UNIVERSIDADE DE SÃO PAULO

INSTITUTO DE FÍSICA DE SÃO CARLOS

LORENZO ANTONIO BUSCAGLIA

Development of a Portable Impedance Spectrometer

São Carlos

2022

LORENZO ANTONIO BUSCAGLIA

Development of a Portable Impedance Spectrometer

Dissertation presented to the Graduate Program in Physics at the Instituto de Física de São Carlos, Universidade de São Paulo to obtain the degree of Master of Science.

Concentration area: Applied Physics
Option: Computational Physics
Advisor:
Prof. Dr. Osvaldo Novais De Oliveira Junior

Corrected Version
(original version available on the Program Unit)

São Carlos

2022

Buscaglia, Lorenzo Antonio
Development of a portable impedance spectrometer / Lorenzo Antonio Buscaglia; advisor Osvaldo N. de Oliveira Junior - corrected version -- São Carlos 2022.
90 p.

Dissertation (Master's degree - Graduate Program in Computational Physics) -- Instituto de Física de São Carlos, Universidade de São Paulo - Brasil , 2022.

1. Impedance Spectroscopy. 2. Signal Processing. 3. Biosensing. 4. SARS-CoV-2. 5. Simple-Z. I. Oliveira Junior, Osvaldo N. de, advisor. II. Title.

Para mi Abuelo Daniel,

que siempre me acompañó

y siempre me va a acompañar.

ACKNOWLEDGEMENTS

Nothing will be alone. There will always be a team.

Here I would like to thank the team that accompanied me during my Masters.

Thank you,

- Professor Osvaldo, for accepting being my supervisor in this project, for your dedication on teaching me and facilitating my academic paths, and especially for the support and affection that I will always remember.
- Papá, for being in this adventure with me, for being my mentor, my friend and my father always.
- Mamá, for being unconditionally present, for helping me with the software development for so many days, and most important, for being my mother.
- Sisters, grandparents (Sílvia and Vivaldo, you too!), uncles and aunts, cousins, Mariana and Marcelo, for accompanying me during these years.
- Friends from São Carlos, Bariloche and abroad, all essential for me to work every day.
- Bianca, for the deep friendship, for the teachings, and especially for the months of quarantine together, which were so important for this project to succeed.
- Larissa, for being my partner and having participated with much love in my daily life during this adventure.
- Professor João P. Carmo, for your guidance with the electronics and for your collaboration during the writing of the review article and patent application.
- Tía Mariana, for your thoughtful collaboration on designing the logo and the casing of Simple-Z.
- Gounella, Poste, Tiago and Melk, for all your time helping me in the fabrication of Simple-Z.
- Paulo, for your time and dedication on helping me with the sodium sulfate, among others, experiments.
- Tío Car, for your very careful mentoring during the experiments with cyanobacteria.
- Fellipe, for the many hours spent in the laboratory helping me on the experiments with cyanobacteria and for helping me write the correspondent part in this dissertation.
- Andrey and Juliana, for working with me over this years and especially on the article on SARS-CoV-2.

- Professor Margaret, even though the pandemic brought down our plans, for your willingness and efforts on receiving me in Ireland for working together.
- Willyan, Priscila and all Biosens, for supporting my personal development.
- All the co-authors of the works published throughout my Masters, it was a pleasure working with you.
- Employees of the Bernhard Gross Polymers Group, of the Department of Physics and Materials Science (FCM), of the Institute of Physics of São Carlos (IFSC), and of the University of São Paulo (USP), who contributed directly or indirectly to this project.
- University of São Paulo (USP) and Institute of Physics of São Carlos (IFSC), for considering me worthy of building this title of Master in Science.
- The São Paulo Research Foundation (FAPESP), for granting this project's scholarship, and I extend my acknowledgements to all research and development funding agencies, for giving the opportunity for carrying out high quality research and the consequent formation of excellent professionals for our society.

This study was financed in part by the Fundação de Amparo à Pesquisa do Estado de São Paulo - Brasil (FAPESP) - Process Number 2019/00101-8.

ABSTRACT

BUSCAGLIA, L. A. **Development of a portable impedance spectrometer**. 2022. 90 p. Dissertation (Master in Science) - Instituto de Física de São Carlos (IFSC), Universidade de São Paulo (USP), São Carlos - SP - Brazil, 2022.

Electrical impedance spectroscopy has been used extensively for sensing and biosensing due to the multiple electrical properties that can be interrogated through varying the frequency of the electrical excitation. An impedance spectroscopy system comprises three main units: signal processing, sensing and data analysis. This Masters Dissertation starts with a detailed revision of these units. We elaborate upon the methods to fabricate sensing units, including the choice of nanomaterials and biomolecules in controlled molecular architectures. Using arrays of sensing units, as electronic tongues, generates large amounts of data that require the use of data analysis methods, which we also revise and include examples of information visualization and machine learning techniques. The main focus of the revision, however, is on the signal processing unit, responsible for generating the excitation signal and performing the impedance readout. This focus is due to the high cost of the impedance spectrometers available in the market, which hampers integration of biosensing systems to be used in the field. A detailed description is given of the methods to develop a portable, fully integrated low-cost impedance analyzer that offers wide impedance magnitude, signal amplitude and frequency ranges. The device referred to as Simple-Z includes the integrated circuit AD5933 and peripheral circuits that allow for fine output amplitude regulation, flexible response amplification, sampling rate control, automatic calibration and external communication. We were able to fabricate a few units of Simple-Z with reproducible results, develop a graphical user interface and apply it successfully in sensing and biosensing, including for SARS-CoV-2 detection. The validity of Simple-Z was confirmed by comparing its results in some of the applications with those obtained with benchtop commercial impedance analyzers. Simple-Z can now be deployed in point-of-care diagnosis systems. Furthermore, owing to its low cost it can be fabricated with mass production to also be used in teaching labs for training students in electrical impedance spectroscopy.

Keywords: Impedance spectroscopy. Signal processing. Biosensing. SARS-CoV-2. Simple-Z.

RESUMO

BUSCAGLIA, L. A. **Desenvolvimento de um espectrômetro de impedância portátil**. 2022. 90 p. Dissertação (Mestrado em Ciências) - Instituto de Física de São Carlos, Universidade de São Paulo, São Carlos, 2022.

A espectroscopia de impedância elétrica tem sido usada extensivamente para (bio) sensoriamento graças às múltiplas propriedades elétricas que podem ser interrogadas por meio da variação da frequência da excitação. Um sistema de espectroscopia de impedância compreende três unidades principais: processador de sinais, sensor e analisador de dados. Esta Dissertação de Mestrado começa com uma revisão detalhada dessas unidades. Revisamos os métodos para fabricar sensores, incluindo a escolha de nanomateriais e biomoléculas em arquiteturas moleculares controladas. O uso de matrizes de sensores, como línguas eletrônicas, gera grandes quantidades de dados que exigem o uso de métodos de análise de dados que também revisamos e incluímos exemplos de visualização de informações e técnicas de aprendizado de máquina. O foco principal da revisão, entretanto, está no processador de sinais, responsável por gerar o sinal de excitação e realizar a leitura de impedância. Esse foco se deve ao alto custo dos espectrômetros de impedância disponíveis no mercado, o que dificulta a integração de sistemas de biossensoriamento para serem utilizados em campo. É fornecida uma descrição detalhada dos métodos para desenvolver um analisador de impedância portátil, totalmente integrado e de baixo custo que oferece amplas faixas de magnitude de impedância, de amplitude de sinal e de frequência. O dispositivo, nomeado Simple-Z, inclui o circuito integrado AD5933 e circuitos periféricos para regulagem fina de amplitude de saída, amplificação flexível de resposta, controle da frequência de amostragem, calibração automática e comunicação externa. Fabricamos algumas unidades de Simple-Z com resultados reprodutíveis com uma interface gráfica e aplicamos com sucesso em (bio)sensoriamento, incluindo a detecção de SARS-CoV-2. A validade do Simple-Z foi confirmada comparando seus resultados em algumas das aplicações com aqueles obtidos com analisadores de impedância comerciais de bancada. O Simple-Z agora pode ser implantado em sistemas de diagnóstico para uso em campo. Além disso, graças ao seu baixo custo, pode ser fabricado com produção em massa para ser utilizado também em laboratórios de ensino para treinamento de alunos em espectroscopia de impedância elétrica.

Palavras-chave: Espectroscopia de impedância. Proessamento de sinais. Biossensoriamento. SARS-CoV-2. Simple-Z.

LIST OF FIGURES

LIST OF ABREVIATIONS AND ACRONYMS

11-MUA	11-MercaptoUndecanoic Acid
3D	3-Dimensional
ABB	Auto-Balanced Bridge
AC	Alternated Current
ADC	Analog-to-Digital Converter
ASM-1	Artificial Sputum Medium 1
B	Susceptance
BIA	BioImpedance Analysis
BioTACE	laboratory of BioToxicology of Continental Waters and Effluents
CLK	CLocK
CMOS	Complementary Metal-Oxide-Semiconductor
CNPEM	Brazilian National Center for Research in Energy and Materials
CoNaMA	Brazilian National Council of Environment
CoViD-19	CoronaVirus Disease 2019
CP	Charge-Pump
cpDNA	ChloroPlast DNA
CRISPR	Clustered Regularly Interspaced Short Palindromic Repeats
DAC	Digital-to-Analog Converter
DC	Direct Current
DDS	Direct Digital Synthesizer
Δ	Sensitivity
DFT	Discrete Fourier Transform
DNA	DeoxyriboNucleic Acid
EDC	N-(3-Dimethylaminopropyl)-N’-ethylcarbodiimide hydrochloride
EESC	School of Engineering of São Carlos
ELISA	Enzyme-Linked ImmunoSorbent Assay
e_{TR}	Truncation Error

FAPESP	Fundação de Amparo à Pesquisa do Estado de São Paulo
FCR	Frequency Control Register
FCW	Frequency Control Word
FET	Field-Effect Transistor
f_{OSC}	Oscillator Frequency
f_{OUT}	Output Frequency
f_{SMP}	Sampling Rate
G	Conductance
GUI	Graphical User Interface
HMDSO	HexaMethylDiSilOxane
HPV16	Human PapillomaVirus 16
I-to-V	current-to-Voltage
I2C	Inter-Integrated Circuit
IC	Integrated Circuit
ICG	Impedance CardioGraphy
IDE	Integrated Development Environment
IDMAP	Interactive Document MAPping
InfoViz	Information Visualization
IUPAC	International Union of Pure and Applied Chemistry
KPGA	Programmable Gain Amplification
LAMP	Loop-mediated isothermal AMPlification
LB	Langmuir-Blodgett
LbL	Layer-by-Layer
LC	inductor-Capacitor
LCR	inductor-Capacitor-Resistor
LF	Loop-Filter
LMF	MicroFabrication Laboratory
LNA	Locked Nucleic Acid
LNN	Brazilian National Nanotechnology Laboratory

LoD	Limit of Detection
LPF	Low-Pass Filter
LSPR	Localized Surface Plasmon Resonance
LUT	Look-Up Table
Mac	Multiply-Accumulate
ML	Machine Learning
NCO	Numerically-Controlled Oscillator
NHS	N-HydroxySuccinimide
OP-AMP	Operational Amplifier
OSC	Reference Oscillator
PA	Phase Accumulator
PAC	Phase-to-Amplitude Converter
PAR	Phase-Accumulation Register
PBS	Phosphate Buffered Saline
PCA	Principal Component Analysis
PCB	Printed Circuit Board
PCR	Polymerase Chain Reaction
PDMS	PolyDiMethylSiloxane
PFD	Phase-Frequency Detector
PLA	PolyLactic Acid
PLL	Phase-Locked Loop
ppm	parts-per-million
Q	Quality Factor
R	Resistance
R_{CAL}	Calibration Resistance
R_{FB}	Feedback Resistance
RNA	RiboNucleic Acid
R_{NEG}	Negative Resistance
RT-PCR	Real-Time PCR

S	Silhouette coefficient
SAM	Self-Assembled Monolayer
SARS-CoV-2	Severe Acute Respiratory Syndrome CoronaVirus 2
SD	Standard Deviation
SPR	Surface Plasmon Resonance
ssDNA	single-strand DNA
θ	Phase
USB	Universal Serial Bus
USD	United States Dollar
USP	University of São Paulo
UV	Ultra-Violet
VCO	Voltage-Controlled Oscillator
X	Reactance
XOR	Exclusive Disjunction
Y	Admittance
Z	Impedance

LIST OF SYMBOLS

%	Percent (10^{-2})
º	Degrees
ºC	Degrees Celsius
a	Ato (10^{-18})
c	Centi (10^{-2})
cal	Calories
d	Deci (10^{-1})
g	Grams
h	Hours
Hz	Hertz
k	Kilo (10^{3})
L	Liters
M	Mega (10^{6}) or Molar (mol/L)
m	Milli (10^{-3}) or Meters
min	Minutes
mol	Moles (6.022×10^{23} elementary entities)
n	Nano (10^{-9})
p	Pico (10^{-12})
ppm	Parts-per-million
rad	Radians
s	Seconds
V	Volts
µ	Micro (10^{-6})
Ω	Ohms

CONTENTS

1 INTRODUCTION

Electrical impedance spectroscopy has been used in the characterization of materials [1] for a variety of reasons, especially because it allows for distinguishing interface from bulk phenomena.[2–5] It is also useful for sensing and biosensing since the electrical properties of materials are highly dependent on their interaction with the environment. Indeed, different effects can be interrogated by varying the frequency of the electrical stimulus, which is exploited in determining the interfacial changes induced in sensing experiments.[6–9] This has made impedance spectroscopy a method of choice for much work on sensors and biosensors,[1,10,19,11–18], particularly with sensing units comprising nanomaterials that possess large surface area-to-volume ratios.[1,20-21] In several cases, sensing with impedance spectroscopy performed better than with traditional techniques, such as polymerase chain reaction (PCR) or enzyme-linked immunosorbent assay (ELISA), in sensitivity, limit of detection, speed and cost.[9,22] Electrical impedance spectroscopy is based on applying an alternated current (AC) voltage and measuring, for a range of frequencies, the amplitude and phase of the current going through the sample, providing a complex impedance spectrum.[16] One option relies on applying a single stimulus formed by multiple frequencies, and performing a simultaneous analysis through a fast Fourier transform algorithm. However, this approach is computationally expensive, highly sensitive to noise and its complicated signal processing hardware implies large costs.[23-24] As a result, the commercial spectrometers deal with one frequency at a time.[25]

In most of the work using spectroscopy, static impedance is used since the response is not expected to vary with time or voltage. However, impedance analyzers can also be used for dynamic analyses, which require consideration of additional factors. Capacitance-voltage measurements, on the other hand, are complementary to impedance spectroscopy, as the electrical properties of the sample interrogated differ. A static impedance-based system can be divided into three main units. The first one is the signal processing unit, responsible for the necessary conversions between the digital and the analog circuits. The second part is the sensing unit, which makes the electrical connection between the circuits and the sample, usually a liquid or gas. Finally, the data analysis unit is responsible for exploiting the digitalized impedance spectra in classification algorithms to identify the sample. In the section “2 LITERATURE REVIEW” of this dissertation we review the main concepts behind these units, with examples from the literature. Special emphasis is given to the electronics involved that allow for portable and low-cost implementations. We also include a brief list of applications and challenges for using impedance spectroscopy in sensing and biosensing.

Traditionally, precise wide-spectrum impedance spectrometers are employed as signal processing units. These have almost no limitations regarding impedance magnitude, signal amplitude or signal frequency ranges, such as Solartron 1260A (National Instruments), E4990A (Keysight) and MFIA (Zurich Instruments), to name a few. The high cost of these devices (>10k USD), and their non-portable size and weight, hamper the development of integrated biosensing systems to be used in the field, as in point-of-care diagnostics.[26] Over the last years, the portability of wide-spectrum spectrometers has evolved considerably, resulting in very small and wireless devices, such as the Sensit Smart (PalmSens). However, their prices (>1k USD) and lack of adaptability still represent a barrier. Researchers have opted to develop low-cost narrow-spectrum spectrometers specifically for their application needs, many of them[27–32] using the integrated circuit (IC) AD5933 (Analog Devices), which integrates basic impedance spectroscopy functions.[33] To our knowledge, the novel "ABE-Stat"[34] was the first approach to fill the gap of a wide-spectrum low-cost impedance spectrometer. However, it does not provide several features available in commercial devices. With the aim of bridging between the increasing diversity in biosensors and the development of custom electrical impedance spectroscopy-based integrated prototypes to be used in the field, in this project we developed Simple-Z: a portable, precise and very-low-cost impedance spectrometer. Our design includes new strategies for output and response amplitude regulation, discrete Fourier transform (DFT) calculation and impedance calibration, among other improvements. The details about the development of Simple-Z are presented in section "3 DESIGN AND FABRICATION OF SIMPLE-Z".

2 LITERATURE REVIEW

Most of the content of this section can be found in reference.[35]

2.1 Signal Processing

The signal processing unit receives a digital value with the frequency to be analyzed and returns the complex impedance result. This process may be split into excitation and reading. The former comprises frequency generation, involving controlled oscillation, digital-to-analog conversion and amplitude regulation. The latter regards impedance readout circuits, which involve response amplification, analog-to-digital conversion and impedance calculation.

2.1.1 Frequency Generation

Impedance spectroscopy requires sinusoidal signals with high harmonic quality, precise frequency, low noise and high stability against changes in the environment, especially temperature.[36-37] Frequencies normally range between 0.1 Hz and 10 MHz and can be generated with a frequency synthesizer. This synthesizer divides the output of a fixed oscillator, or uses a variable oscillator, or even combines both. Oscillators can be classified into resistive and resonant. The former may be referred to as relaxation or non-linear oscillators and are based on switching circuits, usually outputting a square wave, and classified as saturated and non-saturated.[38-39] The resonant type, also known as harmonic, tuned, tank or linear oscillators, output a sinusoidal signal. In this section we discuss their application.

The best option of non-linear oscillators is known as ring oscillators and use digital circuits combined with internal and external resistors and capacitors in their implementation.[38,40] This approach occupies less silicon area than a resonant oscillator, however it has considerably higher phase noise[41] which explains its lack of popularity in impedance spectroscopy. The resonant ones have two main types: inductor-capacitor (LC) and crystal oscillators. **Figure 1** shows an LC oscillator, where the ohmic losses (R_{loss}) in an inductor with some quality factor (Q) are $R_{loss} \sim Q^2 R_s$. The conditions for this circuit to oscillate follow the Barkausen criterion,[42] with a unitary closed-loop gain and a 360^o-multiple phase delay. The operational amplifier (OP-AMP) provides a negative resistance (R_{neg}) allowing the oscillator frequency $f_{OSC} = [(2 \pi L C)^{1/2}]^{-1}$ when $R_{loss} > |R_{neg}|$. An LC oscillator generates sinusoidal waves with good degree of purity, achieving easily a Q of 60. However, it is extremely difficult to match a targeted frequency due to the L and C components industrial tolerances, which in the best case are 0.1%.

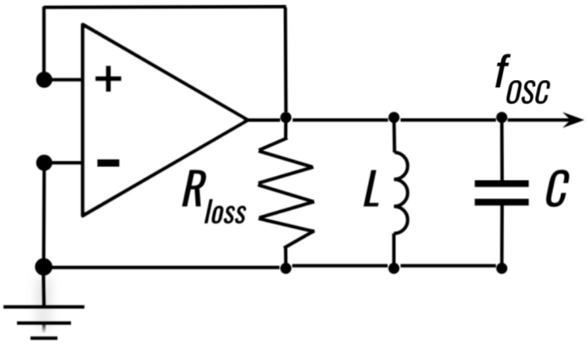

Figure 1: Circuit diagram for an LC oscillator.
Source: Adapted from BUSCAGLIA *et al.*[35]

A more precise way of implementing a resonant oscillator is using a crystal. This mechanical resonator transmits the signal through the piezoelectric effect. **Figure 2** shows the symbol and equivalent circuit of a piezoelectric crystal.[43] The electrical components in the equivalent circuit define the crystal serial resonance frequency $f_{OSC} = [(2 \pi L_s C_s)^{1/2}]^{-1}$, known as Pierce oscillator. This signal frequency depends on various tunable properties of the crystal, such as shape, size and elasticity. This type of fabrication allows matching frequencies with tolerances measured in parts-per-million (ppm) and with the addition of a minimum Q of 10000,[43] resulting in an excellent option as reference oscillation frequency.

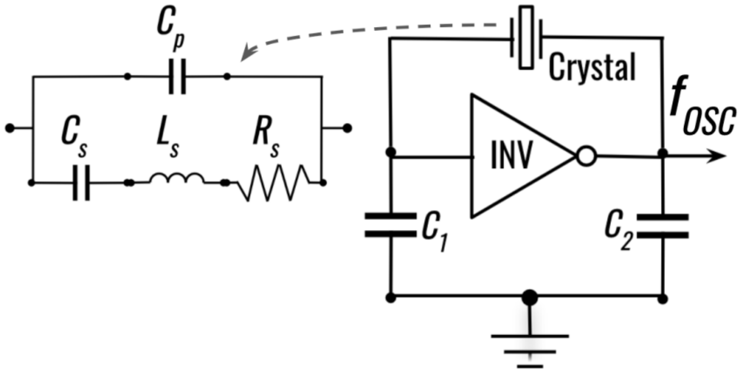

Figure 2: Circuit diagram for a crystal oscillator with the crystal’s equivalent circuit.
Source: Adapted from BUSCAGLIA *et al.*[35]

Any of the above fixed frequency approaches can be adapted to a voltage controlled oscillator (VCO), such as the resonant LC ones that use variable capacitors (varactors).[44] VCOs are used mostly in phase-locked loop (PLL) circuits with a reference frequency f_{OSC}. **Figure 3** shows a block diagram of a PLL, comprising a phase-frequency detector (PFD), a charge-pump (CP), a loop-filter (LF), a VCO and a frequency multiplier N, with output frequency $f_{OUT} = N f_{OSC}$. LF can be freely changed by the designer to avoid the PLL’s prone closed-loop instability.[38,40,44-45] The LF design details, in terms of PFD and CP gain K_ϕ [2π/rad], VCO gain K_{VCO} [Hz/V] and N, can be found in the literature.[46] This flexibility makes PLLs based on resonant VCOs useful for impedance spectroscopy systems, which require sine waves with high harmonic purity.[47]

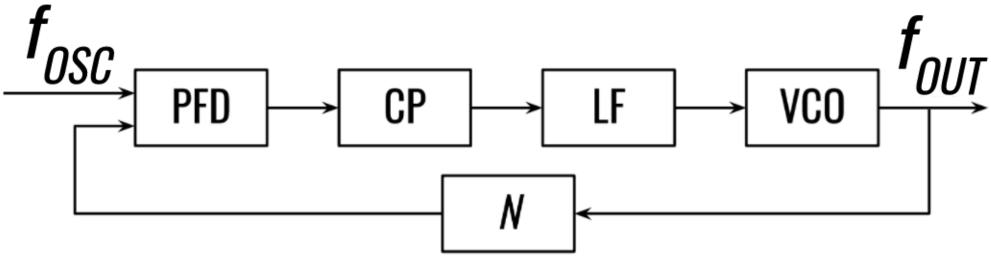

Figure 3: Block diagram of a PLL.
Source: Adapted from BUSCAGLIA *et al.*[35]

An alternative to generate variable signal is a system known as direct digital synthesizer (DDS), also widely employed on instruments for impedance spectroscopy.[16,32,48–50] **Figure 4** shows a block diagram of a DDS comprising a reference oscillator (OSC), a frequency control register (FCR), a numerically-controlled oscillator (NCO), a digital-to-analog converter (DAC) and a low-pass filter (LPF). OSC establishes a maximum output frequency $\max(f_{OUT}) = f_{OSC}$. FCR is an ordinary register based on flip-flops, and DAC is a straightforward implementation either based on R-2R resistive ladders or on current source-sinks. The tricky component of DDS is the NCO, which consists of a phase accumulator (PA) and a sine (and/or cosine) phase-to-amplitude converter (PAC). PAC has an internal N-bit phase-accumulation register (PAR) which periodically accumulates the frequency control word (FCW) stored at FCR. It also contains look-up tables (LUTs) with 2^K equally-spaced values of a single oscillation cycle. Due to their symmetry, a quarter-cycle of sinusoidal waves is sufficient. Usually $2^N >> 2^K$, generating a maximum truncation phase error $e_{TR} \sim 360^o / 2^K$. The DDS procedure starts with loading FCW into FCR to define f_{OUT}. In each new OSC cycle, PAR accumulates FCW, resulting in $PAR_{n+1} = PAR_n + FCW$ (considering $PAR_0 = 0$), which gets instantly converted by DAC. Limited by the register size, when $PAR_{n+1} \geq 2^N$ it truncates, discarding the first bit and allowing the oscillation cycle to restart. The DAC output is a flat-top signal, which gets smoothed by the reconstruction LPF. The output frequency is given by $f_{OUT} = f_{OSC} (FCW / 2^N)$. Most ICs used in impedance spectroscopy use DDSs rather than PLLs, which require complex and numerous circuits for frequency sweeping. Furthermore, DDSs employ simpler circuits that allow for a flexible sweep with a single f_{OSC} and provide additional advantages as low-power, low-price and small size.[51]

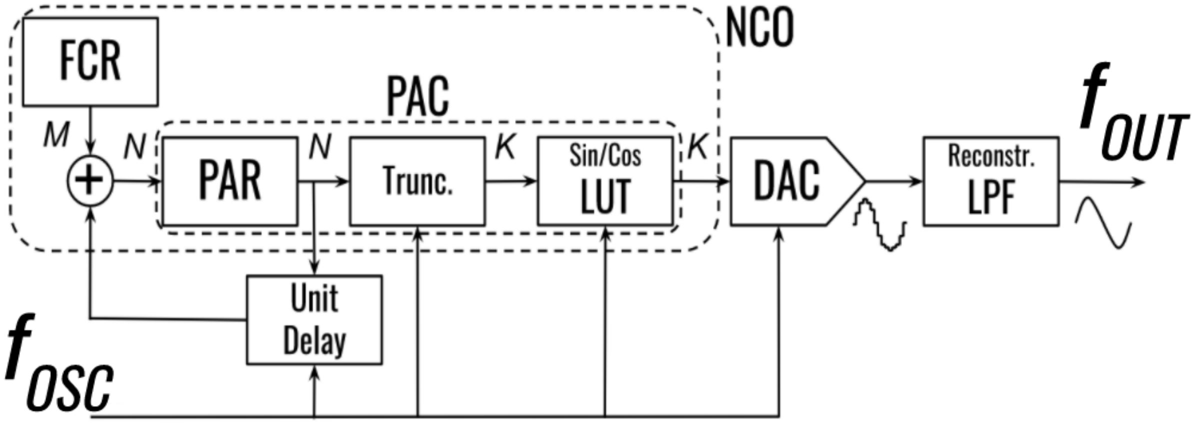

Figure 4: Block diagram of a DDS.
Source: Adapted from BUSCAGLIA *et al.*[35]

The DDS operation can be simulated with a microcontroller, using its memory to store the LUTs.[52] As illustrated in **Figure 5**, the algorithm is built with a simple structure with two adders, one multiplier block and two unit delay cells.[52] The frequency is defined by the parameter F, between -0.2 and 0, and is given by $f_{OUT} = |F|^{1/2} (2 \pi T)$, where T is the time for obtaining a single output data.[52] This approach uses sum, multiplication, analog conversion and memory access, and requires the knowledge of the exact speed of each operation, which is usually complicated to implement.

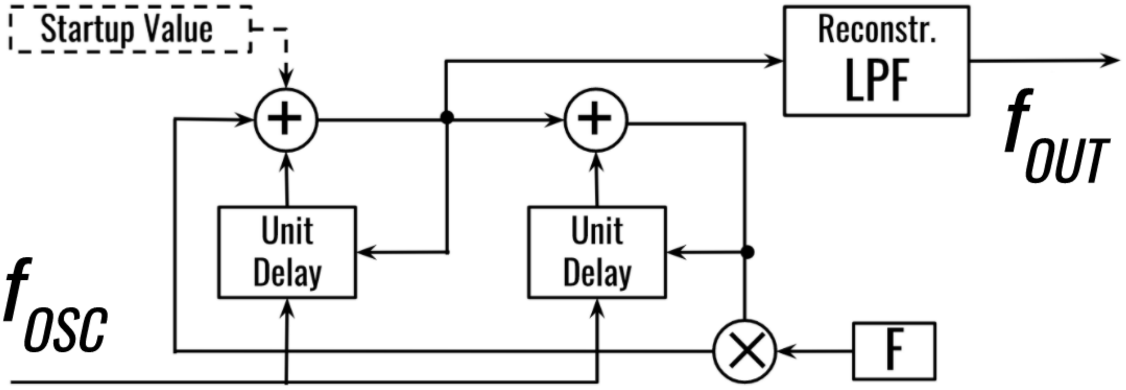

Figure 5: Block diagram of an algorithm to simulate a DDS with a microcontroller.
Source: Adapted from BUSCAGLIA *et al.*[35]

2.1.2 Impedance Readout

The second part of the signal processing unit, namely the impedance readout circuit, compares the excitation and response signals and calculates the impedance. It usually includes an analog-to-digital converter (ADC) and a calculation core. ADCs have a limited voltage amplitude range, a limited number of bits (resolution) and a maximum sampling rate. Usual impedance spectroscopy applications employ excitation amplitudes between 10 mV and 1 V (2 decades) and measure impedances between 10 Ω and 10 MΩ (6 decades).[16] This requires a highly flexible amplification strategy to fit the signal within the ADC conversion limits without creating flattening (small amplitude) problems. Regarding the sampling rate, the frequency range usually stays within 0.1 Hz and 10 MHz (8 decades),[16] requiring hardware/software approaches capable of sweeping the full range without exceeding a reasonable measurement duration. The recommended impedance measuring technique for frequencies up to 100 kHz is the auto-balanced bridge (ABB)[25] shown in **Figure 6**, based on a known feedback resistance in a current-to-voltage (I-to-V) conversion. Due to the OP-AMP limitations, a modified ABB is suggested for frequencies from 100 kHz to 110 MHz, including null and phase detectors and a vector modulator.[25] Both settings allow calculation through comparing amplitude and phase shift before and after the I-to-V conversion. This is the main approach implemented by commercial impedance analyzers.[25] However, it has a major requirement: the sampling rate must be considerably faster than the signal frequency to avoid sub-sampling issues, such as aliasing and precision losses.[16] To fulfil this requirement for the highest frequencies one usually has to employ high-cost acquisition hardware, which hampers customized biosensing developments.[34,53]

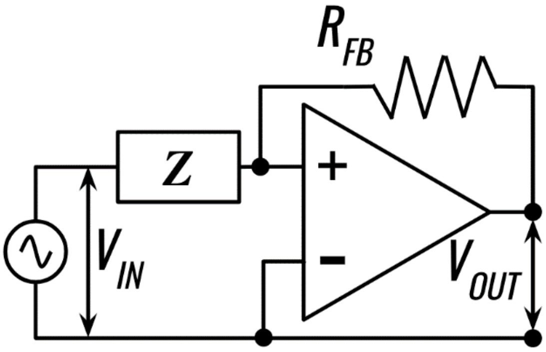

Figure 6: Circuit/Block diagram of an ABB.
Source: Adapted from BUSCAGLIA *et al.*[35]

Most applications of electrical impedance spectroscopy in sensors and biosensors are made with frequencies below 100 kHz. This range is compatible with usual OP-AMPs, allowing for low-cost spectrometers. Indeed, the low-cost (~ 20 USD) impedance analyzer AD5933 was made available by Analog Devices, containing a DDS synchronized with an ADC and a DFT multiply-accumulate (MAc) core, and also contains an inter-integrated circuit (I^2C) communication interface.[33] This piece of hardware depicted in **Figure 7** has several limitations: only four options for AC amplitude, highly restricted impedance magnitude (>1 kΩ) and signal frequency (1 kHz to 100 kHz) ranges, and requires a manual choice of amplification and calibration resistances. Despite this, AD5933 in its minimal configuration represented a breakthrough for low-cost impedance systems, appearing in several publications.[54–57] Some of the limitations were surpassed with peripheral circuits,[30,58–60] as in the ABE-Stat.[34]

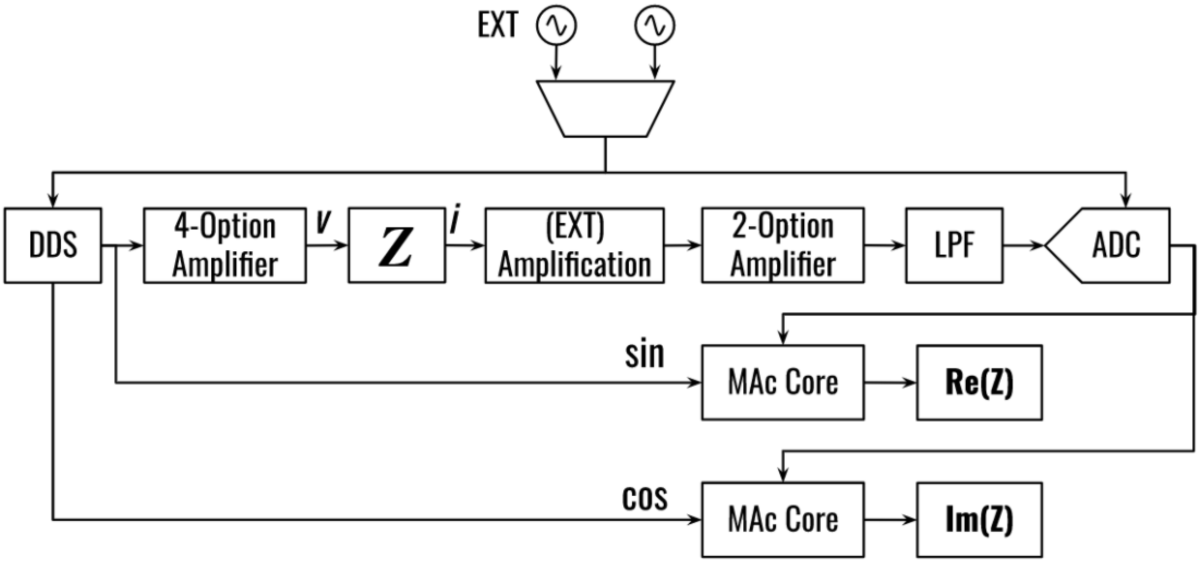

Figure 7: Circuit/Block diagram of AD5933.
Source: Adapted from BUSCAGLIA *et al.*[35]

The “lock-in approach” shown in **Figure 8** is an alternative for measuring impedance within the same ranges and avoiding fast sampling.[61–65] The response signal is analogically multiplied with sine and cosine references and passed through LPFs, outputting two direct current (DC) signals representing the real (resistance) and imaginary (reactance) impedances.[61–64] However, the current commercial alternatives for low-noise and precise analog multiplications are of higher cost than AD5933.

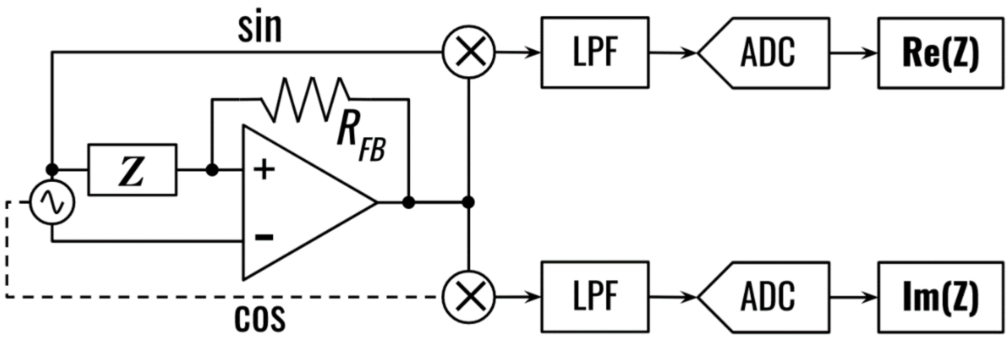

Figure 8: Circuit/Block diagram of the lock-in approach.
Source: Adapted from BUSCAGLIA *et al.*[35]

The concept behind the lock-in approach has also been developed to return signals representing impedance magnitude and phase. This was achieved through replacing the multipliers with modulation, comparison, exclusive disjunction (XOR) and integration circuits.[66] Its block diagram is represented in **Figure 9** as the “phase/magnitude approach”.

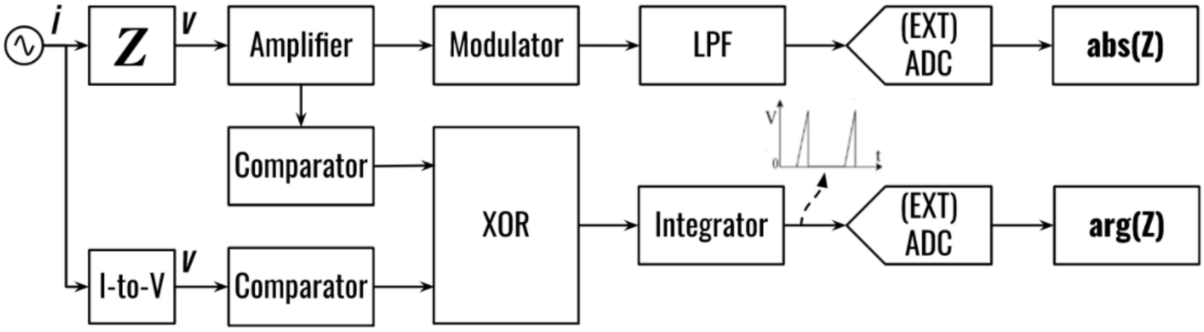

Figure 9: Circuit/Block diagrams of the phase/magnitude approach.
Source: Adapted from BUSCAGLIA *et al.*[35]

2.1.3 Instrumentation Challenges

An important issue related to signal processing is in the limitations of circuit fabrication. Analog signal processing is subjected to parasitic resistances, capacitances and inductances that alter amplitudes and phases in unwanted ways.[67] For example, digital potentiometers such as AD5252 (Analog Devices),[68] which can be implemented as an OP-AMP variable feedback resistance, have significant amplitude and phase deviations for frequencies above 10 kHz.[68] Similarly, low-noise OP-AMPs such as the AD860X (Analog Devices) series have non-ideal capacitances that compromise their performance above 100 kHz.[69] Depending on the degree of impact, these problems may be addressable through software calibration. An additional issue involves the reconstruction LPF, which in some cases needs to be altered during the frequency sweep. For example, when measuring between 1 Hz and 100 kHz (5 decades), the LPF appropriate for the first decade (1 Hz to 10 Hz) might filter the main sinusoidal frequency if used for the last decade (10 kHz to 100 kHz). The most practical solution to this problem is the selective filtering with low-noise analog multiplexing circuits (e.g. ADG7XX [Analog Devices] series).[70] However, their parasitic capacitances also have to be considered for the filtering calculations, and can even constrain the frequency range.

2.2 Sensing Units

Impedance spectroscopy sensors are typically fabricated through depositing electrodes over substrates and coating them with thin films of appropriate materials. These films are usually made of nanostructures, as sensitivity is enhanced when films are ultrathin. If the sensing units are biosensors, the coatings comprise a matrix onto which a bioactive layer is deposited. With molecular-specific interactions, these biosensors may be employed in clinical diagnosis and health monitoring conditions. Another extension in applications is made using an array of sensing units, rather than only a single unit. In this section we shall describe these components, including issues that might affect sensitivity and reproducibility.

2.2.1 Substrates and Electrodes

In sensing with impedance spectroscopy the electrical current goes through multiple materials and interfaces that can be represented by complex impedances.[10,16] On one hand, serial impedances are dominated by the largest magnitudes, motivating electrodes made from materials much more conductive than the sample.[16] Noble metals, e.g. gold,[6,20,71–73] silver[74–76] and platinum,[77-78] or other inert metals, such as stainless steel[79-80] and chromium,[81] are normally used. On the other hand, parallel impedances are dominated by the smallest magnitudes, requiring highly insulating substrates, for example glass,[71-72,82] silicon,[73,83–85], quartz[86] and alumina[82,87]. The recent attempts to reduce costs for disposable sensing units escalated research into flexible materials, including plastics[88] and bio-based materials such as cellulose-related substrates. Two worth highlighting areas are paper-based sensor devices[74,89–92] and wearable[92–96] or implantable devices.[97–99] The latter has very stringent requirements regarding mechanical properties in addition to biocompatibility. Electrodes are fabricated via sputtering, for metal deposition, or with adsorption or printing, for inks and carbon-based materials. Screen printing and three-dimensional (3D) printing, in particular, allow for mass production.[100-101]

The distribution of the electric field affects the detection sensitivity and depends on the electrodes geometry.[19,102-103] Most electrical impedance-based detections use interdigitated electrodes[7,15,18-19] which may be obtained at low cost and provide good distribution within a limited area, increased signal-to-noise ratio, and can be used with small sample volumes.[7,65] The usual design shown in **Figure 10** (a) consists in coplanar microelectrodes with meshed parallel straight fingers forming a rectangular sensing area, fabricated by photolithography.[7] Modifying the interdigits width and interspacing can optimize sensitivity for specific applications.[7,102] Variations of this bi-dimensional design have been explored, including wave,[104] circular[105] and spiral-shaped electrodes,[106] shown in **Figure 10** (b-d), respectively. A few 3D interdigits have also been explored to cover channel walls in microfluidic applications.[107] Besides interdigitated electrodes, simpler designs are used, e.g. parallel,[108-109] cylindrical,[110] round[111-112] and acicular[113] electrodes. Practically any of these shapes can also be adapted and implemented as a multi-polar sensing unit, an approach that also redistributes the current paths.

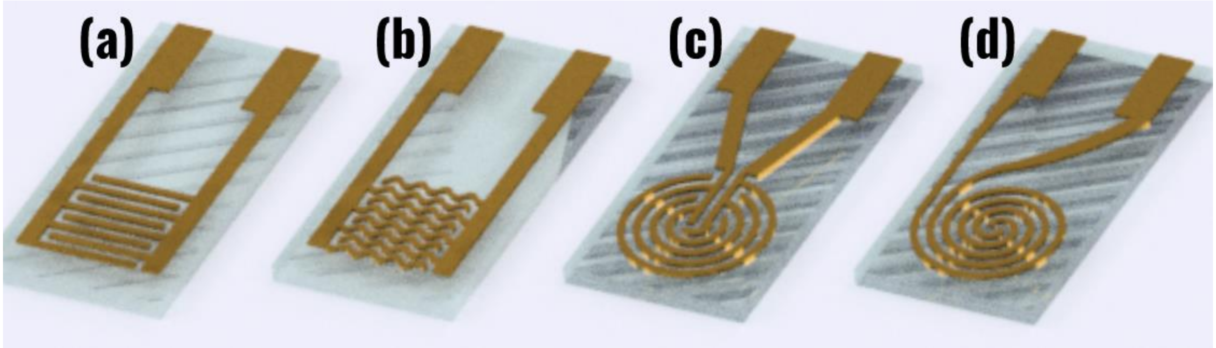

Figure 10: Interdigitated microelectrodes designed with (a) straight, (b) wavy, (c) circular and (d) spiral digits. Source: Adapted from BUSCAGLIA *et al.*[35]

2.2.2 Nanomaterials for Sensors and Biosensors

The main trust in the use of nanomaterials is to increase selectivity (in the case of biosensors) and sensitivity.[22,114] Nanomaterials can be used either in matrices or in active layers, upon exploiting the variety of molecular architectures obtained through methods allowing control in the nanoscale. The most common ones are Langmuir-Blodgett (LB) films, electrostatic layer-by-layer (LbL) films and self-assembled monolayers (SAMs),[21] represented in **Figure 11** (a-c), respectively. The LB technique is based on transferring monolayers from insoluble molecules, organized by Van der Waals interactions at the air-water interface, onto solid supports.[1] Deposition via physical adsorption (physisorption) is possible on hydrophilic or hydrophobic substrates through a slow vertical movement, and multilayer films can be obtained by repetition.[1] One limitation of the LB technique is in the difficulty in depositing water-soluble molecules, which requires special protocols.[1] This limitation was circumvented with LbL films, made from molecules in polyelectrolyte solutions deposited through electrostatic forces.[1] Furthermore, they do not require dedicated equipment, once a few beakers suffice. In contrast to these methods, SAMs are obtained with chemisorption on the substrates.[115] They are restricted to a much smaller number of possible molecules due to the chemical bonding requirement, but are more mechanically stable.[115] The choice of the fabrication method depends on the materials employed and the principles of detection. All three techniques allow for fabrication in a layer-by-layer fashion,[116] being complementary to each other, as explored in reference.[117] They also allow for immobilizing biomolecules, with their bioactivity preserved,[20] and for seeking synergy in the deposition of distinct nanomaterials in the same film. Biosensors are mostly disposable to avoid cross contamination among samples, and their cost vary considerably depending on the biological materials employed.

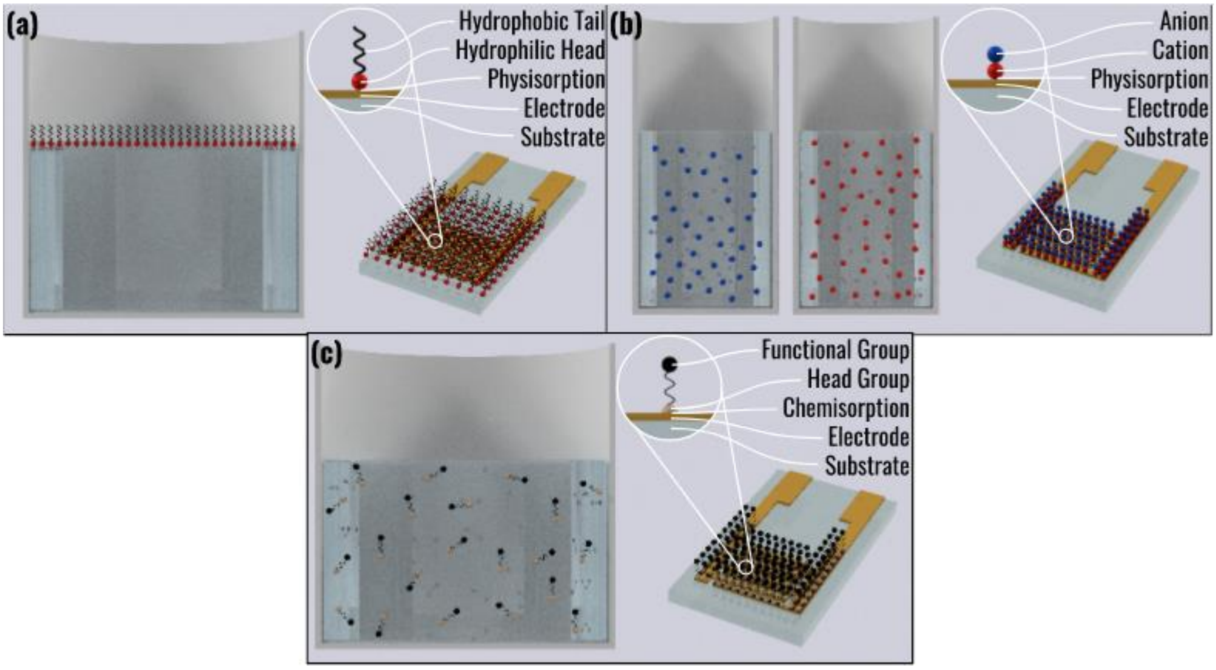

Figure 11: Representations of the medium used and the resultant deposition of films or monolayers through the (a) LB, (b) LbL and (c) SAM techniques.
Source: Adapted from BUSCAGLIA *et al.*[35]

The sensing units almost always contain an ultrathin film coating the electrodes. As already mentioned, most of these coatings involve nanomaterials, as discussed at length in reference.[116] Carbon-based materials such as carbon nanotubes and graphene have been prominent in sensors and biosensors, where in the latter they usually comprise the matrix for the immobilization of biomolecules.[116] Also worth mentioning are the metallic nanoparticles, especially silver and gold, as they affect the electrical properties of the sensing units, which may be exploited in increasing the sensitivity.[116] Similarly to the carbon-based materials, nanoparticles can be incorporated in the matrix of biosensors.[116] The synergy sought in combining nanomaterials and biomolecules is perhaps the most important feature in developing biosensors at present. The extensive use of biosensing has motivated establishing new nomenclatures in the topic. It is often the case that biosensors are referred to by their classes. Then, biosensors can be called enzymatic biosensors, immunosensors when the antigen-antibody interaction is explored, and genosensors for detecting genetic material.[116] Genetic-based sensing is expected to change the landscape of clinical diagnosis, as it can replace expensive procedures such as PCR, which requires sophisticated equipment.[9,118] The most popular biosensors available in commercial products are made with enzymes. The immobilization process of the enzymes is performed with various techniques, for example with LbL films for detecting catechol.[119]

2.2.3 Arrays of Sensing Units

Impedance spectroscopy is also useful in sensing tasks where an array of sensing units is employed, rather than a single unit. Two main cases require such arrays: (i) monitoring/detecting multiple analytes, using distinct sensors/biosensors, and (ii) mapping impedance spatial distribution, using identical units. An example of the former case is an electronic tongue for taste detection in liquid samples, presented in **Figure 12** (a), where multiple sensing units of different materials provide a matrix of information for global selectivity.[79] The latter case is represented by tomographies, as in **Figure 12** (b,c), where the bi or tri-dimensional location of each tissue is sought.[120-121] In these applications identical electrodes are strategically distributed in a spatial matrix. The impedance results through this matrix are combined to produce the desired image.[10,121-122] Similar approaches are used for measuring position, growth and movement.[123–126] In most uses of the mentioned arrays, numerous measurements have to be performed. One option is performing them simultaneously, even with very high-speed sampling circuits that use sample-and-hold techniques,[16,127] or with parallel-acquisition circuits.[128] However, these simultaneous sampling approaches result in expensive systems. Low-cost alternatives reside in sequential measurements, automatically performed with programmable switching circuits. Relays are useful for laboratory settings,[129] but their high dimensions, weight and power consumption hinder portable applications. Smaller complementary metal–oxide–semiconductor (CMOS) analog multiplexers (e.g. the ADG7XX series[70]) are suitable for portable and wearable systems. Indeed, in recent years pixel-like matrices of sensing units were incorporated into the CMOS circuits.[77,124,130-131] This approach allows for a very large number of electrodes, useful for counting cells, as shown in **Figure 12** (d).[130]

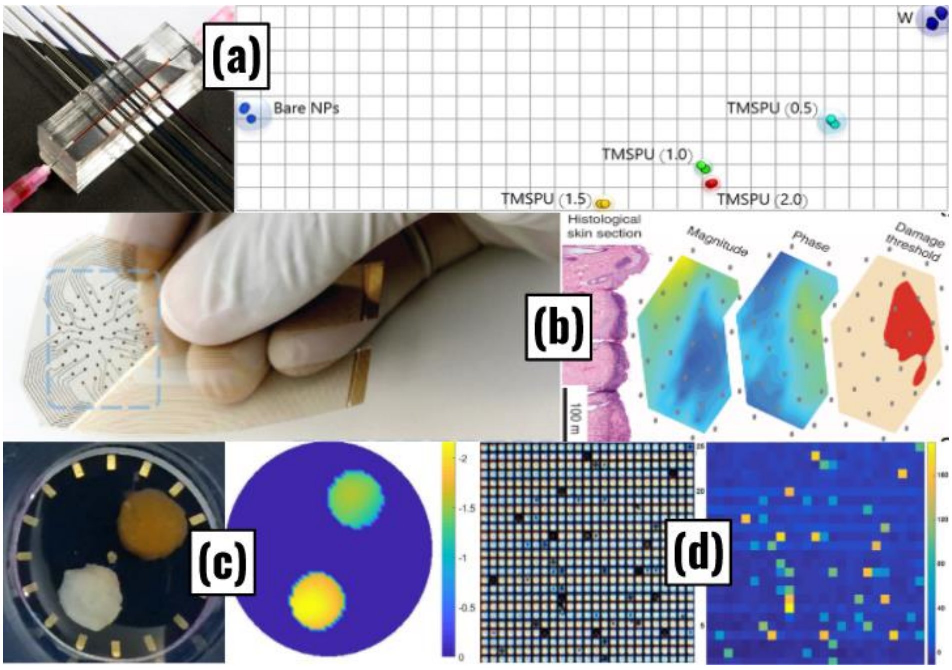

Figure 12: Arrays of sensing units and visualization techniques for (a) an electronic tongue,[79] (b and c) bi-dimensional tomographies[120-121] and (d) pixel-based cell counting.[130]
Source: BUSCAGLIA *et al.*[35]

2.2.4 Common Interferences

In highly-sensitive detection techniques, slight systematic errors can compromise the results. In sensing with electrical impedance spectroscopy there are two main issues to consider: electrode polarization and tracks exposure. Polarization is relevant in electrolytic solutions where the electrodes surface tends to get covered with a layer of ions, of opposite charges, forming an electrical double layer.[16] This phenomenon, represented in **Figure 13**, produces a capacitive electrical barrier, often modelled as a capacitance in series with the sample.[16] The impedance of the double layer is higher at low frequencies and, when it results much higher than the sample impedance, the detection sensitivity gets compromised.[132] The establishment of the double layer may take minutes,[133] and this needs to be considered in measurement protocols. The polarization impedance depends on the electrode material, with platinum being advantageous, especially if platinum black is used, which can reduce polarization impedance by up to four orders of magnitude.[133] Since varying the electrodes geometry can also reduce polarization,[134] interdigitated nanoelectrodes with dimensions near the Debye length (hundreds of nm) have been explored to enhance sensitivity.[135-136]

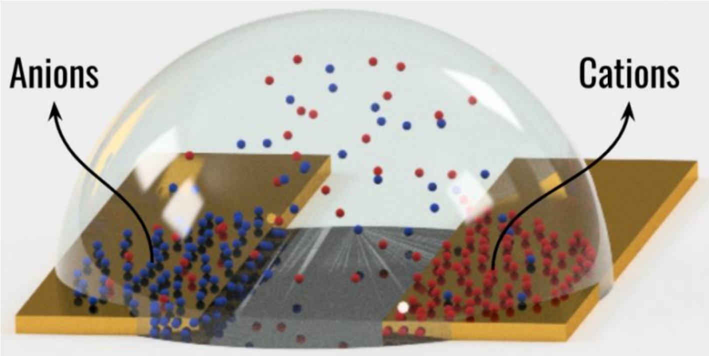

Figure 13: Representation of electrodes polarization.
Source: Adapted from BUSCAGLIA *et al.*[35]

As for the interference regarding the connection tracks in contact with the liquid sample, it results in a parallel capacitance in the impedance model that also affects the detection performance.[137-138] The tracks width has a direct relation to the normalized impedance variation.[138] Aiming for a reproducible measurement, several articles include an insulation layer, usually polydimethylsiloxane (PDMS) that works as a chamber for the liquid sample,[87,139-140] as shown in **Figure 14**. This also avoids variations in the drop interfacial area.[87,140] In addition to these points, the impedance of the materials can be affected by several environmental drifts, especially temperature.[65] Since controlling environmental parameters increases complexity, usually relative variation measurements are a better option.[65]

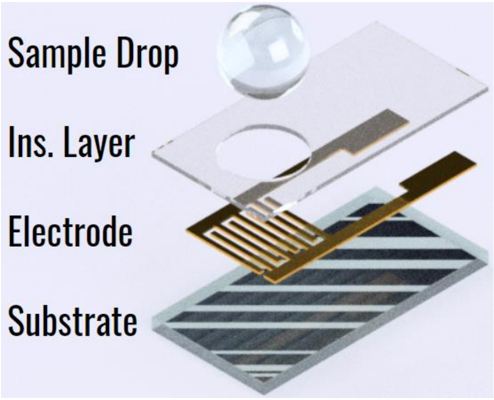

Figure 14: Representation of a sensor with an insulation layer.
Source: Adapted from BUSCAGLIA *et al.*[35]

2.3 Biosensing and Other Applications

The number of papers published involving the use of impedance spectroscopy for sensing and biosensing has increased steadily in the last decade. A brief survey in scientific databases retrieves more than 10k papers, which also include electrochemical impedance spectroscopy – not considered here. Most of this work was produced since the 2000s, as the number of papers per year in the early 1990s was just a few. Review papers have covered considerable parts of this work, normally with focus on applications. For example, impedance-based electronic tongues have been reviewed in the literature.[141] In recent years we note an increasing emphasis in biosensors, especially with low-cost systems that are being developed toward point-of-care diagnosis. Because of this trend we decided to present only a short account of impedance spectroscopy for biosensing.

Nearly all articles in this topic can be classified into three groups: clinical diagnosis, food quality control and cell cultures monitoring. The first group is dominated by the detection of viruses and microorganisms, such as those for Avian Influenza,[142] Hepatitis B,[143] HPV16,[144] CoVid-19,[145] E. Coli,[74,146–148] *S. Aureus*,[22,149-150] S. Epidermidis,[151] M. Tuberculosis,[76] Salmonella Typhi[152] and Brettanomyces.[153] Research into early cancer diagnosis is right behind, including breast,[21,73,108] prostate,[9,154] pancreas,[20,117,155-156] colon[157] and thyroid cancers.[158] Body composition bioimpedance analysis (BIA)[159] and impedance cardiography (ICG)[14] are also noteworthy, since they constitute the most commercially explored applications. Other health-related biomarkers such as cholesterol,[160] cortisol,[109] Ph,[92] glucose and triglycerides[161] have also been detected with impedance spectroscopy. Now regarding the second group, food quality involves the analysis of taste and composition, especially for contamination or adulteration. Electronic tasting has been proven useful for wines,[162] honey,[163] mineral water,[164] ice-cream[80]. and fruits[165]. Contamination can occur with bacteria, detected as for clinical diagnosis, or with toxic pesticides, detectable through electronic tasting.[166] The latter group of articles also involves cell cultures, focusing on low-cost and fast alternatives for monitoring growth and motion, usually with arrays.[125,167–169] Besides these major application areas, impedance spectroscopy is used in characterization of several materials, as in solar cells.[170]

2.4 Data Analysis and Classification

The trend toward ubiquitous sensing and biosensing, in surveillance, monitoring and diagnosis systems, has led to an enormous amount of data, whose processing requires computational and statistical tools. In order to deal with such data, it is useful to recall that from a conceptual - or semantic - perspective, sensing or biosensing corresponds to a classification task. This definition is relevant because of the large body of knowledge accumulated over the years to classify objects or processes, mostly by research communities in statistics and computer science.[13,171-172] Data from sensors and biosensors have long been treated with statistical methods belonging to the realms of chemometrics.[173] There are some applications in which the necessary classification can be done by measuring impedance at a single frequency, chosen from the spectra to optimize the detection sensitivity. In these cases, a calibration curve relating the impedance to the sought property is used.[20,73,174-175] When this is possible, it naturally allows for implementations based on very low-cost single-frequency hardware. However, disregarding the rest of the spectrum means that the potential of classification is diminished, especially as far as selectivity is concerned.

Complex impedance can be represented in polar or Cartesian coordinates and can be transformed into complex capacitance or inductance.[145] Furthermore, by assuming an equivalent circuit suitable for the sample under analysis, as the Cole-Cole models, a spectrum can be summarized into a few inductor-capacitor-resistor (LCR) values using Kramer-Kronigs relations.[10,176] In recent years sensing and biosensing data analysis has been extended with the use of information visualization (InfoViz) methods.[11,177] These encompass linear techniques such as principal component analysis (PCA),[11,166,177-178] and non-linear ones such as Sammon's mapping,[11,150,174,177] interactive document mapping (IDMAP)[11,22,114,150,177] and parallel coordinates.[11,22,116,177] It is noteworthy that the non-linear technique IDMAP, exemplified in **Figure 12** (a), was conceived to classify texts and turned out the most efficient one for biosensing data analysis, enhancing the capability of discriminating complex samples. Perhaps the most relevant advantage of InfoViz is the ability to process a whole dataset rather than portions of it, as normally done in manual analysis. Furthermore, it is possible to perform feature selection by assessing the discrimination ability of the sensing units with metrics such as the silhouette coefficient (S).[9,11,22,154,177]

Data analysis with multidimensional projections is effective for clustering but they require a visual analysis. A practical alternative for automation relies in machine learning (ML),[179] which can be employed with supervised and unsupervised approaches, among others. In spite of its limitations in addressing problems requiring interpretation, ML has been proven effective in classification tasks reaching accuracies over 90%.[180] The trend toward ML to analyze sensing and biosensing data seems irreversible (see some discussion in review papers).[13,171-172,181] The effectiveness of ML methods depends on the amount of data and its coverage of the domain under analysis. In such approaches, different types of data may be integrated to improve classification, especially for clinical diagnostics as the ones cited in section "2.3 Biosensing and Other Applications". In addition to scientific data obtained with impedance spectroscopy, text and images can also be employed.[114] To our knowledge, the first use of ML for impedance spectroscopy data was for correlating electronic tongue results with human taste for Brazilian coffee samples.[182] Since then, several articles explored this approach.[180,183-184] The new concept of multidimensional calibration space based on machine learning is likely to further boost such applications.[185]

3 DESIGN AND FABRICATION OF SIMPLE-Z

Most of the content of this section can be found in reference.[186]

3.1 Circuit Design

The central component of our design is IC AD5933, which can be divided into six parts, as presented in **Figure 15**. These parts are responsible for (a) variable frequency signal generation, (b) output amplification, (c) response amplification, (d) impedance readout, (e) impedance calibration and (f) communication. Each part has a separate function and involves limitations that we needed to overcome in the development of Simple-Z, as described in this section.

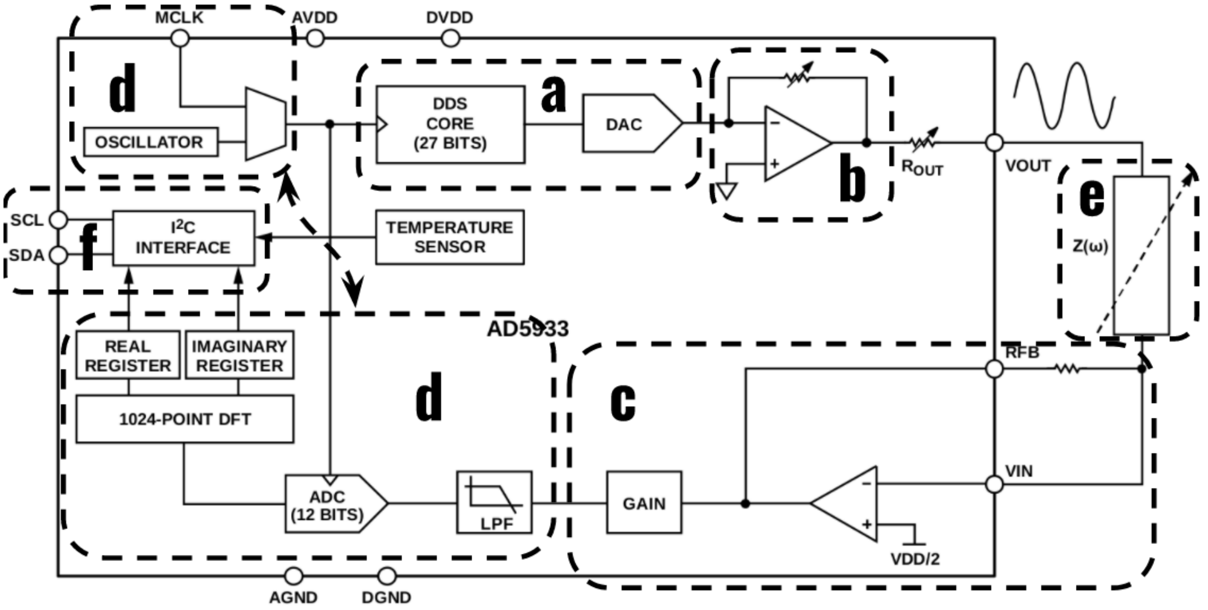

Figure 15: Block diagram of AD5933[33] with (a) variable frequency signal generation, (b) output amplification, (c) response amplification, (d) impedance readout, (e) impedance calibration and (f) communication.

Source: Adapted from ANALOG DEVICES.[33]

3.1.1 Variable Frequency Signal Generation (a)

The AD5933 variable frequency signal generation is performed by a DDS, responsible for generating a sinusoidal signal with a digitally-controlled frequency. It comprises LUTs that contain multiple equally-spaced sinusoidal values which are accessed at a controlled rate and instantly converted into an analog signal. The output frequency is defined by the FCW, stored at a 24-bit FCR, and an internal OSC of 16.776 MHz. The DDS comprises a 27-bit PAR, which allows for dividing f_{OSC} by 2^{27} ~ 134M. The first bits of PA define the address at which the LUTs are accessed by the DAC. The list of frequencies to be analyzed are defined inside AD5933 by three parameters: the first frequency, the step size and the number of steps.[33] This establishes the frequencies in increasing order and linearly separated. However, multiple articles employing electrical impedance spectroscopy use frequencies in decreasing order and with logarithmic separation, since they go through several decades.[9,187] Decreasing frequencies was achieved by forcing the FCW truncation through multiple accumulations, and logarithmic steps were implemented by altering the step size before each frequency change. Both of these solutions were implemented in software.

3.1.2 Output Amplification (b)

The AD5933 output amplification circuit regulates the AC amplitude of the output signal, providing only 4 options (50 mV, 100 mV, 500 mV and 1 V). This represents a problem since some biosensing applications require lower amplitudes (down to 10 mV).[16,85,152,188] Another main limitation is the low maximum current limit, which constrains the impedance range to values over 1 kΩ.[33] We included an external OP-AMP AD8606 in 'follower' mode shown in **Figure 16** which increased the current limit allowing for impedances down to 100 Ω.[189] A further issue is that, for each option of AC amplitude, AD5933 establishes a different DC amplitude.[33] This not only complicates fitting the response signal into the voltage conversion limits, but also impacts the polarization of the electrodes and can even produce unwanted chemical reactions in the sample. We introduced the output amplification circuit presented in **Figure 16**, which comprises a reference resistance, a programmable digital potentiometer AD5252, another OP-AMP AD8606 and a DAC MCP4725 (Microchip). It allows for a fine adjustment of the AC amplitude between 10 mV and 1 V and for adjusting or eliminating the DC component.

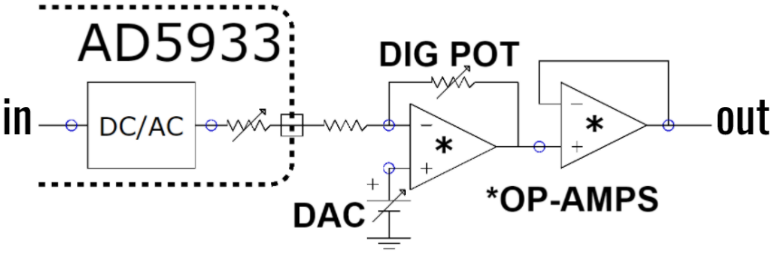

Figure 16: Circuit design of the output amplification of Simple-Z.
Source: Adapted from BUSCAGLIA *et al.*[186]

3.1.3 Response Amplification (c)

The response signal is proportional to the excitation signal, which ranges from 10 mV to 1 V (2 decades). It is inversely proportional to the impedance (Z), which ranges from 100

Ω to 1 MΩ (4 decades). For its acquisition, AD5933 provides a 12-bit (4096 positions) ADC from which at least 100 positions should be used to ensure an acceptable resolution, covering less than 2 decades (100 to 4096). Therefore, amplification is needed to fit the amplitude of the response signal within this ADC range. AD5933 provides a 2-option (1x and 5x) programmable gain amplification (K_{PGA}) and a connection for an external feedback resistance (R_{FB}), both of which need to be chosen depending on Z, characterizing a ‘loop problem’. We introduced the 8-to-1 analog multiplexer ADG728 (Analog Devices) shown in **Figure 17** with 7 options for R_{FB}. Our software combined these options with K_{PGA}, resulting in 13 response amplification options logarithmically distributed along the possible ranges. Furthermore, an iterative software solution was developed to automatically find the appropriate response amplification for an unknown Z.

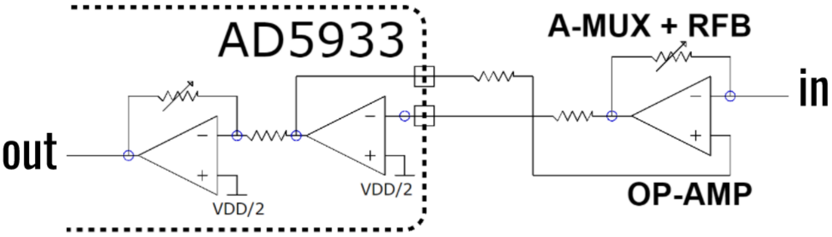

Figure 17: Circuit design of the response amplification of Simple-Z.
Source: Adapted from BUSCAGLIA *et al.*[186]

3.1.4 Impedance Readout (d)

After the amplification, the response signal passes through an embedded reconstruction LPF that smoothes the top-flat shape of the signal produced by DDS. This LPF is designed to eliminate the unwanted frequency components when using the AD5933 internal OSC. In sequence, the signal reaches the AD5933 internal 12-bit ADC which performs 1024 sequential acquisitions at a sampling rate $f_{SMP} = (^{1}/_{16})\ f_{OSC}$. Each acquisition instantly undergoes a MAc operation with a sinusoidal reference from DDS, resulting in a single-frequency DFT. The result is made available through two (real and imaginary) 16-bit registers. This method can lack precision due to three main reasons: spectral leakage, under-sampling and interferences. To avoid spectral leakage, f_{OUT} should be a multiple of f_{OSC}, requiring a very fine control of the latter. An alternative relies on establishing a minimum amount of cycles to be measured and thus reducing the impact of the leakage. In our approach we established that all 1024 points should be distributed along a minimum of 10 signal cycles. To avoid under-sampling issues, a minimum of points per cycle needs to be ensured. We defined this value for our acquisition to have duration between 10 and 102 signal cycles. In

AD5933, the only way of adjusting f_{SMP} is by varying f_{OSC}. AD5933 includes an internal oscillator with a fixed frequency of 16.776 MHz, but also a digitally-selectable connection for an external oscillator allowing for the adjustment of f_{OSC}. As an example for all these numbers, when f_{OUT} is 5 Hz, f_{SMP} should be within 50 Hz and 510 Hz, meaning f_{OSC} should be within 800 Hz and 8.16 kHz. Considering these constraints, we included the programmable variable frequency external oscillator Si5351 (Silicon Labs) shown in **Figure 18**. In our software we implemented a different f_{OSC} for each decade of f_{OUT} (1 Hz to 100 kHz), using the internal oscillator for the last (5th) decade.

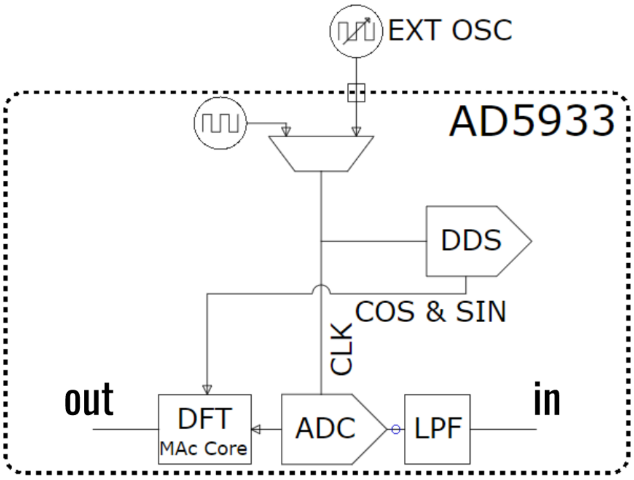

Figure 18: Circuit design of the impedance readout of Simple-Z.
Source: Adapted from BUSCAGLIA *et al.*[186]

The solution above ended up creating a third issue: interference. Since the external f_{OSC} is much lower than the internal one for the first decades of f_{OUT} (1 Hz to 10 kHz), f_{OSC} does not get filtered by the reconstruction LPF embedded in AD5933. This means that the response signal reaches the ADC with top-flat shape, carrying multiple sinusoidal frequencies and so being another source of spectral leakage. We built an external variable reconstruction LPF based on a second ADG728 shown in **Figure 19** that establishes a 5-option capacitance in parallel with an auxiliary resistance. The capacitance and resistance values were chosen in order to filter frequencies above the maximum f_{OUT} of each decade.

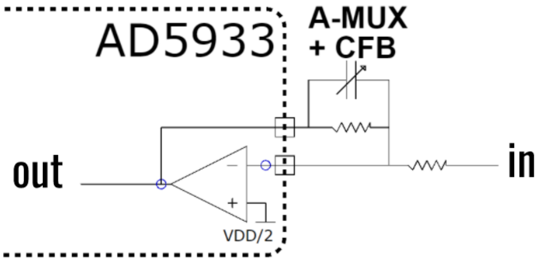

Figure 19: Circuit design of the variable reconstruction LPF of Simple-Z.
Source: Adapted from BUSCAGLIA *et al.*[186]

3.1.5 Impedance Calibration (e)

The acquisition output of AD5933 is a single-frequency DFT result.[33] Its datasheet indicates that after an acquisition is done over the sample, a second acquisition over a calibration resistance (R_{CAL}) is required. The DFT results are combined in a cross-multiplication to obtain Z. The precision of this process depends on the proximity of R_{CAL} to the magnitude of Z, configuring again a loop problem. In our approach, we used the first DFT result for a rough estimation of the magnitude of Z, allowing for the choice of R_{CAL}. A second challenge involves replacing Z with R_{CAL} before the second acquisition. AD5933 does not provide the programmable switching circuit necessary to address this function. For this purpose, we introduced a third ADG728 with 7 R_{CAL}s distributed logarithmically along the impedance magnitude range up to 1 MΩ, as shown in **Figure 20**.

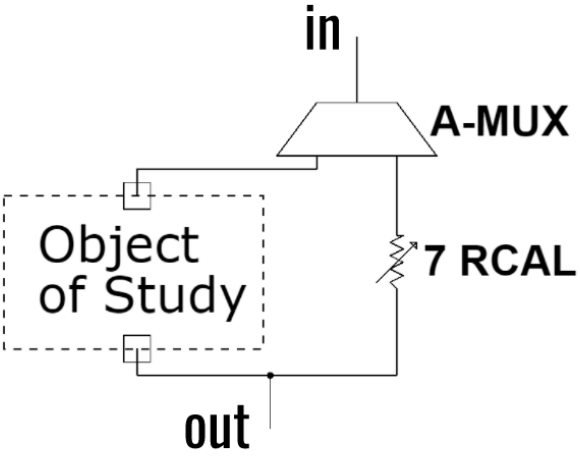

Figure 20: Circuit design of the impedance calibration of Simple-Z.
Source: Adapted from BUSCAGLIA *et al.*[186]

3.1.6 Communication (f)

The hardware of AD5933 does not allow for the storage and execution of a programmable algorithm. Furthermore, the digital output of AD5933 is an array of complex (real and imaginary) 16-bit DFT results, which also needs to be stored in an external memory. The communication of AD5933 consists of an interface for I^2C serial communication, as can be seen in **Figure 15**. I^2C protocol uses two connections: one as timing reference and another for data transfer. These connections can be shared between the devices of the system, once this protocol assigns a unique address to each one. For example, communication between the ICs within Simple-Z (AD5933, AD5252, ADG728, MCP4725 and Si5351) is done through the same couple of I^2C connections. However, devices such as computers and smartphones, required for processing the impedance spectra, plotting and executing sophisticated classification algorithms, usually use Universal Serial Bus (USB) or Bluetooth protocols. We introduced the microcontroller Arduino Mega 2560 shown in **Figure 21**, which comprises I^{2}C and USB interfaces to bridge between these two communication technologies. It also provides a small memory and a microprocessor to store and execute the electrical impedance spectroscopy algorithm.

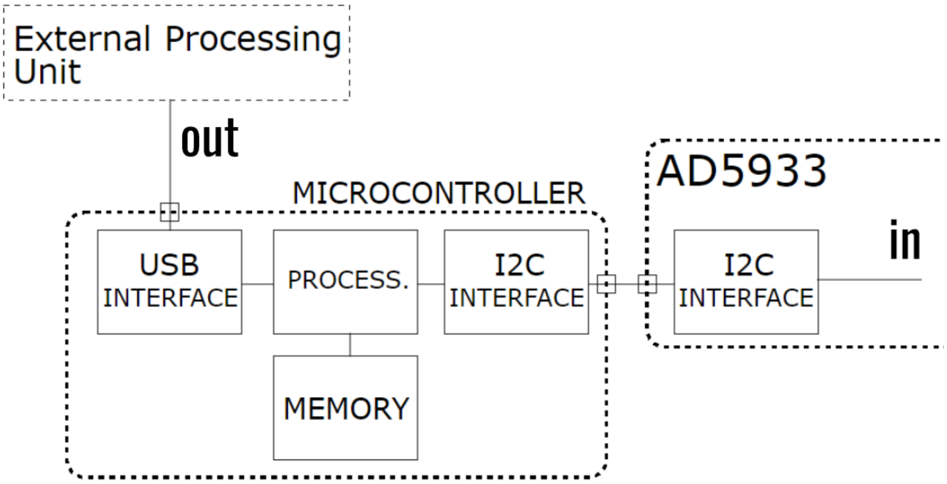

Figure 21: Block diagram of the communication of Simple-Z.
Source: Adapted from BUSCAGLIA *et al.*[186]

3.1.7 Full Circuit

The full design of the circuit of Simple-Z is presented in **Figure 22**, where we discriminated the output frequency generation, the output amplification, the response amplification, the impedance readout, the impedance calibration and the communication circuits.

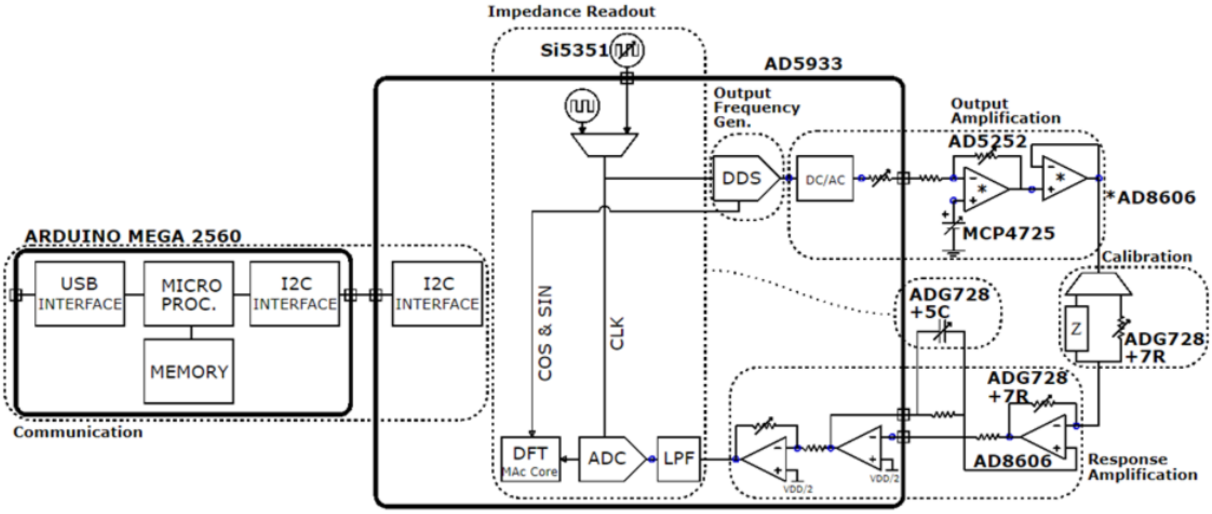

Figure 22: Full circuit design of Simple-Z.
Source: Adapted from BUSCAGLIA *et al.*[186]

3.2 Device Manufacturing

3.2.1 Electronic Circuits

The development of the electronics design involved an iterative process of designing, building and analyzing prototypes until reaching a successful version. In our case the prototyping steps did not require the circuits to be small, allowing us to employ stripboards which speed up and simplify the fabrication process. As presented in **Figure 23**, it starts with the interruption of the copper strips (a), follows the soldering of the jumper wires and the connection sockets (b), and ends with the assembly of the ICs (c).

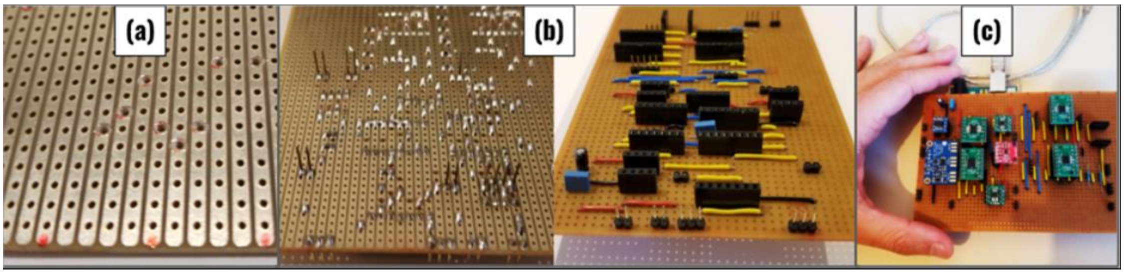

Figure 23: Fabrication steps for electronic circuits using stripboards: (a) interruption of strips, (b) soldering of connections and (c) assembly of components.
Source: By the author.

After the stripboard prototyping process, we designed a printed circuit board (PCB) in the EasyPCB online software. It was based on connecting all the signal processing circuits on the top of the PCB and assembling the Arduino under it to reduce horizontal dimensions. We fabricated this PCB using a traditional method that performs a selective corrosion of a double-sided copper-clad laminate. This method takes several steps based on painting the laminate with photosensitive ink, printing the circuit design over a transparent sheet, ultra-violet (UV)-curing the ink not covered by the printing, removing the un-cured ink and corroding the exposed copper with a ferric chloride solution. **Figure 24** shows the final version of the stripboard-based circuit (a) and its equivalent PCB implementation (b).

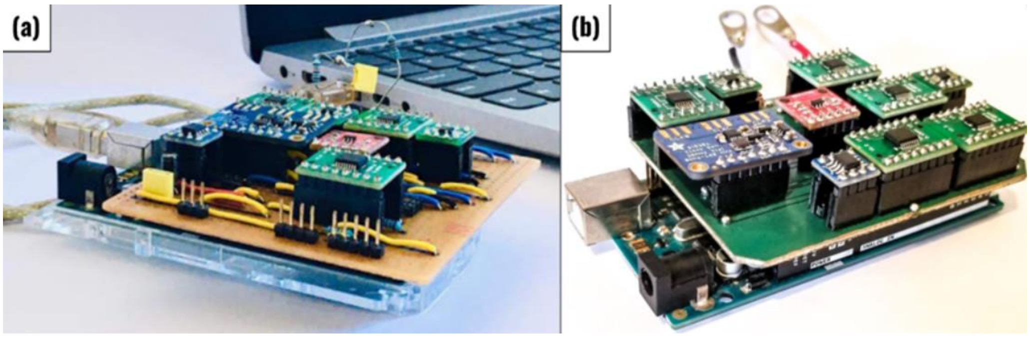

Figure 24: Simple-Z circuit fabricated using (a) stripboard and (b) PCB.
Source: By the author.

3.2.2 Protection Casing

Some basic measurements were first performed to validate the connections inside the PCB, after which we designed the casing to allow its implementation in our laboratories without exposing the circuits to moisture, dust, unwanted electrical contacts and small impacts. We used the 3D design software Autodesk Inventor and fabricated it with a 3D-printer GTMax3D using a 1.75 mm white polylactic acid (PLA) filament. The casing consists of a box with three openings: one for the USB connection and two for the analog connections (red and black) with the sensing unit. At the top of the casing we included the Simple-Z logo, as shown in **Figure 25**. The whole system, including the electronics and the casing has a low production cost of around 100 USD.

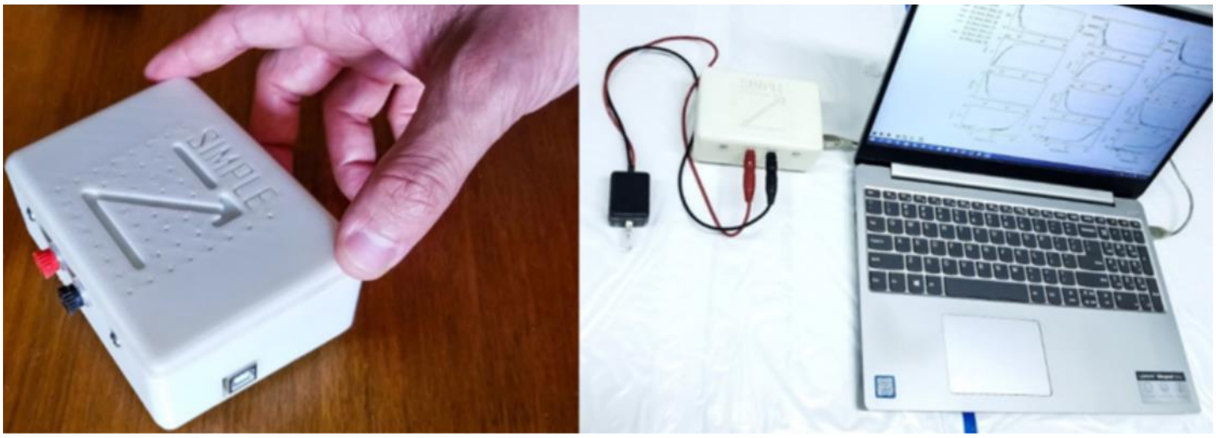

Figure 25: (left) First Simple-Z assembled and (right) Simple-Z connected to computer and sensing unit. Source: By the author.

3.3 Software

An electrical impedance spectroscopy system needs to perform three basic functions: interaction with user for measurement parameters, measurement execution and interaction with user for results output path. The usual approach for these needs is a simultaneous execution of two separate algorithms, one sequential and another event-driven.

3.3.1 Sequential Algorithm

The sequential algorithm is responsible for executing the electrical impedance spectroscopy measurement, without any interaction with the user, and therefore based on a sequential execution of functions. We developed this algorithm in C^{++} language in the Arduino Integrated Development Environment (IDE) and it can be summarized by the flux diagram of **Figure 26**.

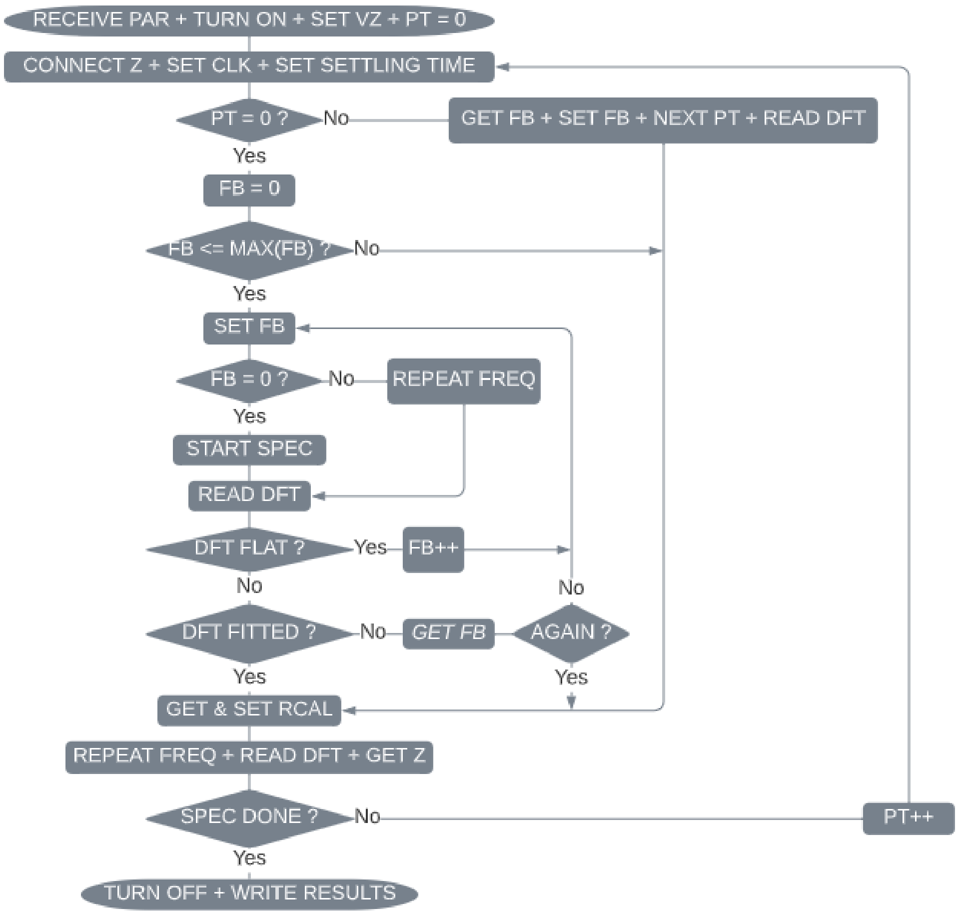

Figure 26: Flux diagram of electrical impedance spectroscopy sequential algorithm executed by the microcontroller.

Source: By the author.

For a better understanding of the algorithm execution, its functionality can be described with the following 4 major groups of steps:

i. Measurement preparation:
   - Receives measurement parameters from computer (user).
   - Commands AD5933, AD5252 and MCP4725 to set the AC amplitude.
   - Commands the calibration ADG728 to connect the sample.
   - Sets Si5351 and oscillator switch to set f_{OSC} corresponding to first frequency.
   - Writes in AD5933 the FCW for first frequency.

ii. Measures first frequency:
   - Commands AD5933 and feedback ADG728 to set minimal response amplification.
   - Commands AD5933 to execute DFT calculation and read DFT result.
   - Compares DFT with reference value: if lower, increases amplification and iterates.
   - Calculates rough estimation of the magnitude of Z.
   - Commands calibration ADG728 to connect corresponding resistance.

  - Commands AD5933 to repeat DFT calculation.
  - Calculates Z for first frequency.
  - Sends to computer an array with circuit parameters and result.

iii. Measures remaining frequencies:

  - Commands calibration ADG728 to connect the sample.
  - Calculates next response amplification based on last point (cross-multiplication).
  - Commands AD5933 and feedback ADG728 to set response amplification.
  - Writes in AD5933 the FCW for next frequency.
  - Commands AD5933 to execute DFT calculation and reads result.
  - Sends to computer an array with circuit parameters and resultant Z.
  - Iterates steps in (iii) until all points are measured.

iv. Ends the measurement:

  - Commands AD5933 to turn off.

3.3.2 Event-Driven Algorithm

The event-driven algorithm is responsible for interacting with the user. Therefore, it comprises a graphical user interface (GUI) with buttons and text entries. We developed this algorithm, presented in **Figure 27**, in Python language, using libraries *tkinter*, *matplotlib*, *numpy*, *cv2*, *time*, *cmath*, *serial*, *winsound* and *os*.

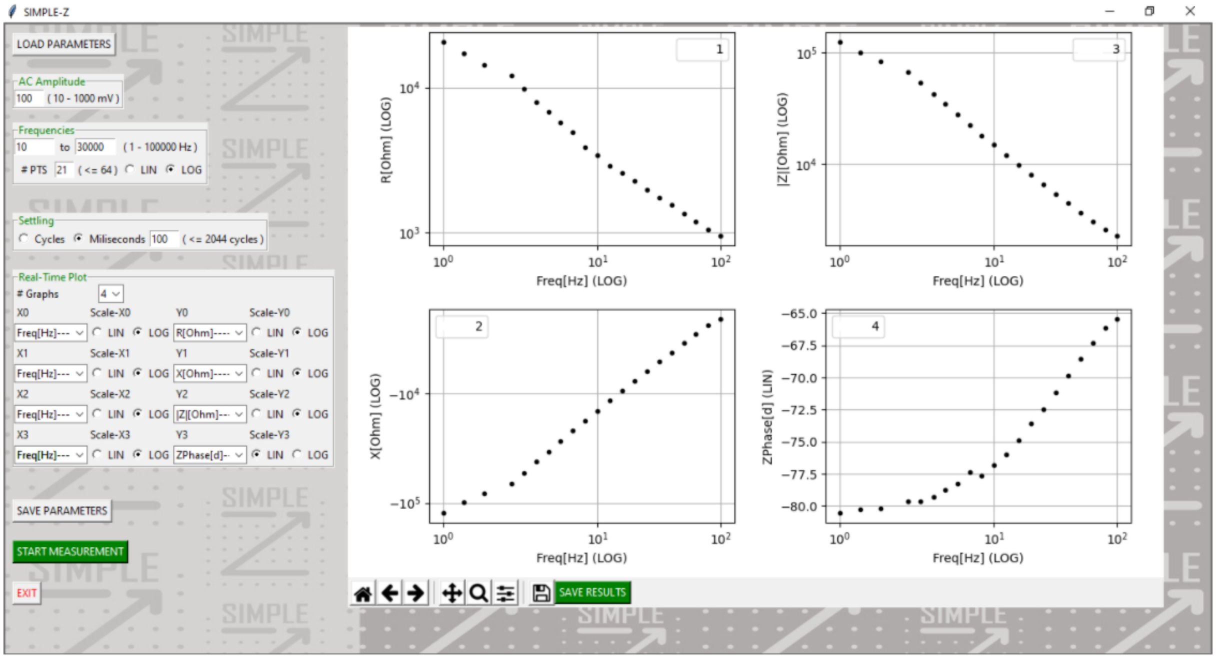

AC Amplitude: 100 (10 - 1000 mV)

Frequencies: 10 to 30000 (1 - 100000 Hz)

PTS 21 (<= 64) ○ LIN ● LOG

Settling: ○ Cycles ● Miliseconds 100 (<= 2044 cycles)

Real-Time Plot: # Graphs 4

X	Scale-X	Y	Scale-Y
X0: Freq[Hz]---	○ LIN ● LOG	Y0: R[Ohm]----	○ LIN ● LOG
X1: Freq[Hz]---	○ LIN ● LOG	Y1: X[Ohm]----	○ LIN ● LOG
X2: Freq[Hz]---	○ LIN ● LOG	Y2: |Z|[Ohm]---	○ LIN ● LOG
X3: Freq[Hz]---	○ LIN ● LOG	Y3: ZPhase[d]--	● LIN ○ LOG

Figure 27: GUI of event-driven algorithm executed in computer which communicates with Simple-Z.
Source: By the author.

For a better understanding of the algorithm execution, the following are steps that the user can follow to execute an electrical impedance spectroscopy:

i. Input the desired measurement parameters using mouse and keyboard (AC amplitude, first frequency, last frequency, number of points, step distribution LIN/LOG, settling mode Cycles/Milliseconds, settling quantity, number of graphs, X axes parameters, X axes distribution LIN/LOG, Y axes parameters, Y axes distribution LIN/LOG) or press ‘LOAD PARAMETERS’ and browse for a previously saved parameters file.
ii. Save parameters by clicking on ‘SAVE PARAMETERS’ and typing the file name, if these parameters might be reused in future measurements.
iii. Start measurement by clicking on ‘START MEASUREMENT’ and wait for the measurement to finish.
iv. Save results by clicking on ‘SAVE RESULTS’ and typing the file name.
v. Exit the program by clicking on ‘EXIT’.

3.4 Reproducibility

In developing industrial products, it is essential to consider fabrication processes that allow for mass production. To validate Simple-Z as a potential industrial product, we sent the design to the company JLCPCB to fabricate the PCBs with which we fabricated 4 additional devices (black, blue, red and green) shown in **Figure 28**. The casing of each device was fabricated using 3D-printing in a 5-hour process and the soldering was done manually in a simultaneous 7-hour process. The casing fabrication can be accelerated (down to seconds) using injection technology for mass production. The soldering process can also be diminished (down to minutes) through using soldering oven technology with a new PCB where all ICs get placed over the same copper layer. The operation of the new Simple-Zs was successfully validated with measurements over simple LCR circuits.

Figure 28: Five copies of Simple-Z fabricated.
Source: By the author.

3.5 Performance Analysis

In the first analysis, we aimed to measure the error and the standard deviation of Simple-Z results through a comparison with the Solartron 1260A. Measurements with sensors and biosensors have a considerable standard deviation, so we opted for using commercial resistors and capacitors. We built four circuits equivalent to human tissues reported in the literature[190–193] and we did three measurements with each circuit using both spectrometers. The electrical impedance spectroscopies ranged between 1 Hz and 100 kHz and used a 500 mV amplitude. On top of **Figure 29** we present the Bode plot of the average of the triplicated results using Solartron 1260A (solid line) and Simple-Z (round markers). On the bottom, we plotted the impedance magnitude relative error and the phase absolute error. Note that the magnitude error reaches a maximum of approximately 8%, staying mostly under 2%. The impedance phase error reaches a maximum of approximately 6°, staying mostly under 2°.

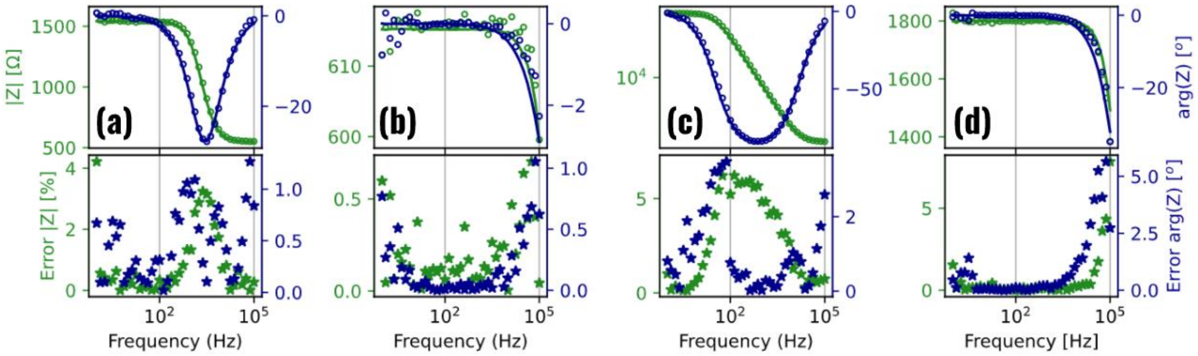

Figure 29: (top) Bode spectra of human-tissue equivalent circuits[190–193] ((a) biceps, (b) breast, (c) blood, (d) arm) measured with Solartron 1260A and Simple-Z and (bottom) Simple-Z error when compared to Solartron 1260A results.
Source: By the author.

Most detections with electrical impedance spectroscopy are based on measuring the relative variation against a reference. For example, when quantifying the concentration of an analyte, usually the reference is the impedance spectrum of a ‘blank’ solution without analyte. This means that random errors may be much more compromising than systematic errors. We calculated the standard deviation of the triplicated measurements of Simple-Z, which are shown in **Figure 30**. The impedance magnitude deviation remained under 1% and the phase deviation under 1.5^{o}, both much lower than the errors of **Figure 29**.

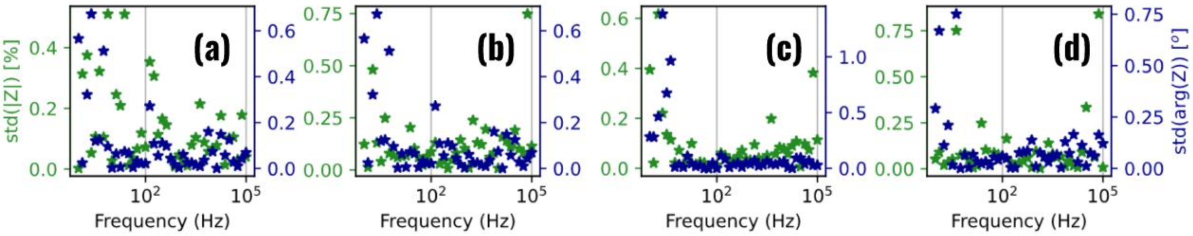

Figure 30: Standard deviations of measurements over each human tissue-equivalent circuit[190–193] ((a) biceps, (b) breast, (c) blood, (d) arm) using Simple-Z.
Source: By the author.

4 USING SIMPLE-Z IN SENSING AND BIOSENSING

4.1 Na_2SO_4 in H_2O (proof of concept)

4.1.1 Motivation

The performance of Simple-Z with the human tissue-equivalent circuits was compatible with detections and quantifications using real samples. Among all the parameters that may affect the impedance of a solution, the concentration of electrolytes is highly relevant. One of the most basic impedance analyses is the quantification of dissolved salt in pure water. As a proof of concept, we aimed to detect and quantify sodium sulfate (Na_2SO_4) using gold interdigitated microelectrodes and we compared the performance with a commercial analyzer.

4.1.2 Methodology

The gold interdigitated microelectrodes were produced using conventional photolithography at the Micro-Fabrication Laboratory (LMF) / Brazilian National Nanotechnology Laboratory (LNNano) / Brazilian National Center for Research in Energy and Materials (CNPEM). The interdigits in these electrodes form a pattern similar to an electrical circuit in parallel, as in parallel plate capacitors.[194–196] They consisted of 50 pairs of 10 µm wide electrodes, 10 µm apart from each other.[21] For the substrate, BK7 glass slides were washed with a neutral detergent to remove impurities and rinsed in ultrapure water, ethanol, and dried under nitrogen (N_2) gas flow. For the electrodes, the substrate was then treated with hexamethyldisiloxane (HMDSO) and positive photoresist AZ4210 deposited by spin coating during 10 and 30 s, respectively. We used a lithographic mask for exposure to UV light for 10 s for photoresist polymerization followed by treatment with tetrabutylammonium. The slides were coated with 20 nm of chromium as an adhesive layer, and then a 150 nm gold layer with the sputtering system BA510 (Balzers).

The electrical measurements were performed using 0 V DC amplitude and 200 mV AC amplitude, applying frequencies between 1 Hz and 100 kHz. We prepared 9 different concentrations of Na_2SO_4 in pure water ranging between 10^{-3} mg/mL and 10 mg/mL. A small volume of 30 µL was placed over the gold interdigitated microelectrodes before each measurement. The impedance spectra were obtained with Simple-Z and Solartron 1260A.

4.1.3 Results

The impedance spectra obtained with Simple-Z and Solartron 1260A are shown as Bode plots in **Figure 31**. They had big similarity in most of the frequency range, with larger deviations in phase within the last frequency decade (10 kHz to 100 kHz).

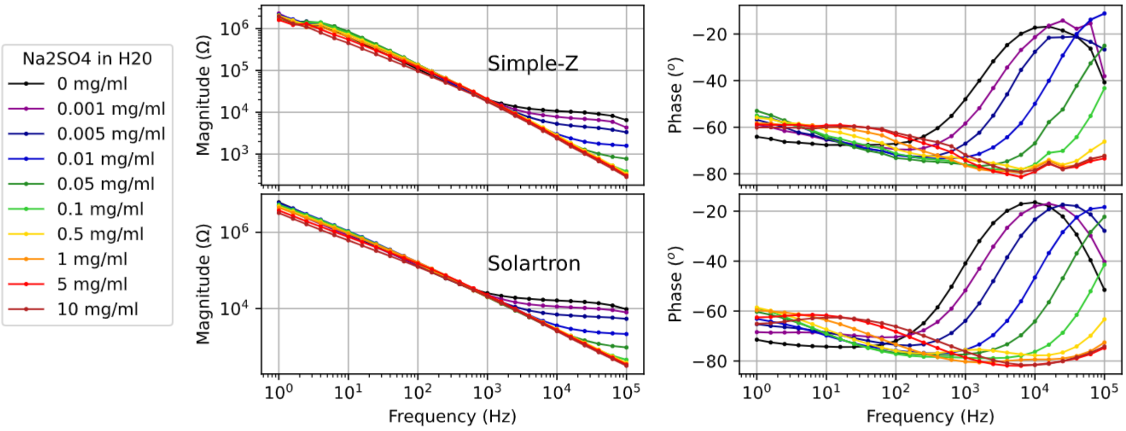

Figure 31: Impedance Bode spectra obtained with Simple-Z and Solartron 1260A over solutions of Na_2SO_4 in pure water.

Source: By the author.

Each frequency of the spectra can be seen as a dimension and so each spectrum represents a point in this multi-dimensional space. Upon visual inspection to distinguish the different samples in **Figure 31**, we chose the impedance phase at the frequencies 100 Hz, 1 kHz, 10 kHz and 100 kHz. We calculated the Euclidean distances from the blank measurement and generated the calibration curves presented on the left of **Figure 32**. The sensitivity obtained with Solartron 1260A was 34.36 versus 33.27 with Simple-Z. On the right of **Figure 32** we compared the distances obtained with both spectrometers, which ideally would result in angular coefficient and linearity of 1. These were 0.97 and 0.998, respectively, confirming the very high similarity between the measured spectra.

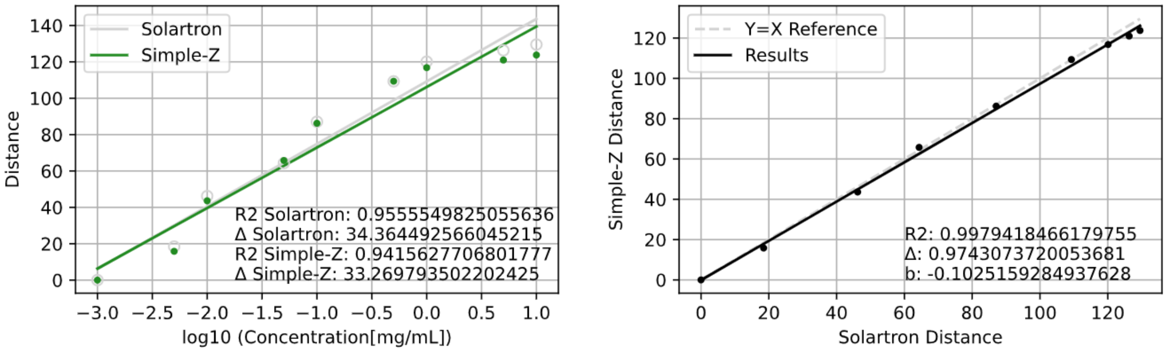

Figure 32: (left) sensitivity analysis using impedance phase at 100 Hz, 1 kHz, 10 kHz and 100 kHz and (right) comparison between Simple-Z and Solartron 1260A.

Source: By the author.

4.1.4 Remarks on Validation

We performed an experiment to validate the detection sensitivity of Simple-Z with Na_2SO_4 in pure water. We developed a tetra-dimensional projection for better distinction of the samples and a calibration curve was obtained. In comparing its performance with the commercial spectrometer Solartron 1260A, we found very high similarity. During this experiment we did not monitor all the parameters that might affect the impedance, such as polarization effects and slight temperature variations. However, the equivalent results between Simple-Z and Solartron 1260A represent a success for our purposes.

4.2 Cyanobacteria (proof of concept)

4.2.1 Motivation

Cyanobacteria have ecological, sanitary and public health-related importance. The species *Microcystis aeruginosa* is frequently dominant in cyanobacteria blooms in Brazilian eutrophicated reservoirs[197-198] and is well known for the production of toxins (hepatotoxin) referred to as microcystins.[199] As an example of the impact of microcystins in public health, one may mention the worldwide famous case from Caruaru (Pernambuco, Brazil), where 60 people died after undergoing hemodialysis with water contaminated with microcystins.[200] This episode was so significant for the Brazilian public health that forced the country to be the first to establish a maximum limit of microcystins (1 µg/L) and the monitoring of cyanobacteria in public consumption water. These limits are now established in resolutions by the Brazilian Health Ministry.[201] Furthermore, the Brazilian National Council of Environment (CoNaMA) also published a resolution that determines the acceptable limits of cyanobacterial density for specific types of rivers and reservoirs used for public consumption.[202] For example, a Class II damp should have a maximum of 50 kCells/mL of cyanobacteria at the source (raw) water.[202] Currently this analysis is done using optical microscopes and performing a tedious and time-consuming manual counting, which takes several minutes and even hours. Creating an automatic counting method would have a huge impact in several sanitary processes. The experiment to be reported here is aimed at using electrical impedance spectroscopy to obtain a calibration curve between impedance and cyanobacterial *Microcystis aeruginosa* concentration.

4.2.2 Methodology

To obtain calibration curves for quantifying cyanobacteria, we used a strain of the species *Microcystis aeruginosa* Kützing (code CCMA-666), kept in the laboratory of BioToxicology of Continental Waters and Effluents (BioTACE) at the School of Engineering of São Carlos (EESC) at the University of São Paulo (USP). *M. Aeruginosa* is a cyanobacteria that lives in fresh water with a predominantly colonial behaviour in natural environments.[203] When in a culture medium, they may show unicellular morphology (disperse in isolated cells). The culture medium used was Artificial Sputum Medium 1 (ASM-1),[204] frequently used for cyanobacteria,[205] in controlled conditions of luminosity (60 µmol $m^{-2}s^{-1}$), photoperiod (12 h clear:12 h dark), pH (7.4) and temperature (25 ^{o}C). The initial inoculum of cells from which the dilutions utilized in the calibrations were obtained had its density of cyanobacteria determined as $8.10x10^{6}$ Cells/mL by manual counting inside a Neubauer chamber (BOECO), using an optical trinocular microscope BX51 (Olympus). The counting estimated error e = 2 / sqrt(N) was based on assuming a random distribution of cells in the counting fields and considers a confidence interval of 95%.[206-207] The resulting error under 10% was considered as acceptable.[205] To simulate cultures with different cyanobacterial concentrations, we first extracted 10 mL from the culture and filtered it to remove all cells from the medium. Then we used it to dissolve a second 2 mL extraction into 8 concentrations ranging down to $4.94x10^{2}$ Cells/mL.

In this case selectivity was not essential, once we already knew the type of cells inside the culture. Thus we used the same type of sensor as for the Na_2SO_4 detection (gold interdigitated microelectrodes) and the electrical measurements were performed with Simple-Z using 200 mV AC amplitude with frequencies between 1 Hz and 100 kHz. The measurements were performed from the lowest to the highest concentrations, using three sensors with equal design.

4.2.3 Results

Simple-Z is currently designed to measure impedance magnitudes between 100 Ω and 1 MΩ, meaning that any result outside this range has not validated accuracy. The impedance magnitude spectra obtained are presented in **Figure 33**, where it can be seen that the results of all three sensors stayed within the impedance limits for the frequencies between 6.3 Hz and 100 kHz.

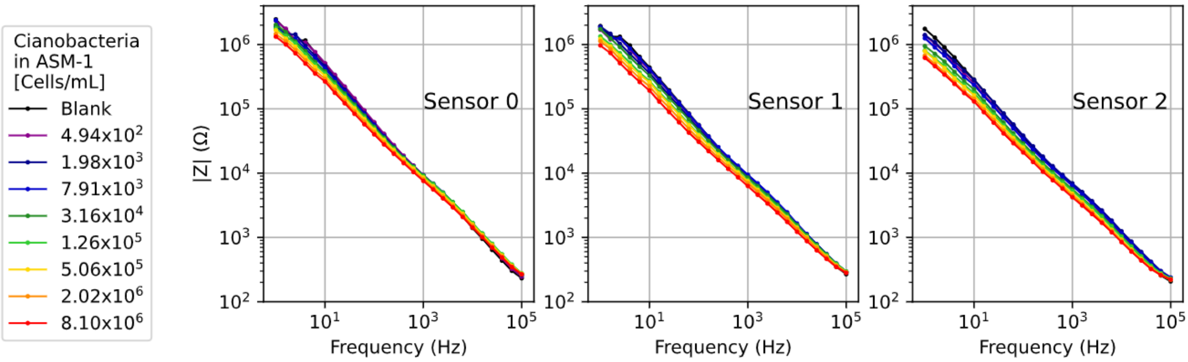

Figure 33: Impedance magnitude spectra of nine Na_2SO_4 concentrations with three sensors with equal design. Source: By the author.

The usual representation of Z, as a complex value, is with its Cartesian coordinates resistance R = Re(Z) and reactance X = Im(Z) or its polar coordinates magnitude |Z| = sqrt(R^2+X^2) and phase Θ_Z = atan(X, R). Another common parameter resulting from a non-linear conversion of Z is the admittance Y = Z^{-1}, with its Cartesian coordinates conductance G = Re(Y) and susceptance B = Im(Y) and its consequential polar coordinates |Y| and Θ_Z. Seeking for a highly sensitive detection, the normalized [0,1] impedance spectra (averaging among the three sensors) were converted to these 8 parameters, as shown in **Figure 34**. The highest variation along the spectra can be observed in G.

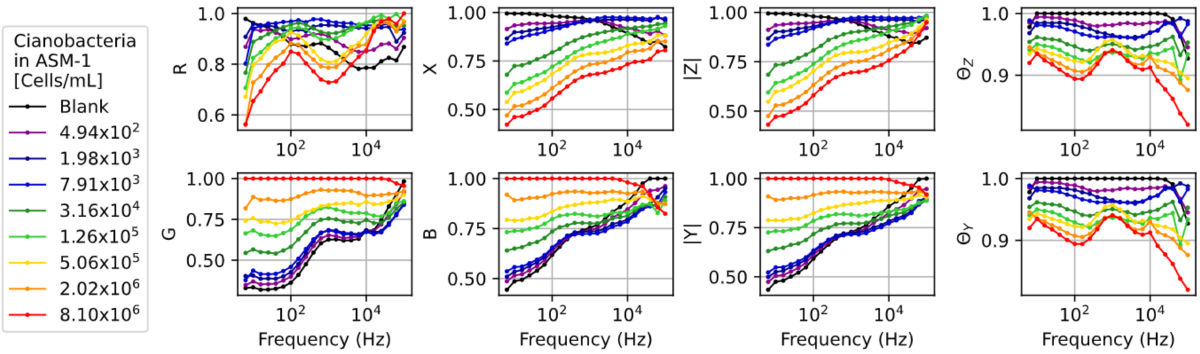

Figure 34: Normalized spectra averaging the three sensors and using eight different impedance parameters. Source: By the author.

It is practical to relate concentration values with a measurable value at a single frequency, instead of using the whole spectrum, speeding up the measurement and the data processing. **Figure 35**, generated with the PexSensorsWeb software, shows the normalized [0,1] G results of the samples represented with the Parallel Coordinates technique. The distinction ability is measured with S, presented over each frequency value as a color bar. It goes from a minimum of -1 to a maximum of 1. The highest S values occurred between 6.3 Hz and 251 Hz.

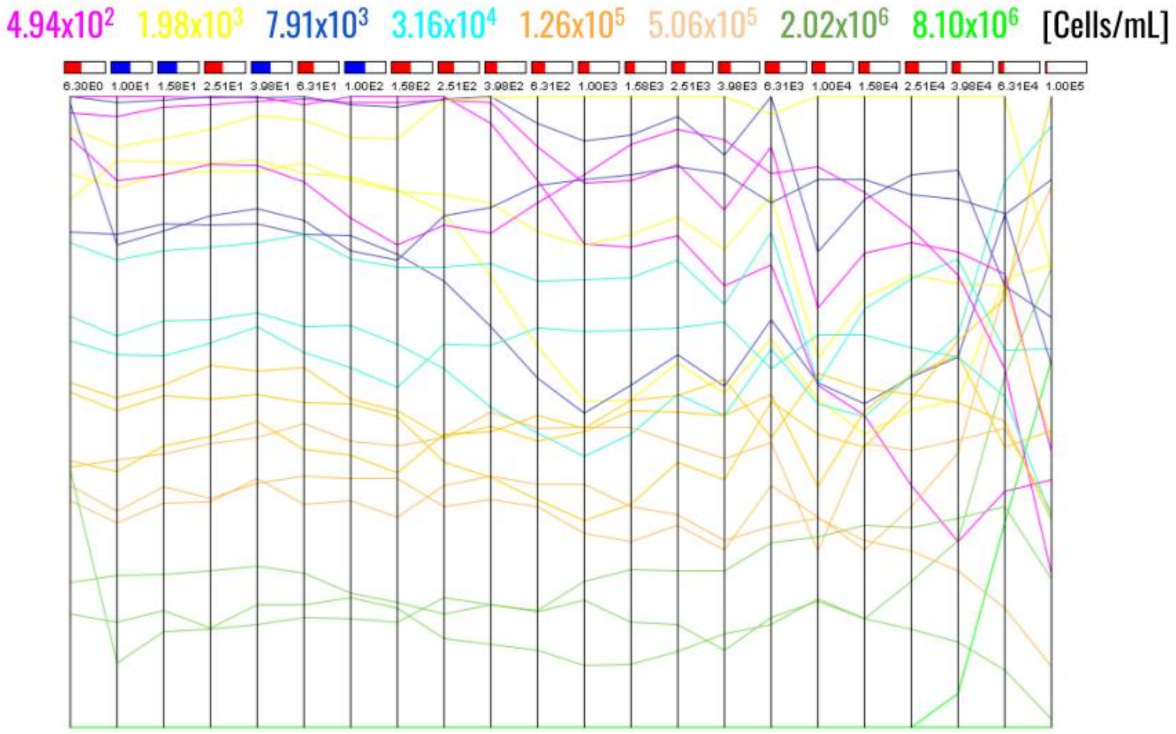

Figure 35: Normalized conductance results of the sample represented with parallel coordinates.
Source: By the author.

Within this frequency range, using the PExSensors Projection Explorer 1.6.3 software, we generated the IDMAP projection in **Figure 36**. In this case, the G spectra of the samples were divided by the spectrum of the blank G_0 of the corresponding sensor. Distinction can be made from 2^{-10}P to P, where P = 8.095 MCells/mL, while the 3 lowest concentrations were not distinguishable.

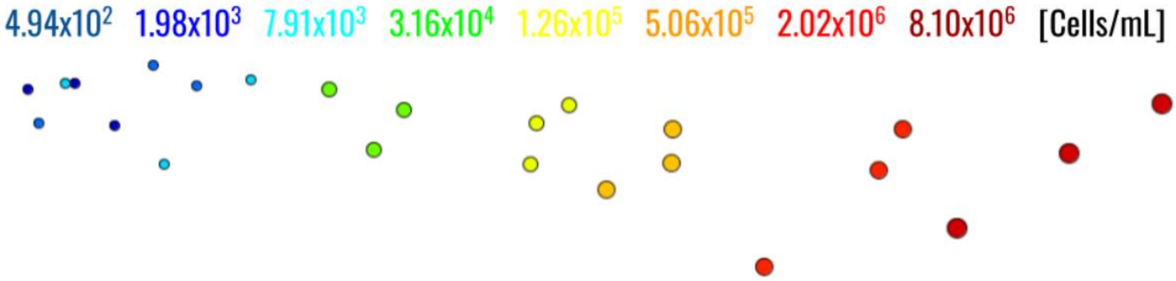

Figure 36: IDMAP of conductance spectra of nine concentrations with three sensors with equal design.
Source: By the author.

Using the average of G/G_0 of the three sensors for the distinguishable concentrations, we performed a linear regression for each frequency of interest. The spectrum of this sensitivity (Δ) is presented in **Figure 37**. The highest value, of 0.5959, was obtained at 25.1 Hz.

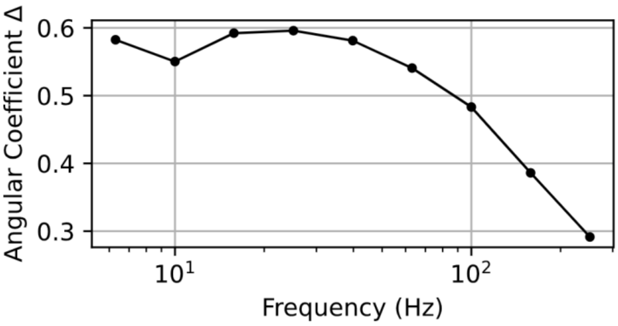

Figure 37: The detection sensitivity spectrum for concentrations 2^{-10}P to P (P = 8.095 MCells/mL). Source: By the author.

We obtained the highest sensitivity (0.596) by using the conductance G = Re (Z^{-1}) at the frequency of 25.1 Hz, with a limit of detection of 7.91×10^3 Cells/mL. The calibration curve is shown in **Figure 38**, which also shows high linearity (0.996) in the detection range.

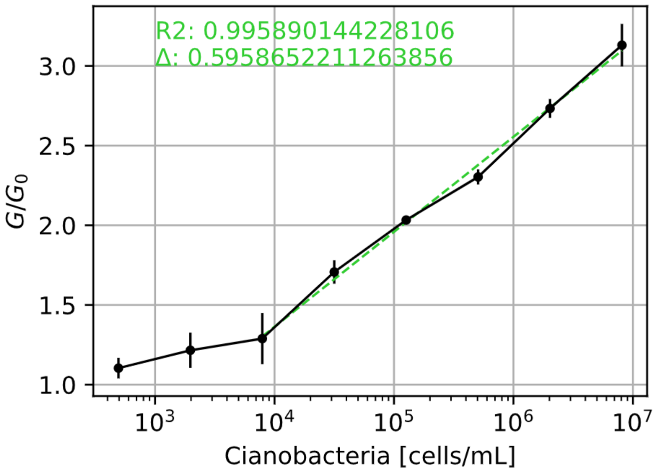

Figure 38: Calibration curve of relative conductance versus cyanobacteria concentration at 25.1 Hz. Source: By the author.

4.2.4 Remarks on Validation

In this experiment we aimed to validate Simple-Z for detecting cyanobacteria cells. We analyzed the spectra using Bode plots, parallel coordinates and IDMAP techniques, and found 25.1 Hz as the most sensitive frequency for the detection. During this experiment we did not monitor all the parameters that might affect the impedance, such as polarization effects and slight temperature variations. Therefore, these are preliminary results for this application and further experiments should be done to confirm if this technique is sufficient for cell quantification.

4.3 SARS-CoV-2

Most of the content of this section can be found in reference.[145]

4.3.1 Motivation

The challenges brought to humanity by the CoViD-19 (Coronavirus disease 2019) pandemic have made it clear that low-cost and easily deployable methods are essential for clinical diagnosis.[208] Early diagnosis of the severe acute respiratory syndrome coronavirus 2 (SARS-CoV-2)[209-210] has been essential for pandemic management[211] and this is mostly performed by real-time PCR (RT-PCR).[212-213] Unfortunately, RT-PCR tests require several hours of sophisticated laboratory equipment and specialized professionals. The RT-PCR method is, therefore, inadequate for low-income countries or remote places with limited resources.[214–216] Other molecular technologies to detect genetic material such as loop-mediated isothermal amplification (LAMP)[217] and clustered regularly interspaced short palindromic repeats (CRISPR)[218-219] suffer from similar limitations. Alternatively, serological tests using ELISA[220-221] and immunosensors[222–226] detect antibodies produced by the infected person. It is worth mentioning that SARS-CoV-2 diagnosis by IgG/IgM screening is not sensitive in the first 1–2 weeks after initial infection, therefore incompatible with early diagnosis of just infected or asymptomatic patients. Hence, public policies to isolate the spreaders cannot rely on this type of test. It seems that genosensors may be a long-term solution for mass testing of diseases requiring sensitive detection of genetic material. Genosensors are biosensors based on nucleic acid which detect single-strand DNA (ssDNA), ribonucleic acid (RNA),[227-228] hairpin DNA, nucleic acid aptamers, and locked nucleic acids (LNAs), depending on the target molecule.[145] In fact, genosensors have long been used in research laboratories and other settings to diagnose various diseases, including SARS, as described in review papers.[9,229-230] However, these sensors have failed to reach the market with mass production, which could considerably enhance the capability of managing this CoViD-19 pandemic efficiently. In our survey of the literature, we identified some sensors developed for SARS-CoV-2, but none of them relies on an electrical transducing principle. Optical detection of ssDNA SARS-CoV-2 sequences was reported with a detection limit of 0.22 pM by using localized surface plasmon resonance (LSPR) spectra.[231] In another work, optical detection of SARS-CoV-2 pseudovirus particles was demonstrated using a gold plasmonic nanocup array functionalized with antibodies, and sensitivity of 370 virus particles/mL.[232] Surface plasmon resonance (SPR) sensors were employed to detect nucleocapsid antibodies against SARS-CoV-2 with a detection limit of 1 µg/mL.[233] An effective diagnosis may be reached by detecting the spike protein of SARS-CoV-2, as it has been done using a field-effect transistor (FET)-based biosensor with a detection limit of 1.6 101 pfu/mL and 2.42x10^2 copies/mL for culture medium and clinical samples, respectively.[234]

In this work, we report on a genosensor produced with an active layer of immobilized ssDNA on a matrix of a SAM. Detection was performed with a complementary ssDNA sequence from the SARS-CoV-2 genome, which mimics the GU280 gp10 gene of the SARS-CoV-2 virus (coding the viral nucleocapsid phosphoprotein). An analysis of possible false positives was made using a non-complementary sequence and other non-related DNA sequences. Our primary purpose is to generate low-cost technology for point-of-care SARS-CoV-2 early diagnosis.

4.3.2 Methodology

The reagents were of analytical grade and used without further purification. Potassium chloride (KCl), sodium chloride (NaCl), magnesium chloride ($MgCl_2$), anhydrous sodium phosphate dibasic (Na_2HPO_4), anhydrous potassium phosphate monobasic (KH_2PO_4), anhydrous potassium ferricyanide ($K_3Fe(CN_6)$), and trihydrate potassium ferrocyanide ($K_3Fe(CN_6)$) were obtained from Synth. N-(3-Dimethylaminopropyl)-N'-ethylcarbodiimide hydrochloride (EDC), N-hydroxysuccinimide (NHS), ethanolamine and 11-mercaptoundecanoic acid (11-MUA) were purchased from Sigma-Aldrich. Highpurity deionized water (resistivity of 18.2 MΩ/cm) was obtained from a Milli-Q system (Millipore). The SARS-CoV-2 chloroplast DNA (cpDNA) sequences used as a probe were synthesized by SigmaAldrich, while the target complementary and non-complementary sequences were synthesized by Exxtend. Phosphate buffered saline (PBS) solutions were prepared with 137x10^{-3} M NaCl, 10x10^{-3} M Na_2HPO_4, 1.7x10^{-3} M KH_2PO_4, and 2.7x10^{-3} M KCl (pH 7.4), with addition of 1.0x10^{-3} M $MgCl_2$ (PBS/$MgCl_2$ solution).

The gold interdigitated electrodes, fabricated according to the method descripted in section "4.1 Na_2SO_4 in H_2O (proof of concept)", were coated with a SAM of 11-MUA (5.0x10^{-3} M) during 24 h in ethanol at room temperature. A solution of 100x10^{-3} M EDC and 100x10^{-3} M NHS was used for 30 min at room temperature in water to increase the attachment of cpDNA probes to carboxylic groups of thiol sites. Then, these devices were immersed in a 1.0x10^{-3} M PBS/$MgCl_2$ solution (1.0x10^{-6} M) containing the NH2-cpDNA for 12 h at room temperature. The probe had the sequence 5'-5AmMC6/ATTTCGCTGATTTTGGGGTC (SigmaAldrich).

A genosensor is based on nucleic acid hybridization whose biological basis is the formation of a double helix that is thermodynamically stabilized by hydrogen bonds. The double helix can be formed by two molecules of ssDNA, RNA/RNA duplexes, or even DNA/RNA hybrids. In this conformation, the two antiparallel and complementary single stranded molecules (either DNA or RNA) acquire a stable form. This specific molecular recognition is explored in this application for the molecular detection of SARS-CoV-2, considering different signal transduction approaches.

Detection experiments were performed with complementary and non-complementary sequences in a concentration range between 1.0×10^{-18} M and 1.0×10^{-6} M diluted in PBS/$MgCl_2$ solutions for the electrical measurements. The positive control for SARS-CoV-2 sequence was 5’-TGATAATGGACCCCAAAATCAGCGAAATGCACCCCGCATTACG-TTTGGTGGACCCTCAGATTCAACTGGCAGTAACCAGA-3’ and the negative control samples sequence was 5’-CCCATCCTCACCATCATCACA CTGGAAGACTCCAGTGG-TAATCTACTGGGACGGAACAGCTTTGAGGTGCGGTTTGTG-30 (Exxtend). The amine terminated ssDNA was chosen based on previous results from our research group.[9,114,144] The negative control sequence was designed from the Homo sapiens TP53 gene, which shows a low identity with the SARS-CoV-2 ssDNA probe designed (40.2% identity between the sequences). We performed a hybridization efficiency analysis for the ssDNA probes, and obtained 0.9998×10^{-10} and 8.4969×10^{-10} for the positive (20.3 kcal/mol) and negative (1.6 kcal/mol) controls, respectively. This analysis was carried out using the mismatch analysis tool.[235-236]

The optimized hybridization process was performed at 85 ^{o}C for 30 min, followed by placing the solution on ice for 5 min. For the impedance spectroscopy measurements, the genosensor was immersed in a solution with 300 µL of each one of the 7 concentrations from 1.0×10^{-18} M to 1.0×10^{-6} M. Control experiments were performed to verify the selectivity of the genosensor, with measurements in DNA samples from Staphylococcus aureus (IDT) (1.0×10^{-6} M), human papillomavirus (HPV16) (Sigma-Aldrich) (4.1×10^{-9} M), Agalactiae (IDT) (1.0×10^{-6} M), and fetal bovine serum (Sigma-Aldrich) (25 mg/dL). Electrical impedance measurements were carried out with the Solartron 1260A, sweeping from 1 Hz to 1 MHz and with AC potential 50 mV. Owing to the potential commercial application of SARS-CoV-2 detection in point-of-care settings, we repeated the electrical impedance analysis using Simple-Z.

4.3.3 Results

The electrical impedance spectra were processed with IDMAP.[237] The mapping strategy strives to reproduce, in a low-dimensional space, the relative pairwise proximities amongst the data samples observed in the original n-dimensional feature space (n is the number of measurements in a spectrum) by minimizing the error. The Euclidean distance $\delta(x_i, x_j)$ between any two samples $x_i = (x_{i1}, x_{i2}, \dots , x_{in})$ and $x_j = (x_{j1}, x_{j2}, \dots , x_{jn})$ is computed as a proxy of their dissimilarity, and the IDMAP strategy is applied to project the samples into a two-dimensional feature space, for visualization purposes. It produces a novel representation of samples x_i and x_j as $y_i = (y_{i1}, y_{i2})$ and $y_j = (y_{j1}, y_{j2})$. **Equation 1** expresses the error to be minimized for a pair of samples x_i and x_j, where $\delta(y_i, y_j)$ denotes the Euclidean distance computed in the reduced space, and δ_{max} and δ_{min} denote the maximum and minimum distance values between the data instances in the original representation space.[11]

$$error_{IDMAP} = \frac{\delta(x_i, x_j) - \delta_{MIN}}{\delta_{MAX} - \delta_{MIN}} - \delta(y_i, y_j) \qquad (1)$$

The genosensor made with a matrix based on 11-MUA was able to detect complementary (positive) sequences in the concentration range between $1.0\text{x}10^{-18}$ and $1.0\text{x}10^{-6}$ M using impedance spectroscopy, as seen in the capacitance $C = \mathrm{Re}((j\ \omega\ Z)^{-1})$ spectra in **Figure 39**. The specific interactions between the cpDNA SARS-CoV-2 and the positive sequence are sufficient to yield measurable differences in the relative capacitance, defined as the difference in capacitance with and without ssDNA SARS-CoV-2 (positive control). The measurements are performed with these electrodes immersed into a liquid sample. Therefore, an electric double-layer will be formed at the interface between the genosensor film and the liquid. The frequency-dependent electrical response in sensors is governed by three types of mechanism.[238-239] At high frequencies, the electrical signal depends mostly on the electrode geometric capacitance while at intermediate frequencies, between 1 kHz and 100 kHz, this response is related to changes at the sensor surface.[240-241] At low frequencies (1 Hz to 1 kHz), the electrical double layer formed at the sensor/electrolyte (sample) interface governs the response, as indicated in the literature[238-239,242] and in previous work from our group.[21,117] Adsorption of the target sequences through hybridization occurs along the film surface, being therefore symmetric with regard to the electrode digits. Since the interdigit distance (10 µm) is considerably larger than the Debye length of the double-layer (of the order of nm), the change in impedance induced by hybridization may be attributed essentially to a change in the double-layer capacitance, in addition to possible molecular reorientation. This assumption is confirmed with the results shown in **Figure 39** where distinction is clear at low frequencies, therefore indicating the relevance of double-layer effects in the detection.

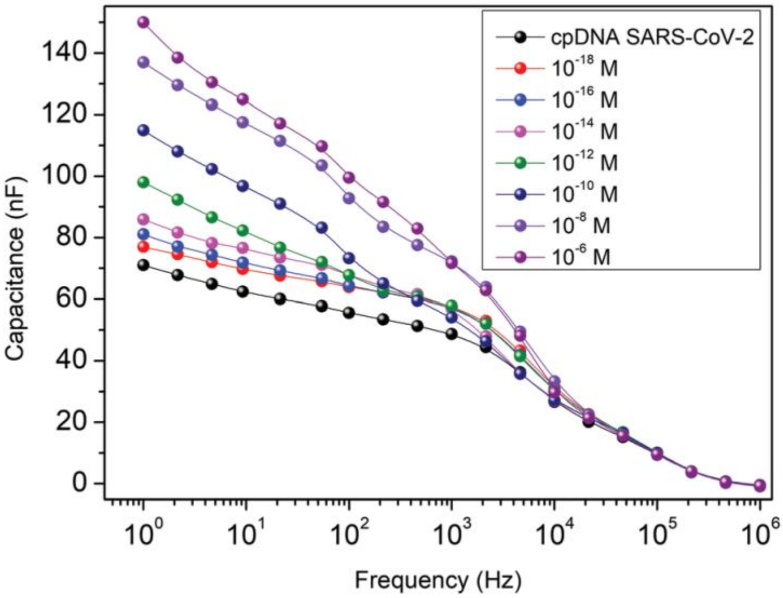

Figure 39: Capacitance spectra obtained for detection of ssDNA SARS-CoV-2 in synthetic samples using a genosensor built with a matrix of 11-MUA SAM under an active layer containing the cpDNA SARS-CoV-2 (probe).

Source: SOARES *et al.*[145]

For practical reasons, one may wish to display the results not in the form of spectra as in **Figure 39**, but with a single capacitance value at a given frequency. Measuring the signal at a single frequency would also facilitate displaying the detection results. We have therefore analyzed the capacitance spectra in **Figure 39** with the Parallel Coordinates visualization technique which is useful to reveal the frequencies responsible for the highest distinction of the different SARS-CoV-2 concentrations. **Figure 40** shows a parallel coordinates plot of the capacitance data. The distinction ability is estimated with S, expressed in **Equation 2**, where n refers to the total number of samples, a_i denotes the average distance between the i^{th} data point and the other data points in the same category as itself, and b_i is the smallest of the average distances computed between the i^{th} data point to the data points in each category distinct from i. S varies in the range [-1, +1] and is useful as an estimate of the cohesion and separability of the different categories of samples. Here we computed its value at each frequency of the measured spectrum. Thus, S ~ -1 indicates the signal at a given frequency is useful for distinction among the samples, while S ~ 0 and S ~ 1 mean, respectively, that the signal is neutral or deleterious for such a distinction.[21,243] In **Figure 40**, the values of S are encoded as small bars at the top of the axis relative to each measured frequency, color coded as follows: blue for positive values, white for S ~ 0, and red for negative values; the length of the filling is proportional to the value. Most frequencies are useful for detection, which leads to an overall S of 0.936 (for all ssDNA SARS-CoV-2 positive samples and frequencies), thus confirming the excellent distinguishing capability of the genosensor. By overall S we mean that it was calculated with all frequencies (not with a single value).

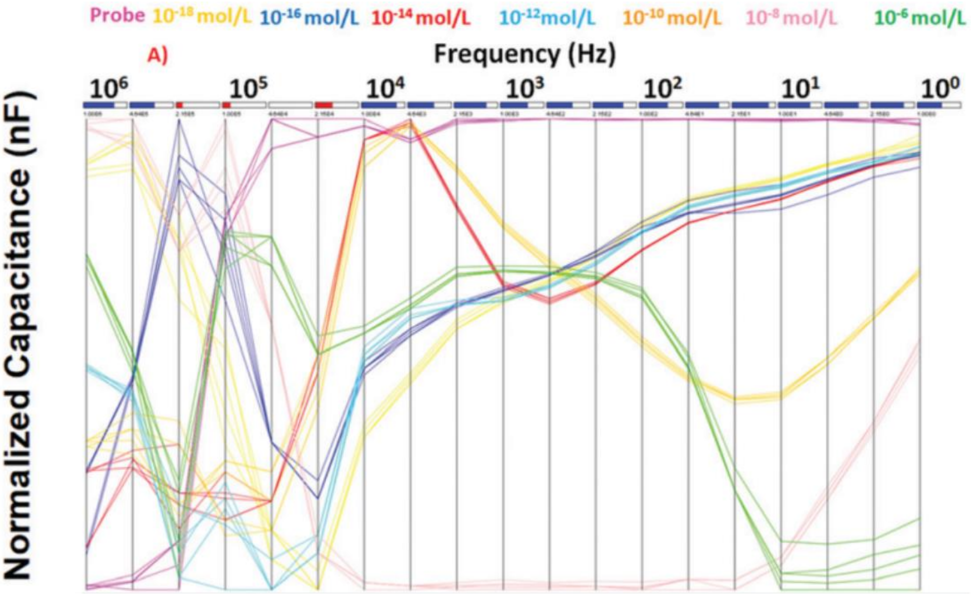

Figure 40: Parallel coordinates plot for the impedance spectroscopy data obtained with 11-MUA genosensor functionalized with an ssDNA SARS-CoV-2 probe.

Source: Adapted from SOARES *et al.*[145]

$$S = \frac{1}{n}\sum_{i=1}^{n}\frac{(b_i-a_i)}{MAX(b_i,a_i)} \tag{2}$$

Assessing the parallel coordinates plot in conjunction with S is also useful to determine the best frequency at which a calibration curve can be taken. From the values estimated for S, we chose 1 Hz and the capacitance versus SARS-CoV-2 concentration in the logarithm scale is shown in **Figure 41**. Taking the initial linear part of the curve, we obtained a detection limit of detection LoD = 3 SD / slope of 0.5 aM using the International Union of Pure and Applied Chemistry (IUPAC) recommendation,[244] where the standard deviation (SD) is of 10 blank curves. This LoD corresponds to 0.3 copies/µL, which is lower than values typically obtained using RT-PCR kits (1.25 copies/µL).[245] Hence, the genosensor may be applied to biological samples, though further studies are required to confirm whether the performance will remain in complex samples.

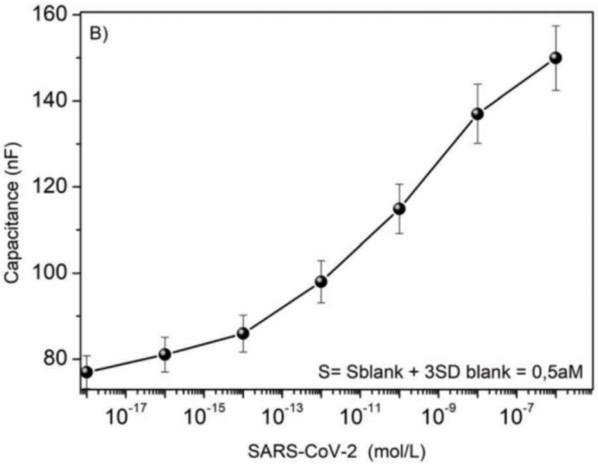

Figure 41: Calibration curve with the capacitance at 1 Hz plotted versus the concentration of SARS-CoV-2. Source: Adapted from SOARES *et al.*[145]

The high sensitivity of the genosensor was our first goal, and this could be feasible with impedance data at a single frequency as previously shown. But selectivity is also crucial, which requires a series of control experiments that generate tens of spectra. In order to analyze these spectra, we plotted the capacitance data with the multidimensional projection IDMAP in **Figure 42**. It is relevant that the spectra for the complementary sequence (positive for SARS-CoV-2) can be distinguished from those of negative sequences, from PBS, fetal bovine serum (FBS), and other DNA biomarkers such as DNA samples from Staphylococcus aureus, HPV16, and Agalactiae.

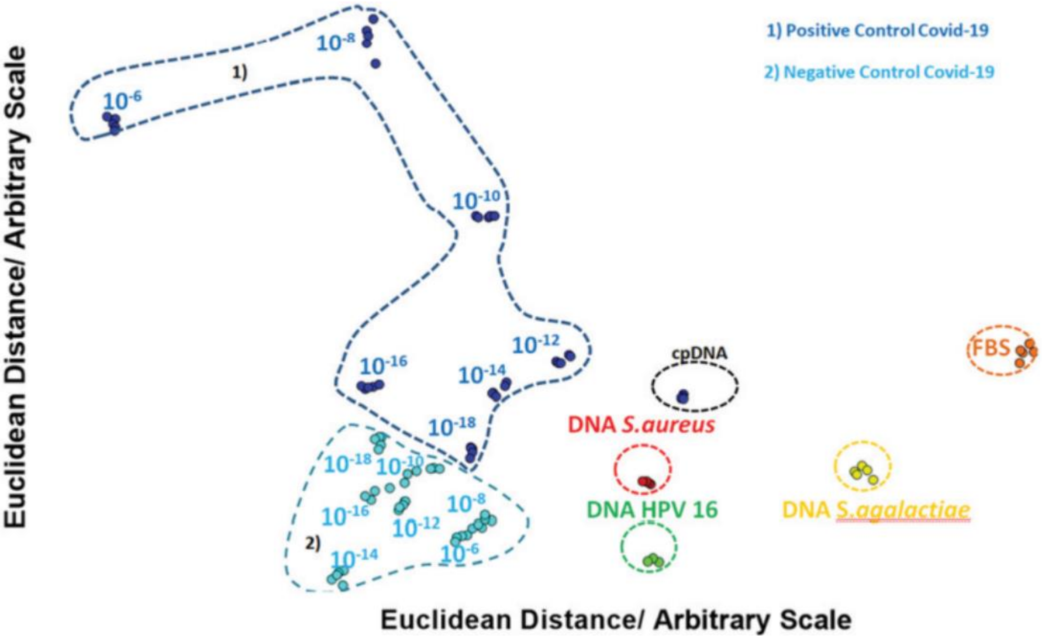

Figure 42: IDMAP projection of capacitance spectra for samples with ssDNA SARS-CoV-2 at various concentrations and DNA S. *Agalactiae*, cpDNA, DNA S. *Aureus* and HPV16, measured using genosensors constructed with 11-MUA SAM coated with ssDNA SARS-CoV-2 probe.
Source: SOARES *et al.*[145]

Notice the data points for the control experiments are not in a single cluster, which suggests non-specific adsorption might have occurred for the distinct non-target samples. Distinction of data from control experiments is common for impedance spectroscopy, which is highly sensitive to any change in the interfacial properties.[9,114,144,246] Nevertheless, detection is not compromised if one uses a projection method to establish the differences between clusters. In subsidiary experiments, we verified that positive sequences of SARS-CoV-2 could be detected in impedance spectroscopy measurements performed with Simple-Z, as demonstrated in the IDMAP plot in **Figure 43**. This approach is promising for making the genosensors available in point-of-care diagnosis systems.

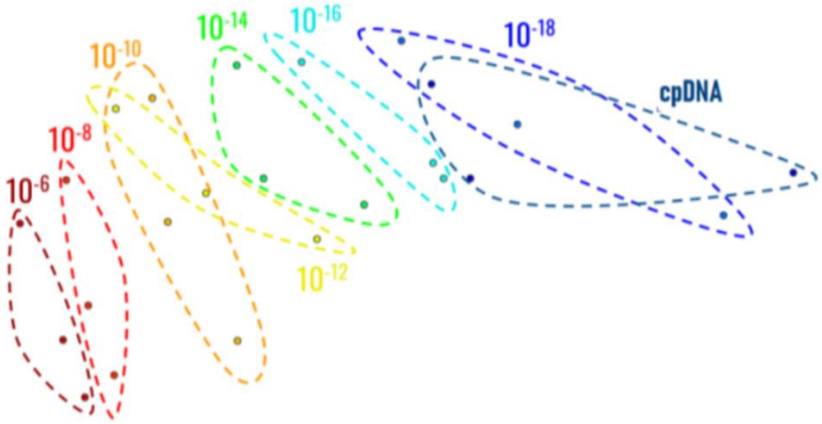

Figure 43: IDMAP projection of the capacitance spectra for cpDNA (Probe) and various ssDNA SARS-CoV-2 concentrations measured with Simple-Z.
Source: Adapted from SOARES *et al.*[145]

4.3.4 Partial Conclusions

A genosensor has been developed which can detect an ssDNA sequence of SARS-CoV-2 using impedance spectroscopy with a detection limit of 0.5 aM. This sensitivity corresponds to 0.3 copies/µL and should suffice to detect the RNA sequence in saliva or other body fluids. The selectivity of the genosensors was verified with control samples, including a negative sequence for SARS-CoV-2 and other DNA biomarkers not related to CoViD-19. The main limitation in this work is associated with the samples analyzed, as the suitability of the genosensor for diagnosis of SARS-CoV-2 in CoViD-19 patients has not been tested. Based on the literature and our own experience with genosensors, we are hopeful that a sensitive, selective diagnosis will be possible. This confirmation will now be pursued by our team, and we also hope other authors will employ the strategies and genosensor architecture for developing efficient diagnostic methods.

5 CONCLUSIONS

The revision of the bibliography suggested that the best option for signal generation and impedance readout for producing low-cost electrical impedance spectroscopy systems is to combine a direct digital synthesizer with a digital or analog discrete Fourier transform calculator. We used the integrated circuit AD5933, which includes both functions, and additional circuits that we developed to overcome its several limitations. We achieved a palm-sized spectrometer (Simple-Z) made 100% of off-the-shelf components with total cost near 100 USD. It is more than 10 times cheaper than commercial spectrometers. Our design works with wide ranges of impedance magnitude (100 Ω to 1 MΩ), alternated current amplitude (10 mV to 1 V) and frequency (1 Hz to 100 kHz). Furthermore, we developed a graphical user interface to simplify its usage. A performance analysis was done using human tissue-equivalent circuits made of resistors and capacitors, resulting in impedance deviations under 1% in magnitude and 1.5^{o} in phase. Its functionality was validated in two proof-of-concept sensing experiments (Na_2SO_4 and cyanobacteria *Microcystis aeruginosa*) and one biosensing work for detecting SARS-CoV-2. Five units of Simple-Z were fabricated to be used by researchers of our group. It represents a bridge over the technological gap between the diversification of biosensors and the development of integrated prototypes to be applied in the field. The prototypical units fabricated in this Master Project have been tested, and Simple-Z is ready for scaling up in mass manufacturing. We envisage that Simple-Z will be useful for applications in sensing and biosensing, as demonstrated here, and in teaching laboratories of universities. Nowadays, impedance spectroscopy experiments are not normally performed in teaching at undergraduate levels owing to the high cost of providing dozens of instruments at once for a class of students. With Simple-Z, this will be feasible.

REFERENCES

1 SIQUEIRA, J.R. *et al.* Immobilization of biomolecules on nanostructured films for biosensing, *Biosensors and Bioelectronics*, v.25, p.1254–63, 2010. DOI:10.1016/J.BIOS.2009.09.043.

2 VALER, J.C. *et al.* Development of a reusable atomic oxygen sensor using zinc oxide thick films, *IEEE Sensors Journal*, v.13, n.8, p.3046–52, 2013. DOI:10.1109/JSEN.2013.2257730.

3 POLESE, D. *et al.* AC characterization of nitrate intercalated layered double hydroxides gas sensors, *Proceedings of IEEE Sensors*, p.1–3, 2017. DOI:10.1109/ICSENS.2017.8234323.

4 NASIR, M. *et al.* Effect of diffusion on impedance measurements in a hydrodynamic flow focusing sensor, *Lab on a Chip*, v.10, p.2787–95, 2010. DOI:10.1039/C005257D.

5 AGUIR, K. *et al.* Impedance spectroscopy to identify the conduction mechanisms in WO3 sensors, *Proceedings of IEEE Sensors*, p.267–70, 2006. DOI:10.1109/ICSENS.2007.355771.

6 HASAN, N. *et al.* Characterization of nanodiamond seeded interdigitated electrodes using impedance spectroscopy of pure water, *Electrochimica Acta*, v.210, p.375–82, 2016. DOI:10.1016/J.ELECTACTA.2016.05.053.

7 YAN, X.F. *et al.* Progress of interdigitated array microelectrodes based impedance immunosensor, *Chinese Journal of Analytical Chemistry*, v.39, n.10, p.1601–10, 2011. DOI:10.1016/S1872-2040(10)60478-1.

8 MAZZEO, B.A.; FLEWITT, A.J. Observation of protein-protein interaction by dielectric relaxation spectroscopy of protein solutions for biosensor application, *Applied Physics Letters*, v.90, n.123901, p.1–3, 2007. DOI:10.1063/1.2716350.

9 SOARES, J.C. *et al.* Detection of the prostate cancer biomarker PCA3 with electrochemical and impedance-based biosensors, *ACS Applied Materials and Interfaces*, v.11, p.46645–50, 2019. DOI:10.1021/ACSAMI.9B19180.

10 BAIDILLAH, M.R. *et al.* Electrical impedance spectro-tomography based on dielectric relaxation model, *IEEE Sensors Journal*, v.17, n.24, p.8251–62, 2017. DOI:10.1109/JSEN.2017.2710146.

11 PAULOVICH, F. V. *et al.* Information visualization techniques for sensing and biosensing, *The Analyst*, v.136, n.7, p.1344, 2011. DOI:10.1039/C0AN00822B.

12 KATZ, E.; WILLNER, I. Probing biomolecular interactions at conductive and semiconductive surfaces by impedance spectroscopy: Routes to impedimetric immunosensors, DNA-sensors, and enzyme biosensors, *Electroanalysis*, v.15, n.11, p.913–47, 2003. DOI:10.1002/ELAN.200390114.

13 CAYTAK, H. *et al. Bioimpedance spectroscopy processing and applications*, New York, USA: Elsevier, 2019, v.3, Available from: http://dx.doi.org/10.1016/B978-0-12-801238-3.10884-0. Access at: 12.01.2022.

14 MILLER, J.C.; HORVATH, S.M. Impedance cardiography, *Psychophysiology*, v.15, n.1, p.80–91, 1978. DOI:10.1111/J.1469-8986.1978.TB01340.X.

15 JIANG, H. *et al.* Application of electronic tongue for fresh foods quality evaluation: A review, *Food Reviews International*, v.34, n.8, p.746–69, 2018. DOI:10.1080/87559129.2018.1424184.

16 CALLEGARO, L. *Electrical impedance:* principles, measurement and applications, New York, USA: CRC Press, 2013.

17 MORAES, M.L. *et al.* Strategies to optimize biosensors based on impedance spectroscopy to detect phytic acid using layer-by-layer films, *Analytical Chemistry*, v.82, n.8, p.3239–46, 2010. DOI:10.1021/AC902949H.

18 HUANG, J. *et al.* Review of non-invasive continuous glucose monitoring based on impedance spectroscopy, *Sensors and Actuators A*, v.311, n.112103, p.1–9, 2020. DOI:10.1016/J.SNA.2020.112103.

19 XU, Y. *et al.* A review of impedance measurements of whole cells, *Biosensors and Bioelectronics*, v.77, p.824–36, 2016. DOI:10.1016/J.BIOS.2015.10.027.

20 THAPA, A. *et al.* Carbon nanotube matrix for highly sensitive biosensors to detect pancreatic cancer biomarker CA19-9, *ACS Applied Materials and Interfaces*, v.9, n.31, p.25878–86, 2017. DOI:10.1021/ACSAMI.7B07384.

21 SOARES, J.C. *et al.* Supramolecular control in nanostructured film architectures for detecting breast cancer, *ACS Applied Materials and Interfaces*, v.7, n.22, p.11833–41, 2015. DOI:10.1021/ACSAMI.5B03761.

22 SOARES, A.C. *et al.* Controlled molecular architectures in microfluidic immunosensors for detecting Staphylococcus aureus, *The Analyst*, v.145, n.18, p.6014–23, 2020. DOI:10.1039/D0AN00714E.

23 LIU, X. *et al.* High-throughput impedance spectroscopy biosensor array chip, *Philosophical Transactions of the Royal Society A*, v.372, n.20130107, p.1–14, 2014. DOI:10.1098/RSTA.2013.0107.

24 SANCHEZ-GONZALEZ, A. *et al.* A multichannel FRA-based impedance spectrometry analyzer based on a low-cost multicore microcontroller, *Electronics*, v.8, n.38, p.1–23, 2019. DOI:10.3390/ELECTRONICS8010038.

25 KEYSIGHT TECHNOLOGIES. *Impedance measurement handbook:* a guide to measurement technology and techniques, 4th ed. s.d. Available from: https://assets.testequity.com/te1/Documents/pdf/keysight/impedance-measurement-handbook.pdf. Access at: 11.04.2022.

26 SIT, E.W. *et al. Sensors and instrumentation, aircraft/aerospace and energy harvesting*, Cham, Switzerland: Springer, 2018, v.8.

27 SAIRIN, M.A. *et al.* Design of portable wireless impedance spectroscopy for sensing lard as adulterant in palm oil, *IOP Conference Series*, v.230, n.1, p.0–9, 2019. DOI:10.1088/1755-1315/230/1/012021.

28 KOERNER, L.J.; SECORD, T.W. An embedded electrical impedance analyzer based on the AD5933 for the determination of voice coil motor mechanical properties, *Sensors and Actuators A*, v.295, p.99–112, 2019. DOI:10.1016/J.SNA.2019.05.037.

29 FERREIRA, J. *et al.* AD5933-based spectrometer for electrical bioimpedance applications, *Journal of Physics*, v.224, n.1, 2010. DOI:10.1088/1742-6596/224/1/012011.

30 HARDER, R. *et al.* Smart multi-frequency bioelectrical impedance spectrometer for BIA and BIVA applications, *IEEE Transactions on Biomedical Circuits and Systems*, v.10, n.4, p.912–9, 2016. DOI:10.1109/TBCAS.2015.2502538.

31 WANG, J. *Design and implementation of an impedance analyzer based on Arduino Uno*. KTH, Stockholm, Sweden, 2015. Available from: https://www.diva-portal.org/smash/get/diva2:800585/FULLTEXT01.pdf. Access at: 11.04.2022.

32 AL-ALI, A.A.A. *Design and implementation of a magnitude only bio-impedance analyzer*. Calgary, Canada: University of Calgary, 2018.

33 ANALOG DEVICES *1 Msps, 12-bit impedance converter, network analyzer:* AD5933 datasheet, Norwood, USA, 2005, Available from: http://www.analog.com/en/rfif-components/direct-digital-synthesis-dds/ad5933/products/product.html. Access at: 12.01.2022.

34 JENKINS, D.M. *et al.* ABE-Stat, a fully open-source and versatile wireless potentiostat project including electrochemical impedance spectroscopy, *Journal of The Electrochemical Society*, v.166, n.9, p.B3056–65, 2019. DOI:10.1149/2.0061909JES.

35 BUSCAGLIA, L.A. *et al.* Roadmap for electrical impedance spectroscopy for sensing: A tutorial, *IEEE Sensors Journal*, v.21, n.20, p.22246–57, 2021. DOI:10.1109/JSEN.2021.3085237.

36 WANG, Y. *et al.* A compact CMOS ring oscillator with temperature and supply compensation for sensor applications, *IEEE Computer Society Annual Symposium on VLSI*, p.267–72, 2014. DOI:10.1109/ISVLSI.2014.15.

37 LINDBERG, E. Oscillators: A simple introduction, *European Conference on Circuit Theory and Design*, p.1–4, 2013. DOI:10.1109/ECCTD.2013.6662285.

38 CARMO, J.P. *et al.* A 4.2 mW 5.7-GHz frequency synthesizer with dynamic-logic (TSPC) frequency divider, *International Conference on Telecommunications*, p.309–12, 2009. DOI:10.1109/ICTEL.2009.5158664.

39 PARK, C.-H.; KIM, B. A low-noise 900 MHz VCO in 0.6 μm CMOS, *IEEE Journal of Solid-State Circuits*, v.34, n.5, p.586–91, 1999. DOI:10.1109/VLSIC.1998.687991.

40 CARMO, J.P.; CORREIA, J.H. RF CMOS transceiver at 2.4 GHz in wearables for measuring the cardio-respiratory function, *Measurement*, v.44, n.1, p.65–73, 2011. DOI:10.1016/J.MEASUREMENT.2010.09.027.

41 LEE, T.H.; HAJIMIRI, A. Oscillator phase noise: A tutorial, *IEEE Journal of Solid-State Circuits*, v.35, n.3, p.326–35, 2000. DOI:10.1109/4.826814.

42 RYBIN, Y.K. Barkhausen criterion for pulse oscillators, *International Journal of Electronics*, v.99, n.11, p.1547–56, 2012. DOI:10.1080/00207217.2012.673153.

43 MEYER, R.G.; SOO, D.C.F. MOS crystal oscillator design, *IEEE Journal of Solid-State Circuits*, v.SC-15, n.2, p.222–8, 1980. DOI:10.1109/JSSC.1980.1051366.

44 PELLERANO, S. *et al.* A 13.5-mW 5-GHz frequency synthesizer with dynamic-logic frequency divider, *IEEE Journal of Solid-State Circuits*, v.39, n.2, p.378–83, 2004. DOI:10.1109/JSSC.2003.821784.

45 GARDNER, F.M. Charge-pump phase-lock loops, *IEEE Transactions on Communications*, v.COM-28, n.11, p.1849–58, 1980. DOI:10.1109/9780470545331.CH4.

46 CARMO, J.P. *et al.* A 3.4-mW 2.4-GHz frequency synthesizer in 0.18 um CMOS. *In:* INTERNATIONAL CONFERENCE ON DESIGN & TECHNOLOGY OF INTEGRATED SYSTEMS IN NANOSCALE ERA, 2009. *Proceedings*[…], Cairo:2009, p.266-269. DOI:10.1109/DTIS.2009.4938068.

47 KIM, J. *et al.* Lock-in amplifier-based impedance detection of tissue type using a monopolar injection needle, *Sensors*, v.19, n.21, p.1–9, 2019. DOI:10.3390/S19214614.

48 CARMINATI, M. *et al. Impedance spectroscopy for biosensing:* circuits and applications, New York, USA: Springer, 2015.

49 SHERIF, S. *et al.* Integration of tri-polar microelectrodes for performance enhancement of an impedance biosensor, *Sensing and Bio-Sensing Research*, v.28, n.100329, p.1–13, 2020. DOI:10.1016/J.SBSR.2020.100329.

50 FLATSCHER, M. *et al.* Measurement of complex dielectric material properties of ice using electrical impedance spectroscopy, *Proceedings of IEEE Sensors*, p.1–3, 2016. DOI:10.1109/ICSENS.2016.7808533.

51 SURBER, J.; MCHUGH, L. Single-chip direct digital synthesis vs. the analog PLL, *Analog Dialogue*, v.30, n.3, p.12–3, 1996.

52 DANIELI, D. Microcontroller provides an alternative to DDS, *EE Times*, p.51–2, 2011. Available from: https://www.eetimes.com/microcontroller-provides-an-alternative-to-dds/#:~:text=Audio%20and%20low%2Dfrequency%20circuit,using%20these%20specialized%20integrated%20circuits. Access at: 12.04.2022.

53 FERNANDES, A.V. *et al.* Smart-optical detector CMOS array for biochemical parameters analysis in physiological fluids, *IEEE Transactions on Industrial Electronics*, v.55, n.9, p.3192–200, 2008. DOI:10.1109/TIE.2008.927962.

54 PAL, A. *et al.* Early detection and monitoring of chronic wounds using low-cost, omniphobic paper-based smart bandages, *Biosensors and Bioelectronics*, v.117, p.696–705, 2018. DOI:10.1016/J.BIOS.2018.06.060.

55 CHITTAN, M.V. *et al.* Design and development of cost-effective system for the measurement of dielectric constant of ceramic materials using PIC microcontroller, *MAPAN - Journal of Metrology Society of India*, v.34, n.4, p.443–50, 2019. DOI:10.1007/S12647-019-00313-Z.

56 NAISHADHAM, G. *et al.* Design of low-frequency impedance measurement sensors for respiratory health, *Proceedings of IEEE Sensors*, p.1–4, 2018. DOI:10.1109/ICSENS.2018.8589787.

57 CHEN, C.J. *et al.* Development of a portable impedance detection system for monitoring the growth of mouse L929 cells, *Journal of the Taiwan Institute of Chemical Engineers*, v.43, n.5, p.678–84, 2012. DOI:10.1016/J.JTICE.2012.04.008.

58 HEFELE, M. *et al.* Measuring fluorescence-lifetime and bio-impedance sensors for cell based assays using a network analyzer integrated circuit, *Biosensors and Bioelectronics*, v.129, p.292–7, 2019. DOI:10.1016/J.BIOS.2018.09.053.

59 HAFID, A. *et al.* Full impedance cardiography measurement device using raspberry PI3 and system-on-chip biomedical instrumentation solutions, *IEEE Journal of Biomedical and Health Informatics*, v.22, n.6, p.1883–94, 2018. DOI:10.1109/JBHI.2017.2783949.

60 MARGO, C. *et al.* A four-electrode low frequency impedance spectroscopy measurement system using the AD5933 measurement chip, *Physiological Measurement*, v.34, n.4, p.391–405, 2013. DOI:10.1088/0967-3334/34/4/391.

61 HEDAYATIPOUR, A. *et al.* CMOS based whole cell impedance sensing: Challenges and future outlook, *Biosensors and Bioelectronics*, v.143, n.111600, p.1–13, 2019. DOI:10.1016/J.BIOS.2019.111600.

62 JAFARI, H. *et al.* 16-channel CMOS impedance spectroscopy DNA analyzer with dual-slope multiplying ADCs, *IEEE Transactions on Biomedical Circuits and Systems*, v.6, n.5, p.468–78, 2012. DOI:10.1109/TBCAS.2012.2226334.

63 MANICKAM, A. *et al.* A CMOS electrochemical impedance spectroscopy (EIS) biosensor array, *IEEE Transactions on Biomedical Circuits and Systems*, v.4, n.6, p.379–90, 2010. DOI:10.1109/TBCAS.2010.2081669.

64 ROTTIGNI, A. *et al.* Handheld bio-impedance measurement system based on an instrument-on-chip. *In*: CONFERENCE ON PH.D. RESEARCH IN MICROELECTRONICS AND ELECTRONICS, 2011. *Proceedings*[...], Italy:2011, p.49-52. DOI:10.1109/PRIME.2011.5966214.

65 CARMINATI, M. Advances in high-resolution microscale impedance sensors, *Journal of Sensors*, v.2017, p.1–15, 2017. DOI:10.1155/2017/7638389.

66 KASSANOS, P. *et al.* A CMOS magnitude/phase measurement chip for impedance spectroscopy, *IEEE Sensors Journal*, v.13, n.6, p.2229–36, 2013. DOI:10.1109/JSEN.2013.2251628.

67 MINAS, G. *et al.* On-chip integrated CMOS optical detection microsystem for spectrophotometric analyses in biological microfluidic systems, *In:* IEEE INTERNATIONAL SYMPOSIUM ON INDUSTRIAL ELECTRONICS, 2005. *Proceedings[...],* Dubrovnik:2005, p.1133–8. DOI:10.1109/ISIE.2005.1529083.

68 ANALOG DEVICES *Dual 64-/256-position I2C nonvolatile memory digital potentiometers:* AD5251/AD5252 datasheet, Norwood, USA, 2004, Available from: https://www.analog.com/media/en/technical-documentation/data-sheets/ad5251_5252.pdf. Access at: 12.01.2022.

69 ANALOG DEVICES *Precision, low noise, CMOS, rail-to-rail, input/output operational amplifiers:* AD8605/AD8606/AD8608 datasheet, Norwood, USA, 2002, Available from: https://www.analog.com/media/en/technical-documentation/data-sheets/ad8605_8606_8608.pdf. Access at: 12.01.2022.

70 ANALOG DEVICES *CMOS, low voltage, 2-wire serially controlled, matrix switches:* ADG728/ADG729 datasheet, Norwood, USA, 2012, Available from: https://www.analog.com/media/en/technical-documentation/data-sheets/ADG728_729.pdf.

Access at: 12.01.2022.

71 JILDEH, Z.B. *et al.* Experimental and numerical analyzes of a sensor based on interdigitated electrodes for studying microbiological alterations, *Physica Status Solidi A*, v.215, n.15, p.1–9, 2018. DOI:10.1002/PSSA.201700920.

72 DAIKUZONO, C.M. *et al.* Information visualization and feature selection methods applied to detect gliadin in gluten-containing foodstuff with a microfluidic electronic tongue, *ACS Applied Materials and Interfaces*, v.9, n.23, p.19646–52, 2017. DOI:10.1021/ACSAMI.7B04252.

73 GAJASINGHE, R. *et al.* Label and immobilization free detection and differentiation of tumor cells, *IEEE Sensors Journal*, v.18, n.9, p.3486–93, 2018. DOI:10.1109/JSEN.2018.2813975.

74 MONDAL, D. *et al.* Detection of total bacterial load in water samples using a disposable impedimetric sensor, *IEEE Sensors Journal*, v.20, n.4, p.1712–20, 2020. DOI:10.1109/JSEN.2019.2950422.

75 MOSTAFALU, P.; SONKUSALE, S. A high-density nanowire electrode on paper for biomedical applications, *RSC Advances*, v.5, n.12, p.8680–7, 2015. DOI:10.1039/C4RA12373E.

76 GOPINATH, S.C.B. *et al.* Nanogapped impedimetric immunosensor for the detection of 16 kDa heat shock protein against Mycobacterium tuberculosis, *Microchimica Acta*, v.183, n.10, p.2697–703, 2016. DOI:10.1007/S00604-016-1911-7.

77 VISWAM, V. *et al.* Impedance spectroscopy and electrophysiological imaging of cells with a high-density CMOS microelectrode array system, *IEEE Transactions on Biomedical Circuits and Systems*, v.12, n.6, p.1356–68, 2018. DOI:10.1109/TBCAS.2018.2881044.

78 TURA, A. *et al.* Impedance spectroscopy of solutions at physiological glucose concentrations, *Biophysical Chemistry*, v.129, p.235–41, 2007. DOI:10.1016/J.BPC.2007.06.001.

79 SHIMIZU, F.M. *et al.* Monitoring the surface chemistry of functionalized nanomaterials with a microfluidic electronic tongue, *ACS Sensors*, v.3, n.3, p.716–26, 2018. DOI:10.1021/ACSSENSORS.8B00056.

80 GROSSI, M. *et al.* Automatic ice-cream characterization by impedance measurements for optimal machine setting, *Measurement*, v.45, n.7, p.1747–54, 2012. DOI:10.1016/J.MEASUREMENT.2012.04.009.

81 BORATO, C.E. *et al.* Layer-by-layer films of poly(o-ethoxyaniline), chitosan and chitosan-poly(methacrylic acid) nanoparticles and their application in an electronic tongue, *IEEE Transactions on Dielectrics and Electrical Insulation*, v.13, n.5, p.1101–9, 2006. DOI:10.1109/TDEI.2006.247838.

82 SYAIFUDIN, A.R.M. *et al.* Measurements and performance evaluation of novel interdigital sensors for different chemicals related to food poisoning, *IEEE Sensors Journal*, v.11, n.11, p.2957–65, 2011. DOI:10.1109/JSEN.2011.2154327.

83 MACKAY, S. *et al.* Using impedance measurements to characterize surface modified with gold nanoparticles, *Sensors*, v.17, n.2141, p.1–16, 2017. DOI:10.3390/S17092141.

84 FOO, K.L. *et al.* Au decorated ZnO thin film: application to DNA sensing, *Microsystem Technologies*, v.22, n.4, p.903–10, 2016. DOI:10.1007/S00542-015-2572-X.

85 SRIVASTAVA, S.K. *et al.* A generic microfluidic biosensor of G protein-coupled receptor activation - impedance measurements of reversible morphological changes of reverse transfected HEK293 cells on microelectrodes, *RSC Advances*, v.5, n.65, p.52563–70, 2015. DOI:10.1039/C5RA04976H.

86 CARVALHO, E.R. *et al.* Detection of brominated by-products using a sensor array based on nanostructured thin films of conducting polymers, *Sensors*, v.7, n.12, p.3258–71, 2007. DOI:10.3390/S7123258.

87 ZHENG, X. *et al.* Generic protease detection technology for monitoring periodontal disease, *Faraday Discussions*, v.149, p.37–47, 2011. DOI:10.1039/C005364C.

88 BOAS, L. *et al.* Assessment of the deformability and velocity of healthy and artificially impaired red blood cells in narrow polydimethylsiloxane (PDMS) microchannels, *Micromachines*, v.9, n.8, p.384, 2018. DOI:10.3390/MI9080384.

89 MORAIS, R.M. *et al.* Low cost humidity sensor based on PANI/PEDOT:PSS printed on paper, *IEEE Sensors Journal*, v.18, n.7, p.2647–51, 2018. DOI:10.1109/JSEN.2018.2803018.

90 DAIKUZONO, C.M. *et al.* Paper based electronic tongue-a low-cost solution for the distinction of sugar type and apple juice brand, *Analyst*, v.144, n.8, p.2827–32, 2019. DOI:10.1039/C8AN01934G.

91 MONDAL, D. *et al.* Impedance spectroscopy-based detection of cardiac biomarkers on polyaniline coated filter paper, *IEEE Sensors Journal*, v.17, n.16, p.5021–9, 2017. DOI:10.1109/JSEN.2017.2717701.

92 PAL, A. *et al.* Conformal, waterproof electronic decals for wireless monitoring of sweat and vaginal pH at the point-of-care, *Biosensors and Bioelectronics*, v.160, p.112206, 2020. DOI:10.1016/J.BIOS.2020.112206.

93 TACCOLA, S. *et al.* Toward the use of temporary tattoo electrodes for impedancemetric respiration monitoring and other electrophysiological recordings on skin, *Sensors*, v.21, n.1197, p.1–17, 2021. DOI:10.3390/S21041197.

94 MIHAJLOVIC, V. *et al.* Noninvasive wearable brain sensing, *IEEE Sensors Journal*, v.18, n.19, p.7860–7, 2018. DOI:10.1109/JSEN.2018.2844174.

95 LOPES, P.A. *et al.* Soft bioelectronic stickers: selection and evaluation of skin-interfacing electrodes, *Advanced Healthcare Materials*, v.8, n.1900234, p.1–11, 2019. DOI:10.1002/ADHM.201900234.

96 KIM, J.J.; ANDREW, T.L. Real-time and noninvasive detection of UV-induced deep tissue damage using electrical tattoos, *Biosensors and Bioelectronics*, v.150, p.111909, 2020. DOI:10.1016/J.BIOS.2019.111909.

97 LI, Y.T. *et al.* Application of implantable wireless biomicrosystem for monitoring nerve impedance of rat after sciatic nerve injury, *IEEE Transactions on Neural Systems and Rehabilitation Engineering*, v.21, n.1, p.121–8, 2013. DOI:10.1109/TNSRE.2012.2219883.

98 BAEK, C. *et al.* Fabrication and evaluation of cyclic olefin copolymer based implantable

neural electrode, *IEEE Transactions on Biomedical Engineering*, v.67, n.9, p.2542–51, 2020. DOI:10.1109/TBME.2020.2963992.

99 KOTANEN, C.N.; GUISEPPI-ELIE, A. Characterization of a wireless potentiostat for integration with a novel implantable biotransducer, *IEEE Sensors Journal*, v.14, n.3, p.768–76, 2014. DOI:10.1109/JSEN.2013.2288059.

100 SRINIVASAN, B.; TUNG, S. Development and applications of portable biosensors, *Journal of Laboratory Automation*, v.20, n.4, p.365–89, 2015. DOI:10.1177/2211068215581349.

101 KIM, J. *et al.* Noninvasive alcohol monitoring using a wearable tattoo-based iontophoretic-biosensing system, *ACS Sensors*, v.1, n.8, p.1011–9, 2016. DOI:10.1021/ACSSENSORS.6B00356.

102 BRATOV, A. *et al.* Three-dimensional interdigitated electrode array as a transducer for label-free biosensors, *Biosensors and Bioelectronics*, v.24, n.4, p.729–35, 2008. DOI:10.1016/J.BIOS.2008.06.057.

103 OKYAY, A.K. *et al.* Using nanogap in label-free impedance based electrical biosensors to overcome electrical double layer effect, *Microsystem Technologies*, v.23, n.4, p.889–97, 2017. DOI:10.1007/S00542-015-2764-4.

104 PARK, J. *et al.* Interdigitated and wave-shaped electrode-based capacitance sensor for monitoring antibiotic effects, *Sensors*, v.20, n.18, p.5237, 2020. DOI:10.3390/S20185237.

105 GOMES, H.L. *et al.* A microelectrode impedance method to measure interaction of cells, *Proceedings of IEEE Sensors*, v.2, p.1011–3, 2004. DOI:10.1109/ICSENS.2004.1426344.

106 DUDZINSKI, K. *et al.* Spiral concentric two electrode sensor fabricated by direct writing for skin impedance measurements, *IEEE Sensors Journal*, v.17, n.16, p.5306–14, 2017. DOI:10.1109/JSEN.2017.2719001.

107 KANG, G. *et al.* Differentiation between normal and cancerous cells at the single cell level using 3-D electrode electrical impedance spectroscopy, *IEEE Sensors Journal*, v.12, n.5, p.1084–9, 2012. DOI:10.1109/JSEN.2011.2167227.

108 HUERTA-NUÑEZ, L.F.E. *et al.* A biosensor capable of identifying low quantities of breast cancer cells by electrical impedance spectroscopy, *Scientific Reports*, v.9, n.1, p.6419, 2019. DOI:10.1038/S41598-019-42776-9.

109 SANKHALA, D. *et al.* A four-channel electrical impedance spectroscopy module for cortisol biosensing in sweat-based wearable applications, *SLAS Technology*, v.23, n.6, p.529–39, 2018. DOI:10.1177/2472630318759257.

110 KASHYAP, B. *et al.* Ultra-precision liquid level sensing using impedance spectroscopy and data analytics, *IEEE Sensors Journal*, v.19, n.20, p.9468–78, 2019. DOI:10.1109/JSEN.2019.2925788.

111 ABDOLAHAD, M. *et al.* Silicon nanograss based impedance biosensor for label free detection of rare metastatic cells among primary cancerous colon cells, suitable for more accurate cancer staging, *Biosensors and Bioelectronics*, v.59, p.151–9, 2014. DOI:10.1016/J.BIOS.2014.02.079.

112 CHAUDHURI, C.R.; MONDAL, D. Electrode design improvement for impedance evaluation of biological cell culture under variable frequency low intensity sinusoidal electric field, *IEEE Transactions on Dielectrics and Electrical Insulation*, v.20, n.2, p.382–90, 2013. DOI:10.1109/TDEI.2013.6508738.

113 GUERMAZI, M. *et al.* Investigation of long time beef and veal meat behavior by bioimpedance spectroscopy for meat monitoring, *IEEE Sensors Journal*, v.14, n.10, p.3624–30, 2014. DOI:10.1109/JSEN.2014.2328858.

114 RODRIGUES, V.C. *et al.* Electrochemical and optical detection and machine learning applied to images of genosensors for diagnosis of prostate cancer with the biomarker PCA3, *Talanta*, v.222, p.121444, 2021. DOI:10.1016/J.TALANTA.2020.121444.

115 CABRITA, J. *et al.* Copper protection by phosphonic acid self-assembled monolayers, *Corrosão e Protecção de Materiais*, v.29, n.4, p.114–9, 2010.

116 OLIVEIRA, O.N. *et al.* Nanomaterials for diagnosis: Challenges and applications in smart devices based on molecular recognition, *ACS Applied Materials and Interfaces*, v.6, n.17, p.14745–66, 2014. DOI:10.1021/AM5015056.

117 SOARES, A.C. *et al.* Controlled film architectures to detect a biomarker for pancreatic cancer using impedance spectroscopy, *ACS Applied Materials & Interfaces*, v.7, n.46, p.25930–7, 2015. DOI:10.1021/ACSAMI.5B08666.

118 MALLYA, A.N.; RAMAMURTHY, P.C. Conjugated molecule based sensor for microbial detection in water with E. coli as a case study and elucidation of interaction mechanism, *Electroanalysis*, v.30, n.6, p.1172–83, 2018. DOI:10.1002/ELAN.201800052.

119 AOKI, P.H.B. *et al.* Molecularly designed layer-by-layer (LbL) films to detect catechol using information visualization methods, *Langmuir*, v.29, n.24, p.7542–50, 2013. DOI:10.1021/LA304544D.

120 SWISHER, S.L. *et al.* Impedance sensing device enables early detection of pressure ulcers in vivo, *Nature Communications*, v.6, n.1, p.6575, 2015. DOI:10.1038/NCOMMS7575.

121 CHEN, Z. *et al.* Hybrid learning-based cell aggregate imaging with miniature electrical impedance tomography, *IEEE Transactions on Instrumentation and Measurement*, v.70, p.1–10, 2021. DOI:10.1109/TIM.2020.3035384.

122 YANG, Y. *et al.* A miniature electrical impedance tomography sensor and 3-D image reconstruction for cell imaging, *IEEE Sensors Journal*, v.17, n.2, p.514–23, 2017. DOI:10.1109/JSEN.2016.2631263.

123 ZHANG, C. *et al.* An impedance sensing platform for monitoring heterogeneous connectivity and diagnostics in lab-on-a-chip systems, *ACS Omega*, v.5, n.10, p.5098–104, 2020. DOI:10.1021/ACSOMEGA.9B04048.

124 PARK, J.S. *et al.* 1024-pixel CMOS multimodality joint cellular sensor/stimulator array for real-time holistic cellular characterization and cell-based drug screening, *IEEE Transactions on Biomedical Circuits and Systems*, v.12, n.1, p.80–94, 2018. DOI:10.1109/TBCAS.2017.2759220.

125 PUI, T.S. *et al.* High density CMOS electrode array for high-throughput and automated cell counting, *Sensors and Actuators B*, v.181, p.842–9, 2013.

DOI:10.1016/J.SNB.2013.02.065.

126 OGATA, N. *et al.* An electrical impedance biosensor array for tracking moving cells, *Proceedings of IEEE Sensors*, p.1–4, 2018. DOI:10.1109/ICSENS.2018.8589577.

127 KYOMUK LIM *et al.* A 16-channel neural stimulator with DAC sharing scheme for visual prostheses, *IEEE International Symposium on Circuits and Systems*, v.2, p.1873–6, 2013. DOI:10.1109/ISCAS.2013.6572231.

128 HU, Z. *et al.* Calibration of an AC zero potential circuit for two-dimensional impedimetric sensor matrices, *IEEE Sensors Journal*, v.20, n.9, p.5019–25, 2020. DOI:10.1109/JSEN.2020.2966141.

129 LU, Y.-Y. *et al.* Cell growth characterization using multi-electrode bioimpedance spectroscopy, *Measurement Science and Technology*, v.24, n.3, p.035701, 2013. DOI:10.1088/0957-0233/24/3/035701.

130 CHUNG, J. *et al.* High-density impedance-sensing array on complementary metal-oxide-semiconductor circuitry assisted by negative dielectrophoresis for single-cell-resolution measurement, *Sensors and Actuators B*, v.266, p.106–14, 2018. DOI:10.1016/J.SNB.2018.03.113.

131 WIDDERSHOVEN, F. *et al.* A CMOS pixelated nanocapacitor biosensor platform for high-frequency impedance spectroscopy and imaging, *IEEE Transactions on Biomedical Circuits and Systems*, v.12, n.6, p.1369–82, 2018. DOI:10.1109/TBCAS.2018.2861558.

132 JIANG, Z. *et al.* Development of a portable electrochemical impedance spectroscopy system for bio-detection, *IEEE Sensors Journal*, v.19, n.15, p.5979–87, 2019. DOI:10.1109/JSEN.2019.2911718.

133 SCHWAN, H.P. Linear and nonlinear electrode polarization and biological materials, *Annals of Biomedical Engineering*, v.20, n.3, p.269–88, 1992. DOI:10.1007/BF02368531.

134 BAZANT, M.Z. *et al.* Diffuse-charge dynamics in electrochemical systems, *Physical Review E*, v.70, n.2, p.021506, 2004. DOI:10.1103/PHYSREVE.70.021506.

135 ZOU, Z. *et al.* Functionalized nano interdigitated electrodes arrays on polymer with integrated microfluidics for direct bio-affinity sensing using impedimetric measurement, *Sensors and Actuators A*, v.136, n.2, p.518–26, 2007. DOI:10.1016/J.SNA.2006.12.006.

136 BONANNI, A. *et al.* DNA hybridization detection by electrochemical impedance spectroscopy using interdigitated gold nanoelectrodes, *Microchimica Acta*, v.170, n.3–4, p.275–81, 2010. DOI:10.1007/S00604-010-0358-5.

137 CLAUDEL, J. *et al.* Lab-on-a-chip device for yeast cell characterization in low-conductivity media combining cytometry and bio-impedance, *Sensors*, v.19, n.15, p.3366, 2019. DOI:10.3390/S19153366.

138 DE ARAUJO, A.L.A. *et al.* Influence of electrode connection tracks on biological cell measurements by impedance spectroscopy, *Sensors*, v.19, n.13, p.2839, 2019. DOI:10.3390/S19132839.

139 LEI, K.F.; LEUNG, P.H.M. Microelectrode array biosensor for the detection of Legionella pneumophila, *Microelectronic Engineering*, v.91, p.174–7, 2012.

DOI:10.1016/J.MEE.2011.10.002.

140 STICKER, D. *et al.* Zirconium dioxide nanolayer passivated impedimetric sensors for cell-based assays, *Sensors and Actuators B*, v.213, p.35–44, 2015. DOI:10.1016/J.SNB.2015.02.018.

141 RIUL JUNIOR, A. *et al.* Recent advances in electronic tongues, *The Analyst*, v.135, n.10, p.2481, 2010. DOI:10.1039/C0AN00292E.

142 ZHANG, B.H. *et al.* LabVIEW-based impedance biosensing system for detection of avian influenza virus, *International Journal of Agricultural and Biological Engineering*, v.9, n.4, p.116–22, 2016. DOI:10.3965/J.IJABE.20160904.1704.

143 DAS, N. *et al.* Nanostructured silicon oxide immunosensor integrated with noise spectroscopy electronics for POC diagnostics. *In*: INTERNATIONAL CONFERENCE ON VLSI DESIGN, 2016. *Proceedings*[…], Kolkata:2016, p.367–72. DOI:10.1109/VLSID.2016.53.

144 SOARES, A.C. *et al.* Microfluidic-based genosensor to detect Human Papillomavirus (HPV16) for head and neck cancer, *ACS Applied Materials & Interfaces*, v.10, n.43, p.36757–63, 2018. DOI:10.1021/ACSAMI.8B14632.

145 SOARES, J.C. *et al.* Detection of a SARS-CoV-2 sequence with genosensors using data analysis based on information visualization and machine learning techniques, *Materials Chemistry Frontiers*, v.5, n.15, p.5658–70, 2021. DOI:10.1039/D1QM00665G.

146 WU, H. *et al.* A polyaniline-modified immunosensor based on four-wire interdigitated microelectrode, *Journal of Micro-Bio Robotics*, v.12, n.1–4, p.1–8, 2017. DOI:10.1007/S12213-016-0093-Z.

147 QUEIRÓS, R.B. *et al.* A label-free DNA aptamer-based impedance biosensor for the detection of E. coli outer membrane proteins, *Sensors and Actuators B*, v.181, p.766–72, 2013. DOI:10.1016/J.SNB.2013.01.062.

148 JIANG, K. *et al.* Rapid label-free detection of E. coli using antimicrobial peptide assisted impedance spectroscopy, *Analytical Methods*, v.7, n.23, p.9744–8, 2015. DOI:10.1039/C5AY01917F.

149 ESTRADA-LEYPON, O. *et al.* Simultaneous monitoring of Staphylococcus aureus growth in a multi-parametric microfluidic platform using microscopy and impedance spectroscopy, *Bioelectrochemistry*, v.105, p.56–64, 2015. DOI:10.1016/J.BIOELECHEM.2015.05.006.

150 WILSON, D. *et al.* Electrical detection of pathogenic bacteria in food samples using information visualization methods with a sensor based on magnetic nanoparticles functionalized with antimicrobial peptides, *Talanta*, v.194, p.611–8, 2019. DOI:10.1016/J.TALANTA.2018.10.089.

151 PAREDES, J. *et al.* Interdigitated microelectrode biosensor for bacterial biofilm growth monitoring by impedance spectroscopy technique in 96-well microtiter plates, *Sensors and Actuators B*, v.178, p.663–70, 2013. DOI:10.1016/J.SNB.2013.01.027.

152 PAL, N. *et al.* Sensitive and rapid detection of pathogenic bacteria in small volumes using impedance spectroscopy technique, *Biosensors and Bioelectronics*, v.77, p.270–6, 2016.

DOI:10.1016/J.BIOS.2015.09.037.

153 TUBÍA, I. *et al.* Antibody biosensors for spoilage yeast detection based on impedance spectroscopy, *Biosensors and Bioelectronics*, v.102, p.432–8, 2018. DOI:10.1016/J.BIOS.2017.11.057.

154 ROCHA NETO, J.B.M. *et al.* Polysaccharide multilayer films in sensors for detecting prostate tumor cells based on hyaluronan-CD44 interactions, *Cells*, v.9, n.6, p.1563, 2020. DOI:10.3390/CELLS9061563.

155 SOARES, A.C. *et al.* A simple architecture with self-assembled monolayers to build immunosensors for detecting the pancreatic cancer biomarker CA19-9, *The Analyst*, v.143, n.14, p.3302–8, 2018. DOI:10.1039/C8AN00430G.

156 SOARES, J.C. *et al.* Immunosensor for pancreatic cancer based on electrospun nanofibers coated with carbon nanotubes or gold nanoparticles, *ACS Omega*, v.2, n.10, p.6975–83, 2017. DOI:10.1021/ACSOMEGA.7B01029.

157 SORAYA, G. *et al.* A label-free, quantitative fecal hemoglobin detection platform for colorectal cancer screening, *Biosensors*, v.7, n.4, p.19, 2017. DOI:10.3390/BIOS7020019.

158 YUN, J. *et al.* Ex vivo identification of thyroid cancer tissue using electrical impedance spectroscopy on a needle, *Sensors and Actuators B*, v.261, p.537–44, 2018. DOI:10.1016/J.SNB.2018.01.155.

159 KUSHNER, R.F. Bioelectrical impedance analysis: A review of principles and applications, *Journal of the American College of Nutrition*, v.11, n.2, p.199–209, 1992. DOI:10.1080/07315724.1992.12098245.

160 MORAES, M.L. *et al.* Immobilization of cholesterol oxidase in LbL films and detection of cholesterol using ac measurements, *Materials Science and Engineering C*, v.29, n.2, p.442–7, 2009. DOI:10.1016/J.MSEC.2008.08.040.

161 MORAES, M.L. *et al.* Detection of glucose and triglycerides using information visualization methods to process impedance spectroscopy data, *Sensors and Actuators B*, v.166–167, p.231–8, 2012. DOI:10.1016/J.SNB.2012.02.046.

162 GARCIA-HERNANDEZ, C. *et al.* Impedimetric electronic tongue based on nanocomposites for the analysis of red wines. Improving the variable selection method, *Sensors and Actuators B*, v.277, p.365–72, 2018. DOI:10.1016/J.SNB.2018.09.023.

163 ELAMINE, Y. *et al.* Insight into the sensing mechanism of an impedance based electronic tongue for honey botanic origin discrimination, *Sensors and Actuators B*, v.285, p.24–33, 2019. DOI:10.1016/J.SNB.2019.01.023.

164 RIUL JUNIOR, A. *et al.* An artificial taste sensor based on conducting polymers, *Biosensors and Bioelectronics*, v.18, n.11, p.1365–9, 2003. DOI:10.1016/S0956-5663(03)00069-1.

165 IBBA, P. *et al.* Low-cost bio-impedance analysis system for the evaluation of fruit ripeness, *Proceedings of IEEE Sensors*, p.1–4, 2018. DOI:10.1109/ICSENS.2018.8589541.

166 FACURE, M.H.M. *et al.* Detection of trace levels of organophosphate pesticides using an electronic tongue based on graphene hybrid nanocomposites, *Talanta*, v.167, p.59–66, 2017.

DOI:10.1016/J.TALANTA.2017.02.005.

167 CHEN, Y. *et al.* CMOS high density electrical impedance biosensor array for tumor cell detection, *Sensors and Actuators B*, v.173, p.903–7, 2012. DOI:10.1016/J.SNB.2012.07.024.

168 KASIVISWANATHAN, U. *et al.* Fabrication of MSM-based biosensing device for assessing dynamic behavior of adherent mammalian cells, *IEEE Sensors Journal*, v.20, n.17, p.9652–9, 2020. DOI:10.1109/JSEN.2020.2990919.

169 KASIVISWANATHAN, U. *et al.* Functional behavior of the primary cortical neuronal cells on the large surface of TiO_2 and SnO_2 based biosensing device, *IEEE Transactions on NanoBioscience*, v.20, n.2, p.138–45, 2021. DOI:10.1109/TNB.2021.3058332.

170 KASIVISWANATHAN, U. *et al.* Extended large area Si/ZnO heterojunction biosensor for assessing functional behavior of primary cortical neuronal cells, *IEEE Sensors Journal*, v.21, n.13, p.14619–26, 2021. DOI:10.1109/JSEN.2021.3072448.

171 CUI, F. *et al.* Advancing biosensors with machine learning, *ACS Sensors*, v.5, n.11, p.3346–64, 2020. DOI:10.1021/ACSSENSORS.0C01424.

172 LEKHA, S.; M, S. Recent advancements and future prospects on e-nose sensors technology and machine learning approaches for non-invasive diabetes diagnosis: A review, *IEEE Reviews in Biomedical Engineering*, v.14, p.127–38, 2021. DOI:10.1109/RBME.2020.2993591.

173 ADAMS, M.J. *Chemometrics in analytical spectroscopy*, Cambridge, UK: The Royal Society of Chemistry, 1995.

174 SILVA, T.A. da *et al.* 3D-printed graphene electrodes applied in an impedimetric electronic tongue for soil analysis, *Chemosensors*, v.7, n.4, p.50, 2019. DOI:10.3390/CHEMOSENSORS7040050.

175 GUPTA, A.K. *et al.* Label-free electrochemical detection of dibenzofuran using MnO_2 nanofibres, *IEEE Sensors Journal*, v.20, n.21, p.12537–42, 2020. DOI:10.1109/JSEN.2020.3002158.

176 SAWHNEY, M.A.; CONLAN, R.S. POISED-5, a portable on-board electrochemical impedance spectroscopy biomarker analysis device, *Biomedical Microdevices*, v.21, n.3, 2019. DOI:10.1007/S10544-019-0406-9.

177 OLIVEIRA, O.N. *et al.* Information visualization to enhance sensitivity and selectivity in biosensing, *Biointerphases*, v.7, n.1, p.53, 2012. DOI:10.1007/S13758-012-0053-7.

178 MAGRO, C. *et al.* Polyelectrolyte based sensors as key to achieve quantitative electronic tongues: Detection of triclosan on aqueous environmental matrices, *Nanomaterials*, v.10, n.4, p.640, 2020. DOI:10.3390/NANO10040640.

179 MEYROWITZ, A.L.; CHIPMAN, S. *Foundations of knowledge acquisition:* machine learning, Norwell, USA: Kluwer Academic Publishers, 1993.

180 CUNHA, A.B. *et al.* Machine learning for stem cell differentiation and proliferation classification on electrical impedance spectroscopy, *Journal of Electrical Bioimpedance*, v.10, n.1, p.124–32, 2019. DOI:10.2478/JOEB-2019-0018.

181 BANERJEE, A. *et al.* Nanostructures for biosensing, with a brief overview on cancer detection, IoT, and the role of machine learning in smart biosensors, *Sensors*, v.21, n.4, p.1253, 2021. DOI:10.3390/S21041253.

182 FERREIRA, E.J. *et al.* Random subspace method for analysing coffee with electronic tongue, *Electronics Letters*, v.43, n.21, p.1138, 2007. DOI:10.1049/EL:20071182.

183 CHRISTINELLI, W.A. *et al.* Two-dimensional MoS2-based impedimetric electronic tongue for the discrimination of endocrine disrupting chemicals using machine learning, *Sensors and Actuators B*, v.336, p.129696, 2021. DOI:10.1016/J.SNB.2021.129696.

184 TIITTA, M. *et al.* Classification of wood chips using electrical impedance spectroscopy and machine learning, *Sensors*, v.20, n.4, p.1076, 2020. DOI:10.3390/S20041076.

185 POPOLIN NETO, M. *et al.* Machine learning used to create a multidimensional calibration space for sensing and biosensing data, *Bulletin of the Chemical Society of Japan*, v.94, n.5, p.1553–62, 2021. DOI:10.1246/BCSJ.20200359.

186 BUSCAGLIA, L.A. *et al. Sistema e dispositivo de medição de espectro de impedância elétrica portáteis*. Depositante: Universidade de São Paulo, BR n.1020210209402. Depósito: 19 Out. 2021. Em andamento.

187 SOARES, J.C. *et al.* Adsorption according to the Langmuir–Freundlich model is the detection mechanism of the antigen p53 for early diagnosis of cancer, *Physical Chemistry Chemical Physics*, v.18, n.12, p.8412–8, 2016. DOI:10.1039/C5CP07121F.

188 D'AURELIO, R. *et al.* Molecularly imprinted nanoparticles based sensor for cocaine detection, *Biosensors*, v.10, n.3, p.1–13, 2020. DOI:10.3390/BIOS10030022.

189 ANALOG DEVICES *Circuit note CN-0217: High accuracy impedance measurements using 12-bit impedance converters*, Norwood, USA, 2011, Available from: http://www.analog.com/media/en/reference-design-documentation/reference-designs/CN0217.pdf. Access at: 12.01.2022.

190 DAI, T.; ADLER, A. In vivo blood characterization from bioimpedance spectroscopy of blood pooling, *IEEE Transactions on Instrumentation and Measurement*, v.58, n.11, p.3831–8, 2009. DOI:10.1109/TIM.2009.2020836.

191 GÓMEZ, F. *et al.* Modeling and simulation of equivalent circuits in description of biological systems - A fractional calculus approach, *Journal of Electrical Bioimpedance*, v.3, n.1, p.2–11, 2012. DOI:10.5617/JEB.225.

192 QIAO, G. *et al.* Bioimpedance analysis for the characterization of breast cancer cells in suspension, *IEEE Transactions on Biomedical Engineering*, v.59, n.8, p.2321–9, 2012. DOI:10.1109/TBME.2012.2202904.

193 FREEBORN, T.J.; BOHANNAN, G.W. Changes of fractional-order model parameters in biceps tissue from fatiguing exercise, *IEEE International Symposium on Circuits and Systems*, p.1–5, 2018. DOI:10.1109/ISCAS.2018.8351812.

194 ZENG, R. *et al.* CRISPR-Cas12a-driven MXene-PEDOT:PSS piezoresistive wireless biosensor, *Nano Energy*, v.82, p.105711, 2021. DOI:10.1016/J.NANOEN.2020.105711.

195 CHEN, J. *et al.* Ti3C2 MXene nanosheet-based capacitance immunoassay with tyramine-

enzyme repeats to detect prostate-specific antigen on interdigitated micro-comb electrode, *Electrochimica Acta*, v.319, p.375–81, 2019. DOI:10.1016/J.ELECTACTA.2019.07.010.

196 YU, Z. *et al.* Pressure-based biosensor integrated with a flexible pressure sensor and an electrochromic device for visual detection, *Analytical Chemistry*, v.93, n.5, p.2916–25, 2021. DOI:10.1021/ACS.ANALCHEM.0C04501.

197 CARVALHO, L.R. de *et al.* Cyanobacterial occurrence and detection of microcystin by planar chromatography in surface water of Billings and Guarapiranga Reservoirs, SP, Brazil, *Revista Brasileira de Botânica*, v.30, n.1, p.141–8, 2007. DOI:10.1590/S0100-84042007000100014.

198 BITTENCOURT-OLIVEIRA, M. *et al.* Toxic cyanobacteria in reservoirs in northeastern Brazil: detection using a molecular method, *Brazilian Journal of Biology*, v.70, n.4, p.1005–10, 2010. DOI:10.1590/S1519-69842010000500012.

199 BORTOLI, S. *et al.* Growth and microcystin production of a Brazilian Microcystis aeruginosa strain (LTPNA 02) under different nutrient conditions, *Revista Brasileira de Farmacognosia*, v.24, n.4, p.389–98, 2014. DOI:10.1016/J.BJP.2014.07.019.

200 POURIA, S. *et al.* Fatal microcystin intoxication in haemodialysis unit in Caruaru, Brazil, *The Lancet*, v.352, n.9121, p.21–6, 1998. DOI:10.1016/S0140-6736(97)12285-1.

201 BRASIL. Ministerio da Saude. Portaria de Consolidaçao n.5, de 28 de setembro de 2017**.** *Consolidaçao das normas sobre as açoes e os serviços de saude do Sistema Unico de Saude*. Disponivel em: http://portalsinan.saude.gov.br/images/documentos/Legislacoes/Portaria_Consolidacao_5_28_SETEMBRO_2017.pdf. Acesso em: 12.01.22.

202 CONSELHO NACIONAL DE MEIO AMBIENTE.CONAMA. *Resolução n. 357*: Dispõe sobre a classificação dos corpos de água e diretrizes ambientais para o seu enquadramento, bem como estabelece as condições e padrões de lançamento de efluentes, e dá outras providências. *Diario Oficial*, n.53,18.03.2005. p.1–36.

203 REYNOLDS, C.S. *et al.* On the annual cycle of the blue-green alga Microcystis Aeruginosa Kütz. Emend. Elenkin, *Philosophical Transactions of the Royal Society of London*, v.293, n.1068, p.419–77, 1981. DOI:10.1098/RSTB.1981.0081.

204 GORHAM, P.R. *et al.* Isolation and culture of toxic strains of Anabaena flos-aquae (Lyngb.) de Bréb, *SIL Proceedings, 1922-2010*, v.15, n.2, p.796–804, 1964. DOI:10.1080/03680770.1962.11895606.

205 JACINAVICIUS, F.R. *et al. Manual para cultivo de cianobactérias*. São Paulo: Secretaria do Meio Ambiente do Estado de São Paulo, 2012. v.1, p.1–32.

206 COMPANHIA AMBIENTAL DO ESTADO DE SÃO PAULO. *Norma técnica L5.303*: fitoplâncton de água doce: métodos qualitativos e quantitativos. Sao Paulo: CETESB.2012. p.24.

207 LUND, J.W.G. *et al.* The inverted microscope method of estimating algal numbers and the statistical basis of estimations by counting, *Hydrobiologia*, v.11, n.2, p.143–70, 1958. DOI:10.1007/BF00007865.

208 MATTIOLI, I.A. *et al.* On the challenges for the diagnosis of SARS-CoV-2 based on a

review of current methodologies, *ACS Sensors*, v.5, n.12, p.3655–77, 2020. DOI:10.1021/ACSSENSORS.0C01382.

209 SINGH, A. *et al.* COVID-19: From bench to bed side, *Diabetes & Metabolic Syndrome*, v.14, n.4, p.277–81, 2020. DOI:10.1016/J.DSX.2020.04.011.

210 OLIVEIRA, B.A. *et al.* SARS-CoV-2 and the COVID-19 disease: a mini review on diagnostic methods, *Revista Do Instituto de Medicina Tropical de São Paulo*, v.62, p.1–8, 2020. DOI:10.1590/S1678-9946202062044.

211 MAHARI, S. *et al.* Ecovsens-ultrasensitive novel in-house built printed circuit board based electrochemical device for rapid detection of nCovid-19 antigen, a spike protein domain 1 of SARS-CoV-2, *BioRxiv*, 2020. DOI:10.1101/2020.04.24.059204.

212 BUSTIN, S.A.; NOLAN, T. RT-qPCR Testing of SARS-CoV-2: A primer, *International Journal of Molecular Sciences*, v.21, n.8, p.3004, 2020. DOI:10.3390/IJMS21083004.

213 CORMAN, V.M. *et al.* Detection of 2019 novel coronavirus (2019-nCoV) by real-time RT-PCR, *Eurosurveillance*, v.25, n.3, 2020. DOI:10.2807/1560-7917.ES.2020.25.3.2000045.

214 CHU, D.K.W. *et al.* Molecular diagnosis of a novel coronavirus (2019-nCoV) causing an outbreak of pneumonia, *Clinical Chemistry*, v.66, n.4, p.549–55, 2020. DOI:10.1093/CLINCHEM/HVAA029.

215 HOLSHUE, M.L. *et al.* First case of 2019 novel coronavirus in the United States, *New England Journal of Medicine*, v.382, n.10, p.929–36, 2020. DOI:10.1056/NEJMOA2001191.

216 HOSSEINI, A. *et al.* Roadmap to the bioanalytical testing of COVID-19: From sample collection to disease surveillance, *ACS Sensors*, v.5, n.11, p.3328–45, 2020. DOI:10.1021/ACSSENSORS.0C01377.

217 NGUYEN, T. *et al.* 2019 novel coronavirus disease (COVID-19): Paving the road for rapid detection and point-of-care diagnostics, *Micromachines*, v.11, n.3, p.306, 2020. DOI:10.3390/MI11030306.

218 BROUGHTON, J.P. *et al.* CRISPR–Cas12-based detection of SARS-CoV-2, *Nature Biotechnology*, v.38, n.7, p.870–4, 2020. DOI:10.1038/S41587-020-0513-4.

219 LOTFI, M.; REZAEI, N. CRISPR/Cas13: A potential therapeutic option of COVID-19, *Biomedicine & Pharmacotherapy*, v.131, p.110738, 2020. DOI:10.1016/J.BIOPHA.2020.110738.

220 BUNDSCHUH, C. *et al.* Evaluation of the EDI enzyme linked immunosorbent assays for the detection of SARS-CoV-2 IgM and IgG antibodies in human plasma, *Clinica Chimica Acta*, v.509, p.79–82, 2020. DOI:10.1016/J.CCA.2020.05.047.

221 ALHARBI, S.A. *et al.* Enzyme-linked immunosorbent assay for the detection of severe acute respiratory syndrome coronavirus 2 (SARS-CoV-2) IgM/IgA and IgG antibodies among healthcare workers, *Cureus*, v.2, n.9, 2020. DOI:10.7759/CUREUS.10285.

222 ZUO, B. *et al.* Piezoelectric immunosensor for SARS-associated coronavirus in sputum, *Analytical Chemistry*, v.76, n.13, p.3536–40, 2004. DOI:10.1021/AC035367B.

223 FABIANI, L. *et al.* Magnetic beads combined with carbon black-based screen-printed

electrodes for COVID-19: A reliable and miniaturized electrochemical immunosensor for SARS-CoV-2 detection in saliva, *Biosensors and Bioelectronics*, v.171, p.112686, 2021. DOI:10.1016/J.BIOS.2020.112686.

224 OROOJI, Y. *et al.* An overview on SARS-CoV-2 (COVID-19) and other human coronaviruses and their detection capability via amplification assay, chemical sensing, biosensing, immunosensing, and clinical assays, *Nano-Micro Letters*, v.13, n.1, p.18, 2021. DOI:10.1007/S40820-020-00533-Y.

225 YAKOH, A. *et al.* Paper-based electrochemical biosensor for diagnosing COVID-19: Detection of SARS-CoV-2 antibodies and antigen, *Biosensors and Bioelectronics*, v.176, p.112912, 2021. DOI:10.1016/J.BIOS.2020.112912.

226 RAZIQ, A. *et al.* Development of a portable MIP-based electrochemical sensor for detection of SARS-CoV-2 antigen, *Biosensors and Bioelectronics*, v.178, p.113029, 2021. DOI:10.1016/J.BIOS.2021.113029.

227 TER-OVANESYAN, D. *et al.* Ultrasensitive measurement of both SARS-CoV-2 RNA and antibodies from saliva, *Analytical Chemistry*, v.93, n.13, p.5365–70, 2021. DOI:10.1021/ACS.ANALCHEM.1C00515.

228 XU, L. *et al.* Facile biosensors for rapid detection of COVID-19, *Biosensors and Bioelectronics*, v.170, p.112673, 2020. DOI:10.1016/J.BIOS.2020.112673.

229 ABAD-VALLE, P. *et al.* DNA single-base mismatch study with an electrochemical enzymatic genosensor, *Biosensors and Bioelectronics*, v.22, n.8, p.1642–50, 2007. DOI:10.1016/J.BIOS.2006.07.015.

230 HAMIDI-ASL, E. *et al.* A genosensor for point mutation detection of P53 gene PCR product using magnetic particles, *Electroanalysis*, v.27, n.6, p.1378–86, 2015. DOI:10.1002/ELAN.201400660.

231 QIU, G. *et al.* Dual-functional plasmonic photothermal biosensors for highly accurate severe acute respiratory syndrome coronavirus 2 detection, *ACS Nano*, v.14, n.5, p.5268–77, 2020. DOI:10.1021/ACSNANO.0C02439.

232 HUANG, L. *et al.* One-step rapid quantification of SARS-CoV-2 virus particles via low-cost nanoplasmonic sensors in generic microplate reader and point-of-care device, *Biosensors and Bioelectronics*, v.171, p.112685, 2021. DOI:10.1016/J.BIOS.2020.112685.

233 DJAILEB, A. *et al.* A rapid and quantitative serum test for SARS-CoV-2 antibodies with portable surface plasmon resonance sensing, *ChemRxiv*, p.1–12, 2020. DOI:10.26434/CHEMRXIV.12118914.

234 SEO, G. *et al.* Rapid detection of COVID-19 causative virus (SARS-CoV-2) in human nasopharyngeal swab specimens using field-effect transistor-based biosensor, *ACS Nano*, v.14, n.4, p.5135–42, 2020. DOI:10.1021/ACSNANO.0C02823.

235 YILMAZ, L.S. *et al.* Systematic evaluation of single mismatch stability predictors for fluorescence in situ hybridization, *Environmental Microbiology*, v.10, n.10, p.2872–85, 2008. DOI:10.1111/J.1462-2920.2008.01719.X.

236 YILMAZ, L.S. *et al.* mathFISH, a web tool that uses thermodynamics-based mathematical models for in silico evaluation of oligonucleotide probes for fluorescence in situ

hybridization, *Applied and Environmental Microbiology*, v.77, n.3, p.1118–22, 2011. DOI:10.1128/AEM.01733-10.

237 MINGHIM, R. *et al.* Content-based text mapping using multi-dimensional projections for exploration of document collections, *Visualization and Data Analysis*, p.1–12, 2006. DOI:10.1117/12.650880.

238 LVOVICH, V.F. *Impedance spectroscopy:* applications to electrochemical and dielectric phenomena, Hoboken, USA: John Wiley & Sons, 2012.

239 BARSOUKOV, E.; MACDONALD, J.R. *Impedance spectroscopy:* theory, experiment, and applications, Hoboken, USA: John Wiley & Sons, 2005.

240 XU, M. *et al.* Hemin/G-quadruplex-based DNAzyme concatamers for in situ amplified impedimetric sensing of copper(II) ion coupling with DNAzyme-catalyzed precipitation strategy, *Biosensors and Bioelectronics,* v.74, p.1–7, 2015. DOI:10.1016/J.BIOS.2015.05.056.

241 QIU, Z. *et al.* Enzyme-triggered formation of enzyme-tyramine concatamers on nanogold-functionalized dendrimer for impedimetric detection of Hg(II) with sensitivity enhancement, *Biosensors and Bioelectronics*, v.75, p.108–15, 2016. DOI:10.1016/J.BIOS.2015.08.026.

242 TAYLOR, D.M.; MACDONALD, A.G. AC admittance of the metal/insulator/electrolyte interface, *Journal of Physics D*, v.20, n.10, p.1277–83, 1987. DOI:10.1088/0022-3727/20/10/010.

243 INSELBERG, A.; DIMSDALE, B. Parallel coordinates: a tool for visualizing multi-dimensional geometry, *In:* IEEE CONFERENCE ON VISUALIZATION, 1990. *Proceedings*[…], Washington,DC:1990, p.361–78. DOI:10.1109/VISUAL.1990.146402.

244 CURRIE, L.A. Nomenclature in evaluation of analytical methods including detection and quantification capabilities (IUPAC Recommendations 1995), *Analytica Chimica Acta*, v.391, n.2, p.105–26, 1999. DOI:10.1016/S0003-2670(99)00104-X.

245 LABORATORY CORPORATION OF AMERICA. *Emergency use authorization (EUA) summary covid-19 RT-PCR test*, p.1-30, 2021. Available from: https://www.fda.gov/media/136151/download#:~:text=The%20COVID%2D19%20RT%2DPCR%20Test%20is%20a%20real%2D,tract%20aspirates%2C%20bronchoalveolar%20lavage%2C%20and. Access at: 08.04.2022.

246 CARR, O. *et al.* Genosensor made with a self-assembled monolayer matrix to detect MGMT gene methylation in head and neck cancer cell lines, *Talanta*, v.210, p.120609, 2020. DOI:10.1016/J.TALANTA.2019.120609.